Plasticity of Human Microglia and Brain Perivascular Macrophages in Aging and Alzheimer's Disease

Authors

Donghoon Lee[#†1,2,3,4], James M. Vicari[#1,2,3,4], Christian Porras[#1,2,3,4], Collin Spencer[#1,2,3,4], Milos Pjanic[1,2,3,4], Xinyi Wang[1,2,3,4], Seon Kinrot[1,2,3,4], Philipp Weiler[5,6], Roman Kosoy[1,2,3,4], Jaroslav Bendl[1,2,3,4], Prashant N M[1,2,3,4], Konstantina Psychogyiou[1,2,3,4], Periklis Malakates[1,2,3,4], Evelyn Hennigan[1,2,3,4], Jennifer Monteiro Fortes[1,2,3,4], Shiwei Zheng[3,7,8], Karen Therrien[1,2,3,4], Deepika Mathur[1,2,3,4], Steven P. Kleopoulos[1,2,3,4], Zhiping Shao[1,2,3,4], Stathis Argyriou[1,2,3,4], Marcela Alvia[1,2,3,4], Clara Casey[1,2,3,4], Aram Hong[1,2,3,4], Kristin G. Beaumont[3], Robert Sebra[3], Christopher P. Kellner[9], David A. Bennett[10], Guo-Cheng Yuan[3,7,8], George Voloudakis[1,2,3,4], Fabian J. Theis[5,6,11], Vahram Haroutunian[2,4,12,13], Gabriel E. Hoffman[1,2,3,4,13], John F. Fullard[#1,2,3,4], Panos Roussos[#†1,2,3,4,13]

Affiliations

[1] Center for Disease Neurogenomics, Icahn School of Medicine at Mount Sinai, New York, NY, USA.
[2] Department of Psychiatry, Icahn School of Medicine at Mount Sinai, New York, NY, USA.
[3] Department of Genetics and Genomic Sciences, Icahn School of Medicine at Mount Sinai, New York, NY, USA.
[4] Friedman Brain Institute, Icahn School of Medicine at Mount Sinai, New York, NY, USA.
[5] Institute of Computational Biology, Helmholtz Center Munich, Munich, Germany.
[6] Department of Mathematics, Technical University of Munich, Munich, Germany.
[7] Tisch Cancer Institute, Icahn School of Medicine at Mount Sinai, New York, NY 10029, USA.
[8] Black Family Stem Cell Institute, Icahn School of Medicine at Mount Sinai, New York, NY 10029, USA.
[9] Department of Neurosurgery, Icahn School of Medicine at Mount Sinai, New York, NY, USA.
[10] Rush Alzheimer's Disease Center, Rush University Medical Center, Chicago, IL, USA.
[11] TUM School of Life Sciences Weihenstephan, Technical University of Munich, Munich, Germany.
[12] Department of Neuroscience, Icahn School of Medicine at Mount Sinai, New York, NY, USA.
[13] Mental Illness Research, Education and Clinical Centers, James J. Peters VA Medical Center, Bronx, New York.

[#]These authors contributed equally to this work.
[†]Corresponding author: donghoon.lee@mssm.edu; panagiotis.roussos@mssm.edu

Abstract

The complex roles of myeloid cells, including microglia and perivascular macrophages, are central to the neurobiology of Alzheimer's disease (AD), yet they remain incompletely understood. Here, we profiled 832,505 human myeloid cells from the prefrontal cortex of 1,607 unique donors covering the human lifespan and varying degrees of AD neuropathology. We delineated 13 transcriptionally distinct myeloid subtypes organized into 6 subclasses and identified AD-associated adaptive changes in myeloid cells over aging and disease progression. The GPNMB subtype, linked to phagocytosis, increased significantly with AD burden and correlated with polygenic AD risk scores. By organizing AD-risk genes into a regulatory hierarchy, we identified and validated *MITF* as an upstream transcriptional activator of *GPNMB*, critical for maintaining phagocytosis. Through cell-to-cell interaction networks, we prioritized *APOE-SORL1* and *APOE-TREM2* ligand-receptor pairs, associated with AD progression. In both human and mouse models, *TREM2* deficiency disrupted GPNMB expansion and reduced phagocytic function, suggesting that GPNMB's role in neuroprotection was *TREM2*-dependent. Our findings clarify myeloid subtypes implicated in aging and AD, advancing the mechanistic understanding of their role in AD and aiding therapeutic discovery.

Main

Despite the quantifiable neuropathology of β-amyloid plaques (Aβ) and neurofibrillary tangles (NFTs) (*1*), the exact neurobiological mechanisms underlying Alzheimer's disease (AD) remain elusive. Brain myeloid-origin immune cells, including microglia and perivascular macrophages (PVMs), play crucial roles in the pathogenesis of AD (*2–9*), providing neuroprotective benefits by clearing lesions, but also exacerbating the disease through the induction of excessive neuroinflammation (*10*). While previous studies utilizing single-nucleus/-cell RNA sequencing (snRNA-seq/scRNA-seq) have made significant progress describing complex functional roles of murine and human microglia in AD (*5*, *11–14*), challenges with characterizing the wide spectrum of microglial heterogeneity and identifying more nuanced AD-associated subtypes still remain (*15*), largely due to limited sample sizes and differences in the single-cell technologies used. Among the issues that arise is the failure of nuclear fractions in snRNA-seq from frozen tissue to capture key genes related to microglial adaptation and response to pathogenic lesions (*16*). Moreover, microglia are highly reactive cells, and describing their adaptive nature using scRNA-seq in cells isolated from fresh tissue is challenging (*17*). To overcome those limitations, we present two independent human myeloid cohorts generated at single-cell resolution from the prefrontal cortex (PFC). In the first cohort, we isolated viable *ex-vivo* human myeloid cells from fresh postmortem PFC and deeply profiled both nuclear and cytoplasmic RNA. The second cohort focused on the breadth of the transcriptome, profiling human myeloid nuclei from a large number of demographically diverse frozen cortical tissues. By considering both the depth and the breadth of the human myeloid transcriptome, we establish a reproducible taxonomy and demonstrate the importance of

microglia and PVM plasticity throughout the lifespan, across different stages of AD pathological and clinical severity, and genetic liability.

Cellular taxonomy of human myeloid cells

In total, we profiled 832,505 human myeloid cells from the PFC of 1,607 unique donors. The first dataset, named FreshMG, includes samples from fresh autopsy tissue specimens of 137 unique postmortem donors recruited from two brain banks and contains individuals displaying varying degrees of AD neuropathology as well as controls (**Fig. 1A, Supplementary Fig. S1A**). FreshMG donors are aged between 26 and 107 years (average 80.7 years), comprising 76 females and 61 males. To enrich for myeloid cells, viable CD45+ cells were isolated via fluorescence-activated cell sorting (FACS). In addition, for a subset (n=3 donors, each with 8 technical replicates), we profiled surface-level protein markers using CITE-seq (*18*), using a panel of 154 unique antibodies, resulting in a total of 161 scRNA-seq libraries from fresh brain specimens. Following rigorous QC and initial clustering, we found a large, relatively homogeneous, cluster of myeloid cells along with small subsets of co-purified immune cells, such as monocytes, neutrophils, T, NK, and B cells. The myeloid cluster consisted of 543,012 microglia and PVMs robustly expressing 23,740 genes (**Supplementary Fig. S1E**).

The second dataset, named PsychAD, consists of frozen prefrontal cortex specimens and includes cases and controls from a cohort of 1,470 unique donors (**Fig. 1B**). PsychAD donors were aged between 0 and 108 years, (average 71.3 years), comprising 761 females and 709 males (**Supplementary Fig. S1B**). Frozen samples were subject to snRNA-seq profiling from which microglia and PVMs were sorted *in silico* after basic clustering. After rigorous QC, we identified 289,493 microglia and PVM nuclei robustly expressing 34,890 genes (**Supplementary Fig. S1F**). Next, we aligned and harmonized the scale of clinical variables to facilitate annotation of both datasets (**Methods**) and saw a strong positive correlation with measures of the severity of AD neuropathology, namely diagnostic certainty of AD, Consortium to Establish a Registry for Alzheimer's Disease (CERAD) (*19*), and Braak stage (*20*) (**Supplementary Fig. S1C**). In contrast, the clinical measures of dementia severity were less well correlated with AD.

Our primary objective was to establish a comprehensive cellular taxonomy that is robust and reproducible; however, cross-validating these independent and large-scale single-cell datasets, each with a distinct transcriptomic origin (whole cell vs. nuclei), posed technical challenges. To overcome these, we devised an iterative cross-validation strategy, which involved establishing a reference state and validating it independently until both datasets were in agreement (**Methods**). Utilizing the FreshMG dataset, which provides comprehensive transcriptomic profiles from both nuclear and cytosolic fractions, we identified functionally distinct phenotypes of microglia and PVMs. Subsequently, we cross-validated the presence of these reference subtypes in the frozen specimen snRNA-seq PsychAD dataset. Our iterative process converged on 13 functionally distinct subtypes of human myeloid cells (**Fig. 1C, Supplementary Fig. S2A, Supplementary Tables S1-2**), and comparison between FreshMG

and PsychAD revealed a high degree of consistency between the two cohorts, as evidenced by an average Pearson correlation of 0.77 across all identified subtypes (**Fig. 1F**). This rigorous methodology ensured the accuracy and reliability of our cellular taxonomy, laying a solid foundation for further analyses.

We grouped the cells using two levels of taxonomic hierarchy; the 13 distinct subtypes under six broad functional subclasses of human myeloid cells: Homeostatic (green), Adaptive (blue), Proliferative (yellow), AD-Associated or ADAM (red), *ex-vivo* Activated Microglia or exAM (pink), and PVM (orange) (**Fig. 1C**). Each subtype is associated with specific markers that not only aid in their identification but also hint at their functional significance (**Fig. 1D, Supplementary Fig. S2D**). Within the homeostatic microglia subclass, we highlight two subtypes, CECR2 and PICALM, both of which are associated with the regulation of GTPase activity. Homeostatic microglia make up the largest proportion of myeloid cells (**Supplementary Figs. S2B-C**) and express microglia-specific canonical markers such as *P2RY12* and *CX3CR1*. The CECR2 subtype uniquely expresses *CECR2* and *NAV2*, with other genes pointing towards cellular maintenance, phagocytosis, cell migration, and adhesion. The PICALM subtype shows elevated expression of *PICALM* and *ELMO1*, suggesting roles in the regulation of the immune response.

We identified 7 specialized microglial subtypes, each exhibiting unique adaptive responses to neuro-environmental cues. In general, the gene signatures across these adaptive microglia underscored an enhancement in antigen processing and presentation programs and the facilitation of MHC protein complex assembly. The CCL3 subtype is characterized by the upregulation of chemotactic genes, most notably the inflammatory cytokines *CCL3*, *CCL4*, and interleukin 1 beta (*IL1B*). In addition, the *IFI44L* subtype is enriched in interferon-inducible genes, like *IFIT1*, *IFIT2*, and *IFIT3*, suggesting a role in the antiviral innate immune response. The AIF1, HIF1A, and HIST clusters share a common gene program related to immunoglobulin-mediated immune response, while the TMEM163 cluster focuses on antigen processing and presentation via MHC II. The final adaptive cluster, HSPA1A, is enriched for gene signatures responsible for adaptive response to unfolded protein, which is characterized by elevated activity of heat shock proteins and cellular stress response, with a potential role in AD neuropathology (*21*). In addition, we identified a subtype, the GPNMB, which is predominantly observed in individuals with AD (*22*, *23*). These AD-associated microglia (ADAM) feature elevated expression of glycoprotein non-metastatic melanoma protein B (*GPNMB*), microphthalmia-associated transcription factor (*MITF*), and protein tyrosine phosphatase receptor type G (*PTPRG*) genes, and functional enrichment analysis suggests increased phagocytic activity is a hallmark of these cells. Consistent with previous studies (*11*), we also identified a cluster of proliferative cells, MKI67, that is highly enriched in cell-cycle dependent genes (*STMN1*, *MKI67*, *TOP2A*). Lastly, we report a cluster, ERN1, showing specific expression of *ERN1* and *PLK2* genes that resemble activation patterns of exAM (*17*) (**Supplementary Information**). In addition to microglial subtypes, we identified a PVM cluster, named CD163, expressing a unique set of known PVM-specific markers, notably *CD163* and *F13A1*. The CD163 cluster displayed a significant enrichment of genes involved in endocytic processes, emphasizing its priming for receptor-mediated endocytosis and phagocytosis. While we

observe a close similarity between ADAM and PVM clusters (**Supplementary Fig. S2A**), we found a clear separation between the two when we enriched for conserved murine disease-associated microglia (DAM) signatures as well as human DAM signature from iPSC-derived microglia (*5*, *23–25*) (**Supplementary Fig. S3A**).

We further annotated myeloid subtypes by estimating the enrichment with polygenic risk scores of heritable traits at single-cell resolution (`scDRS`; **Methods**; **Supplementary Fig. S3B, Supplementary Table S15**). We extended the analysis to a set of the brain related diseases beyond AD including schizophrenia (SCZ), bipolar disorder (BD), major depressive disorder (MDD), autism spectrum disorder (ASD), multiple sclerosis (MS), amyotrophic lateral sclerosis (ALS), and Parkinson's disease (PD). The polygenic risk scores for each trait were highly reproducible between the FreshMG and PsychAD cohorts with AD and MS having the greatest correlation (**Supplementary Fig. S3C**). The meta-analysis of both FreshMG and PsychAD cohorts indicated that the 9 subtypes of myeloid cells were significantly associated with heritable AD risk, which was the largest of all brain diseases followed by MS, SCZ, and MDD (**Fig. 1E**). Notably, the GPNMB subtype had the widest coverage showing significant heritable risks for all 8 diseases.

Multi-modal validation of human myeloid taxonomy

To show the utility of our annotation as the reference human myeloid taxonomy, we validated the reproducibility of 13 myeloid subtypes using several independent datasets. First, using a published human microglia dataset (*14*), we assessed the similarity of our taxonomy to existing microglia annotations. While we found 8 of their microglial states, including their brain-associated macrophage (BAM), resemble our subtypes (**Supplementary Fig. S3D**), the alignments were moderate for the remaining 5 states. After re-annotating their nuclei using our taxonomy as the reference (**Methods**), we confirmed the presence of all 13 subtypes (**Fig. 1G, Supplementary Fig. S3G**). We also discovered the subtype composition was comparable to our PsychAD snRNA-seq dataset (**Supplementary Figs. 2B-C**).

Since the taxonomy was established based on post-mortem tissues, we needed to ensure the taxonomy was not biased for post-mortem effects, and it can be reproduced using living brain tissues. Independent from the FreshMG and PsychAD cohorts, we generated an additional scRNA-seq dataset, called LivingMG, from brain biopsies, which were obtained from 25 unique human donors (26 libraries; 97,828 cells after QC) diagnosed with spontaneous intracerebral hemorrhage (ICH) (*26*). The brain tissue was collected during treatment and processed in an identical manner to the fresh autopsy material. It's important to note that cortical biopsy samples were obtained from a site distal to the site of the hemorrhage and, in the absence of a secondary diagnosis, are considered neurotypical controls. We annotated myeloid cells using the taxonomy derived from the FreshMG dataset and confirmed the presence of all 13 subtypes in living cells. (**Fig. 1G**, **Supplementary Fig. S3E, S3J**).

Since the taxonomy was primarily derived from sc/snRNA-seq datasets, we utilized different technology and modalities to confirm the robustness of our myeloid taxonomy. To validate the spatial context, we conducted deep single-cell phenotyping and spatial analysis using multiplexed imaging assay (Akoya PhenoCycler) and demonstrated, for example, PVMs

colocalize around blood vessels via staining for CD163 (**Fig. 1H**). Subsequently, we performed spatial transcriptomic characterization using the Xenium *in situ* technology on 11 tissue slides obtained from 8 individual donors (**Methods**). A custom panel of 366 genes, including both a pre-designed human brain panel and additional markers for myeloid subtypes, was used to further characterize the myeloid taxonomy (**Fig. 1I**). We showed the presence of 5 major subclasses excluding the exAM, which was not expected to be present in cryosectioned tissue (**Fig. 1G, Supplementary Figs. S3F, S4A-B**). While the resolution was limited in the Xenium data, we were able to stratify robust subtypes via stability analysis (**Methods**) and validated the presence of myeloid subtypes.

Lastly, we applied a multi-omic assay to further characterize the myeloid subtypes. We employed CITE-seq, jointly quantifying the transcriptome and 154 unique cell-surface proteins, to assess the preservation of the functional hierarchical structure at the protein-level. Using this approach, we confirmed the presence of distinct proteomic patterns for each myeloid subtype (**Supplementary Fig. S3K**). For example, within the homeostatic microglia subclass, the CECR2 subtype expressed *CD99* and *ITGB3*, while the PICALM subtype expressed *CLEC4C* and *TNFRSF13C* proteins as their markers. Likewise, the PVM cluster showed distinct surface markers, *CD163* and *CCR4*, while the ADAM cluster was specific for *CD9* and *CD44* proteins.

In summary, we used both external and independent datasets, as well as multi-omic modalities, to validate that the taxonomy is robust and consistent irrespective of the tissue source.

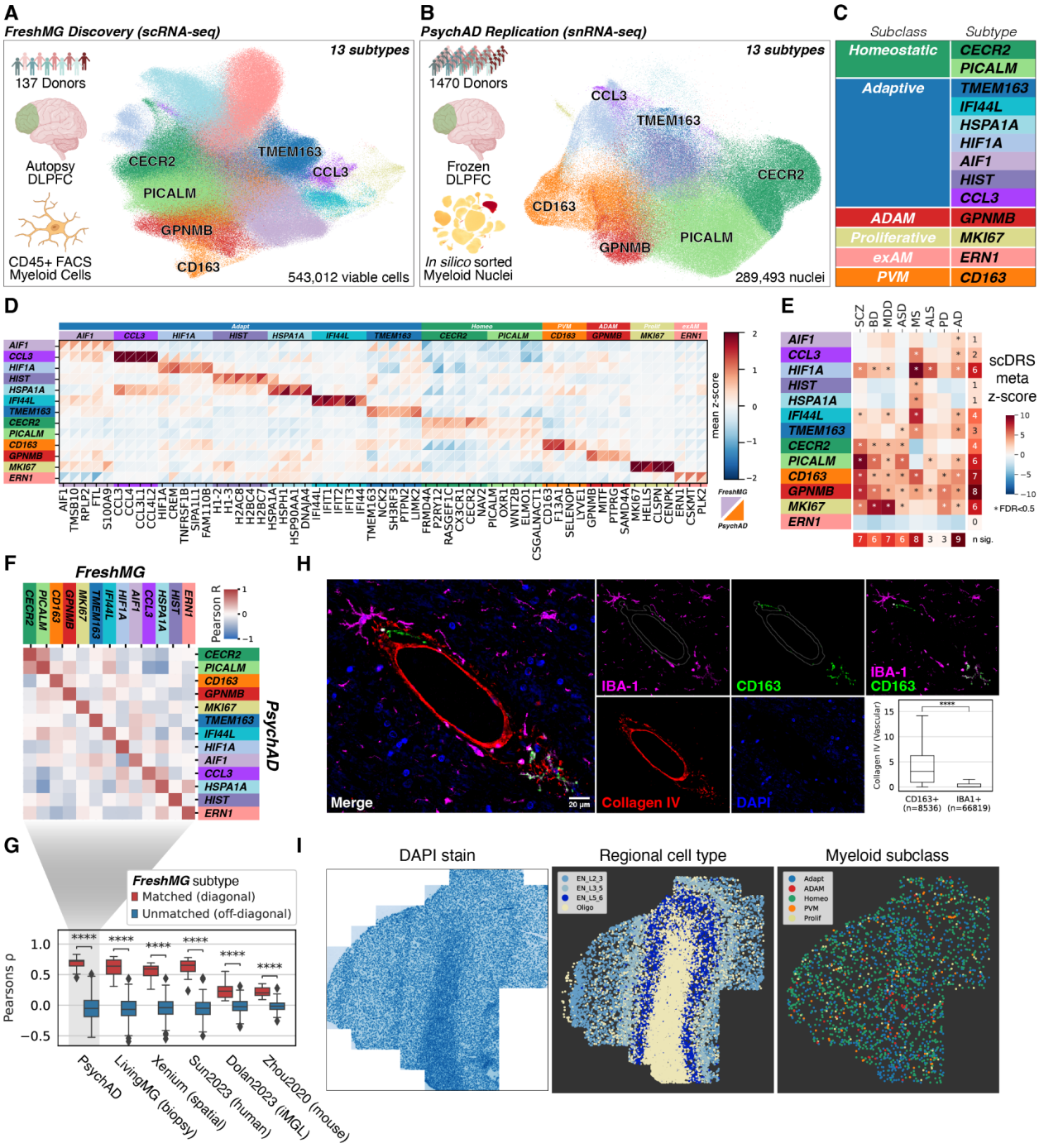

Figure 1. Overview of the human myeloid single-cell atlas. **(A)** the *FreshMG* discovery cohort (scRNA-seq) using live human myeloid cells from postmortem PFC and **(B)** the *PsychAD* replication cohort (snRNA-seq) using flash-frozen PFC tissues and *in-silico* sorted for microglia and PVMs. **(C)** Unified taxonomy of human myeloid subtypes. **(D)** Subtype-specific marker gene expression. Z-score normalized. Upper-triangle: *FreshMG*. Lower-triangle: *PsychAD*. **(E)** Enrichment of heritable disease risk (scDRS) by subtype using GWAS of 8 brain diseases. Meta-analysis between FreshMG and PsychAD. The asterisk denotes FDR < 0.05. SCZ: schizophrenia, BD: bipolar disorder, MDD: major depressive disorder, ASD: autism spectrum

disorder, MS: multiple sclerosis, ALS: amyotrophic lateral sclerosis, and PD: Parkinson's disease. **(F)** Pairwise Pearson correlation of the subtype-level taxonomy between *FreshMG* and *PsychAD* datasets using highly variable genes common in both datasets. **(G)** Validation of human myeloid taxonomy using independent, multi-modal, and published datasets. Human (*14*), iMGL: iPSC-derived microglia (*23*), and Mouse (*27*). Pairwise comparison of subtype-level taxonomy against the FreshMG annotation. Mann–Whitney U test between matched (diagonal) and unmatched (off-diagonal) subtypes. ****: $p \leq 1.0e-4$. **(H)** Representative image of Akoya PhenoCycler multiplex immunofluorescence results showing $CD163^{+}$/$IBA\text{-}1^{+}$ cells are enriched near blood vessels (outlined by gray line), labeled by Collagen IV. Scale bar 20 μm. **(I)** Representative slide of Xenium *in situ* spatial transcriptomics data. Left: DAPI, Middle: laminar distribution of neuronal cell types, Right: distribution of myeloid cells annotated by subclasses.

Variation in human myeloid subtype composition on aging and AD

After determining 13 distinct subtypes of human brain myeloid cells, we examined the compositional variation of myeloid subtypes that are associated with aging in a subset of neurotypical donors who were free of dementia and diagnostic neuropathology from the FreshMG and PsychAD datasets. We normalized the subtype count ratio data using the centered log-ratio transformation and modeled using a linear mixed model, accounting for technical and demographic variables (**Methods**). Notably, the two homeostatic microglia subtypes displayed opposing trajectories with respect to aging (**Figs 2A left, D**). The CECR2 subtype showed progressive decline while the PICALM subtype showed a gradual increase with age. In addition, we saw an overall increase in the proportions of the ADAM and PVM subtypes with age. These findings were replicated using published human microglia snRNA-seq dataset (*14*) (**Supplementary Fig. S4C**). In contrast, we observed an age-related decline in the CCL3 subtype, indicating a possible reduction of chemotactic microglia in older brains. In parallel, we investigated sex-dependent variation in human myeloid subtypes, with or without taking age into consideration, but did not find any statistically significant compositional differences between males and females (**Figs. 2A middle, right**).

Next, we examined the variation of subtype composition during onset and progression of AD. To minimize the effect of younger brains, we limited the analysis to donors 40 years and older, resulting in a dataset composed of 134 donors from the FreshMG and 1,314 donors from the PsychAD cohort. We first evaluated the involvement of myeloid subtypes using the centered log-ratio transformed count ratio data after accounting for technical and demographic variables (**Methods**). Overall, irrespective of different measures of AD phenotypes (dx_AD, CERAD, Braak, and Dementia), we observed robust changes in subtype proportions in both FreshMG and PsychAD cohorts (**Fig. 2B**). Similar to normal aging, two homeostatic subtypes showed opposing trends, where the CECR2 subtype showed a progressive decline with increasing AD burden while the PICALM subtype showed a gradual increase. While the trends were observed during the early stages of AD, a more substantial divergence occurred after Braak stage 3 (**Fig. 2E**). Likewise, we observed a consistent increase in the proportion of the PVM subtype. The most notable difference in the compositional variation of AD phenotypes compared to aging was the GPNMB subtype. The GPNMB subtype was an outlier and showed the largest effect size across all 4 AD phenotypes, suggesting that proliferation of the GPNMB subtype is a hallmark of AD (**Fig. 2C**). We further supported our findings by replicating the compositional variation analysis with previously published data (*14*). Consistent with our findings, we observed the GPNMB subtype was increasing in proportion while Homeo_CECR2 was decreasing with severe AD neuropathology (**Supplementary Figs. S4C-E**).

Causal mediation analysis of polygenic AD risk scoring and myeloid subtypes

Having established that certain myeloid subtypes are enriched for AD genetic risk (**Fig. 1E**) and that their compositional landscape shifts in the presence of AD (**Fig. 2B**), we next sought to evaluate the association of per-cell polygenic AD risk scores with the compositional variation

observed in AD (`scDRS`; **Methods**, **Supplementary Fig. S3B**). We observed a positive correlation (Pearson's r = 0.55) indicating that the ratio of subtypes with higher polygenic AD risk scores increases in AD (**Fig. 2F; Supplementary Fig. S4F**). This also suggested heritable risks might play a role in driving the compositional changes of myeloid subtypes.

Next, we leveraged our population-scale cohort to calculate per-donor AD polygenic risk scores (PRS; **Methods**) and to assess how the interindividual variation in AD risk impact changes in myeloid subtype composition (**Supplementary Fig. S3B**). The proportion of the GPNMB subtype was significantly increased with AD PRS (**Supplementary Fig. S4G**). We observed a similar compositional variation between AD phenotype (dx_AD) and PRS (**Fig. 2G circle**), which was not driven by the AD status alone as the same compositional variation was observed using a disease-free subset (**Fig. 2G triangle**).

To further dissect the relationships between genetic risk for AD and the observed changes in GPNMB subtype composition, we conducted a series of causal mediation analyses using the PRS as an instrumental variable (**Methods**). By examining the indirect effects of AD PRS on the GPNMB subtype composition, we aimed to clarify whether the observed cellular changes were driven by genetic predisposition or were a downstream consequence of AD pathology (plaque). Our analysis revealed a significant indirect effect of AD PRS on the GPNMB subtype, mediated through accumulation of Aβ plaques (Average Causal Mediated Effect (ACME) = 0.0254, 95%CI = [0.0137, 0.04], pval<2e-16). This indirect effect accounted for 60.5% of the total effect (pval = 0.034). These findings suggest that the GPNMB subtype variation is more likely a consequence of AD pathology. Furthermore, we observed a significant mediation effect of the GPNMB subtype variation on severity of dementia (8.29% of the total effect mediated, pval = 0.00096), suggesting that modification of this subtype via therapeutics could be a feasible treatment strategy for AD.

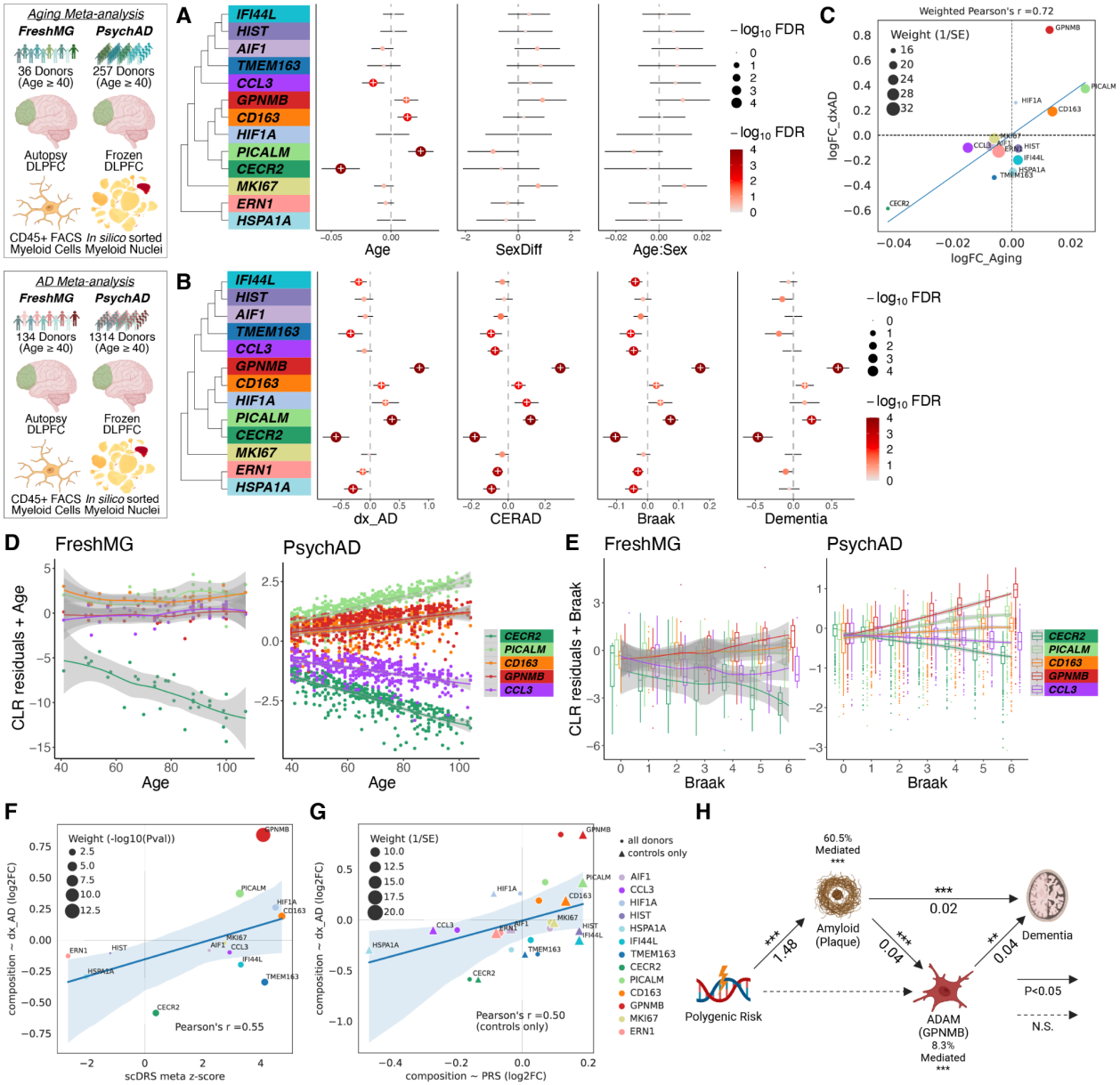

Figure 2. Variation in human myeloid subtype composition. **(A)** Compositional variation of myeloid subtypes by age, sex, and the interaction between age and sex using disease-free subset. CLR transformed composition data was modeled using a linear mixed model accounting for technical batch effects including tissue sources and sequencing pools and donor effects including age, sex, genetic ancestry, and PMI (see **Methods** on `crumblr`). Fixed effect meta-analysis using results from FreshMG and PsychAD cohorts. **(B)** Compositional variation of myeloid subtypes by four different neuropathological measures of the AD progression; diagnosis (dx_AD), CERAD, Braak staging, and dementia status, after accounting for technical and donor-level covariates. Fixed effect meta-analysis using both FreshMG and PsychAD cohorts. **(C)** Comparison of compositional variation between disease-free aging and AD. Subtypes were weighted by the inverse of standard error. **(D)** Covariate adjusted compositional variation with disease-free aging. CLR: centered-log-ratio. **(E)** Covariate

adjusted compositional variation with Braak staging. **(F)** Correlation between `scDRS` meta z-scores and `crumblr` estimate of compositional variation by dx_AD as a coefficient. Weighted Pearson's correlation using average -log10(P-value) as weights. **(G)** Correlation between `crumblr` estimate of compositional variation by PRS as a coefficient against `crumblr` estimate of compositional variation by dx_AD as a coefficient. Weighted Pearson's correlation using inverse of average of standard error as weights. Circle denotes `crumblr` analysis using all donors while triangle denotes `crumblr` analysis using controls only. **(H)** Causal mediation analysis using PRS, Aβ plaque, composition of the GPNMB subtype, and clinical dementia status. ***: $p \leq 1.0e-3$, **: $p \leq 1.0e-2$, NS: $p > 0.05$.

Variation in transcriptional regulation of human myeloid cells on aging and AD

We investigated the transcriptional regulation of human myeloid cells by examining the differential gene expression patterns associated with normal aging, and during the onset and progression of AD. In normal aging (**Supplementary Fig. S5A**), we discovered the increase in expression of the *MS4A6A* gene, a member of the MS4A family of cell membrane proteins, which are involved in the regulation of calcium signaling and have been implicated in neurodegenerative processes (*28*). The age-related gene expression changes for both homeostatic subtypes were enriched with actin filament-based process and actin cytoskeleton organization pathways, supporting their proposed roles in cell adhesion and migration (**Supplementary Fig. S5B**). The CD163 subtype was associated with the increase of cell adhesion processes as well as pathways related to cell proliferation. The gene signatures in the GPNMB subtype were enriched with immune response and activation. Overall, the increased involvement of PVM and ADAM subclasses indicated an upregulation of inflammatory responses in older individuals.

Next, we evaluated genes exhibiting differential expression patterns across four different measures of AD phenotypes (dx_AD, CERAD, Braak, and Dementia) (**Fig. 3A**). Our analysis led us to discover a set of AD-associated genes, including *PTPRG*, *DPYD*, and *IL15*, which displayed upregulation across all phenotypes capturing more severe AD stages. Pathway enrichment analysis revealed the PICALM and GPNMB subtypes share common pathways related to the regulation of cell adhesion (**Supplementary Fig. S5C**). In contrast, both the CECR2 and CD163 subtypes appear to be associated with negative regulation of cell projection organization.

Given the strong compositional shifts and gene signatures for AD phenotypes, we tested the presence of AD signatures in bulk microglia RNA-seq data (BulkMG; **Methods**). First, we created myeloid subtype signatures from both the FreshMG and PsychAD datasets by aggregating gene expression by subtype. We then compared the resulting subtype signatures to BulkMG gene expression data, stratified by AD case and control status. Interestingly, the Pearson correlation between subtypes and AD diagnosis clearly reflected the compositional shifts we observed across multiple AD phenotypes (**Supplementary Fig. S5D**). The CECR2, TMEM163, CCL3, and HSPA1A signatures closely correlated with the BulkMG from controls, while the PICALM, CD163, GPNMB, and HIF1A signatures closely matched those from AD cases. These results independently reproduce the observed changes in the myeloid transcriptome during the onset and progression of AD.

To model the dynamic changes that take place during the onset and progression of AD at a molecular level, we expanded our analysis from using discrete donor-level clinical variables to a continuous pseudotime measure by ordering cells along a disease trajectory. We estimated Braak-stage-informed ancestor-progenitor relations between observations through transport maps between neighboring disease stages using Moscot (*29*). We then quantified cell-cell transition probabilities, computed putative drivers, and constructed the disease-stage-informed pseudotime with CellRank 2 (*30*) (**Supplementary Fig. S5E**; **Methods;**

377 **Supplementary Information**). As expected, we observed an increase in pseudotime with
378 disease progression (**Supplementary Fig. S5F**). Stratified by subtypes, we observed that
379 PICALM homeostatic microglia were assigned larger pseudotime values (late), compared to
380 CECR2 homeostatic cells (early; p-value < 0.001, **Supplementary Fig. S5G**), indicating their
381 association with disease progression and aligning with the compositional variation of AD
382 phenotypes observed earlier. To identify potentially critical stages in disease progression, we
383 compared changes in pseudotime across disease stages for each myeloid subtype (**Methods**).
384 This analysis revealed that the change was most pronounced starting from Braak stage 3
385 (**Supplementary Fig. S5H**), which was also the critical time point the subtype composition
386 diverged in AD.
387

388 **Upstream regulators of AD genes in human myeloid cells**

389 After identifying potential AD risk genes, we analyzed myeloid gene regulatory networks
390 (GRNs) to discover key upstream transcriptional regulators. Using SCENIC (*31*, *32*), we
391 constructed GRNs based on expression data and known transcription factor (TF) binding
392 motifs and defined units of regulatory hierarchy (regulons) (**Fig. 3B, Supplementary Table**
393 **S12**). Subsequently, we assessed the enrichment of the regulon for each myeloid subtype
394 independently (**Supplementary Table S13**, **Methods**), revealing high concordance between
395 the FreshMG and PsychAD cohorts (**Fig. 3C**). We then derived combined regulon enrichment
396 scores using meta-analysis (**Methods**) and observed strong regulon subtype-specificity (**Fig.**
397 **3D**). The CECR2 and PICALM homeostatic subtypes were defined by enrichment of *KLF12*,
398 *GLIS3*, and *BACH2* regulons, while the PICALM, CD163, and GPNMB subtypes displayed
399 exclusive enrichment of *MITF* regulon. To link inferred regulons to differentially expressed AD
400 genes, we performed enrichment tests using 4 different types of AD risk signatures (**Methods**).
401 Notably, the target genes of *MITF*, *KLF12*, and *GLIS3* TFs were significantly associated with
402 AD risk profiles in the PICALM, CECR2, GPNMB, and HIF1A subtypes (**Fig. 3E**). *MITF* was
403 preferentially enriched with upregulated AD signatures, whereas *KLF12* and *GLIS3* were more
404 preferentially associated with downregulated AD signatures. Visualization of the joint *MITF-*
405 *KLF12-GLIS3* regulon network with AD risk genes revealed coordinated modulation of both up
406 and down-regulated candidate risk genes (**Fig. 3F**). These findings collectively suggest the
407 coordinated activity of *MITF*, *KLF12*, and *GLIS3* in regulating AD risk gene expression in
408 disease-associated microglia states. Functional enrichment analysis revealed that *MITF*,
409 *KLF12*, and *GLIS3* target genes were involved in key biological processes for microglia
410 function such as phagocytosis, cytokine production, and cellular response (**Supplementary**
411 **Fig. S6A**). Our findings that *MITF* distinctly regulates phagocytic-related pathways are in line
412 with previous findings from *in-vitro* models (*23*). In summary, by integrating differentially
413 expressed genes in AD with GRNs, we nominate *MITF*, *KLF12*, and *GLIS3* as potential
414 upstream master regulators of gene expression changes relevant to AD pathogenesis.
415

416 **Regulation of phagocytosis by MITF and GPNMB**

417 We prioritized *MITF* as a potential upstream regulator of AD-associated gene expression
418 critical for phagocytosis and the GPNMB subtype as the myeloid phenotype linked to AD. To

419 better understand the mechanistic relationship between them, we devised a lentiviral CRISPR
420 activation (CRISPRa) approach to activate genes in HMC3-VPR cell lines and measured the
421 level of phagocytosis under different substrate conditions (**Fig. 3G**). We first discovered that
422 the activation of *MITF* led to increased mRNA expression of *GPNMB* detected by qPCR but
423 not the other way around (**Supplementary Fig. S6D**), indicating that *MITF* is the upstream
424 regulator of *GPNMB* and validating our results using the GRN inference. Furthermore, we
425 observed that the activation of either *GPNMB* or *MITF* led to increased phagocytosis
426 regardless of substrate types **(Fig. 3H)**. Activating *MITF* was more effective at increasing
427 phagocytosis except under the myelin condition. When we added a drug (ML329) that inhibits
428 the *MITF* pathway, the phagocytosis was significantly reduced in all substrate conditions
429 (**Supplementary Fig. S6E**). Our results demonstrate the activation of phagocytosis requires a
430 cascade of regulatory events that involves *MITF* and *GPNMB* in AD.
431
432

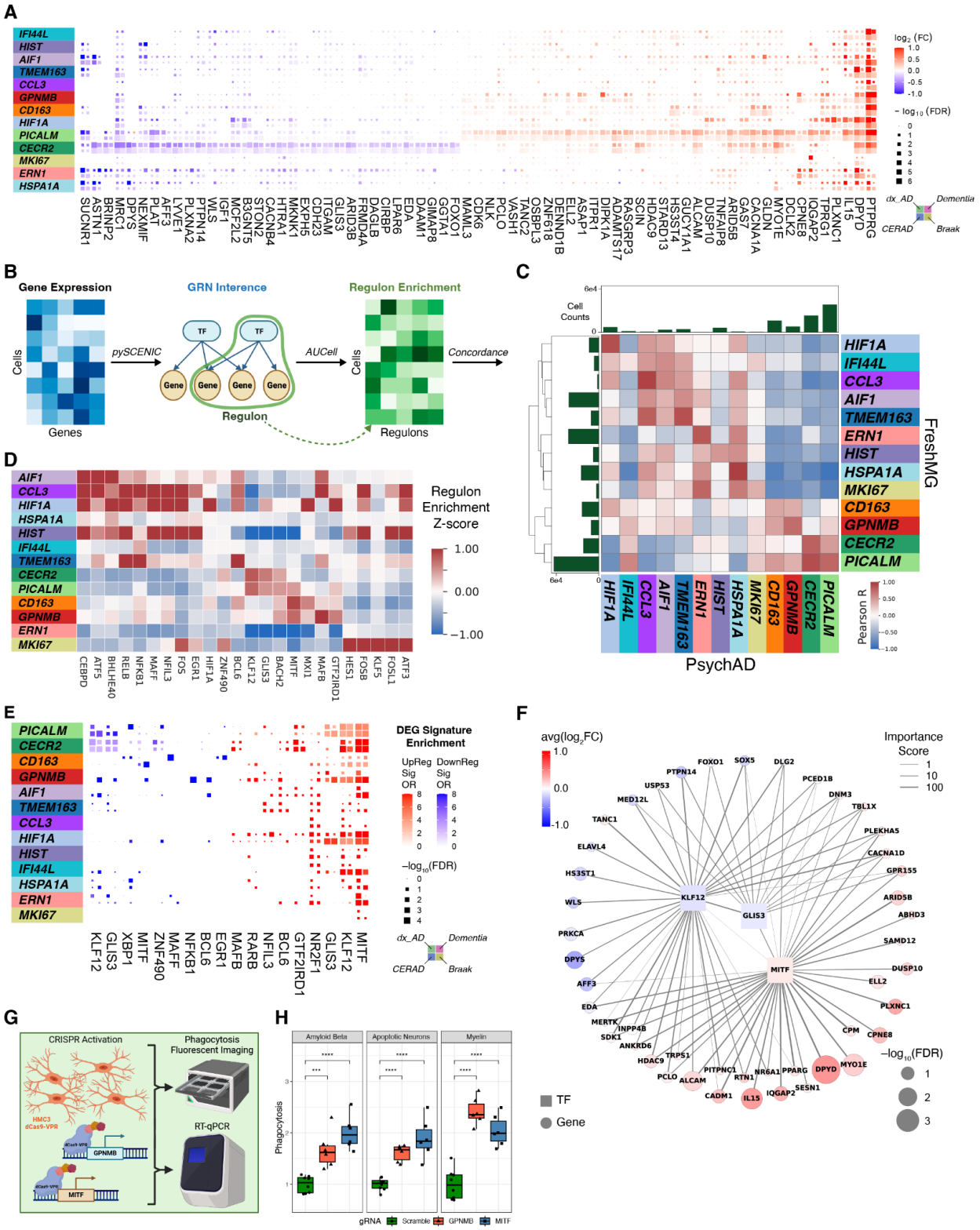

Figure 3. Transcriptional regulation of human myeloid cells. **(A)** Differentially expressed genes by four different measures of AD neuropathology adjusted for technical and donor-level covariates. Fixed effect meta-analysis using both FreshMG and PsychAD cohorts. **(B)** Schematic overview of GRN inference and TF-gene regulon enrichment for prioritization of

upstream master regulators of AD. **(C)** Concordance of normalized regulon activity scores (AUCell) between FreshMG and PsychAD cohorts. Pairwise Pearson correlation. **(D)** Enrichment of regulon by subtypes. Meta-analysis of consensus regulon enrichment Z-score with Stouffer's correction between FreshMG and PsychAD cohorts. Top 3 regulons per each subtype shown. **(E)** Enrichment of AD gene signatures by regulons. Fisher's exact tests for enrichment of differentially expressed gene signatures in regulon target genes across myeloid subtypes. **(F)** TFs that modulate AD risk genes. Gene regulatory network visualization of *KLF12*, *MITF*, and *GLIS3* TFs and downstream target risk genes. Node colors represent gene expression changes from `dreamlet` analysis. Edge weights represent importance scores inferred from the SCENIC pipeline. **(G)** Schematic of phagocytosis assay. **(H)** Relative level of phagocytosis after CRISPR activation in HMC3 cell line.

Non-cell-autonomous mechanisms affecting AD-associated microglia

To gain mechanistic insights into how different human myeloid subtypes communicate with each other and mediate AD risk through non-cell-autonomous mechanisms, we investigated the change of cell-to-cell interactions (CCIs) at different stages of AD using the `LIANA` framework (*33*) (**Supplementary Fig. S7A, Supplementary Table S14**). This approach allows us to dissect how myeloid cell signaling influences neighboring cells, potentially driving disease progression and highlighting targets for therapeutic intervention. For each individual, we inferred the magnitude, specificity, and directionality of cell-to-cell communication using gene expression profiles and known ligand-receptor interactions. We observed strong concordance between the magnitude of CCI activities from the FreshMG and the PsychAD cohorts (**Fig. 4A**), primarily for the homeostatic, PVM, and ADAM subtypes, whereas rare subtypes like MKI67 and CCL3 were less reproducible. By evaluating the CCI magnitude scores as a function of all 4 AD phenotypes using a linear mixed model, we identified differential CCIs associated with AD (**Fig. 4B, Supplementary Fig. S7B**), which were highly concordant across all 4 AD phenotypes (**Supplementary Fig. S7C**). We identified a total of 1,015 CCIs at FDR of 5% that were upregulated or downregulated in AD. The *APOE-SORL1* and *APOE-TREM2* interaction scores were higher in AD and were prioritized as the top AD-relevant CCIs, while *MRC1-PTPRC* interactions were down-regulated in AD. To test for genetic association, we performed the gene-set enrichment analyses on CCI pairs with increased scores in AD using GWAS data (*34*) (**Fig. 4C, Methods**). We observed AD-associated receptors had a strong association with AD risk but not with ligands. Visualizing the CCIs as directional networks in the context of different myeloid subtypes placed the GPNMB subtype as the most affected hub for CCIs that were upregulated in AD (**Fig. 4D**). Notably, the GPNMB subtype served as the receiving node for the *APOE-TREM2* interaction. To better understand the downstream effect of genes participating in AD-associated CCIs, we performed pathway enrichment analysis, uncovering that GPNMB-related CCIs were enriched with lipid metabolism and regulation of proteolysis (**Fig. 4E**).

TREM2-dependent regulation of phagocytosis by AD-associated microglia

Previous studies have shown that *TREM2*, a myeloid cell receptor, plays a crucial role in the activation of disease-associated microglia, with variants increasing AD risk (*5*, *27*, *35–40*). Given the higher expression of *APOE-TREM2* CCI in the GPNMB subtype, we hypothesized that GPNMB expansion in AD is partially *TREM2*-dependent. To investigate this hypothesis, we first examined the impact of highly penetrant *TREM2* variants for AD (R47H; rs75932628; n = 21 and R62H; rs143332484; n = 26) (*39*) on changes of the microglia subtype composition. We found that carriers of these *TREM2* mutations did not exhibit an expansion of the GPNMB subtype during progression of AD (**Fig. 4F**), supporting a potentially protective role of this subtype in phagocytosis and the amelioration of AD pathology. To further explore this, we utilized the published snRNA-seq dataset on Trem2-deficient 5XFAD mice (*27*) (**Fig.4G**). Similar to the human data, in the 5XFAD mouse model, we show an increase in the proportion of the GPNMB subtype, which was absent in the Trem2-deficient 5XFAD mice.

492 Finally, we utilized isogenic induced pluripotent stem cell (iPSC)-derived microglia that were
493 wild-type (WT), heterozygous (HZ), or homozygous (HO) for *TREM2*. *TREM2* knockout cells (HZ
494 and HO) showed approximately 50% lower *GPNMB* and *MITF* mRNA expression compared to
495 WT (**Supplementary Fig. S7D**). Phagocytosis assays using Aβ, myelin, and synaptic protein as
496 substrates revealed significant reduction in phagocytic activity for both HZ and HO lines
497 compared to WT (**Fig. 4I, Supplementary Fig. S7E**). Furthermore, inhibiting the *MITF* pathway
498 (with ML329) leads to a significant reduction in Aβ phagocytosis in WT cells. We used FACS to
499 separate microglia into high- and low-phagocytosing populations based on the fluorescence of
500 pHrodo-labeled substrates (**Fig. 4H, Supplementary Fig. S7F**). *GPNMB* protein levels were
501 higher in cells with high phagocytic activity (**Fig. 4J**). Similarly, RT-qPCR revealed that high-
502 phagocytosing cells exhibited higher levels of *GPNMB* mRNA than low-phagocytosing cells
503 across all substrate conditions.
504
505

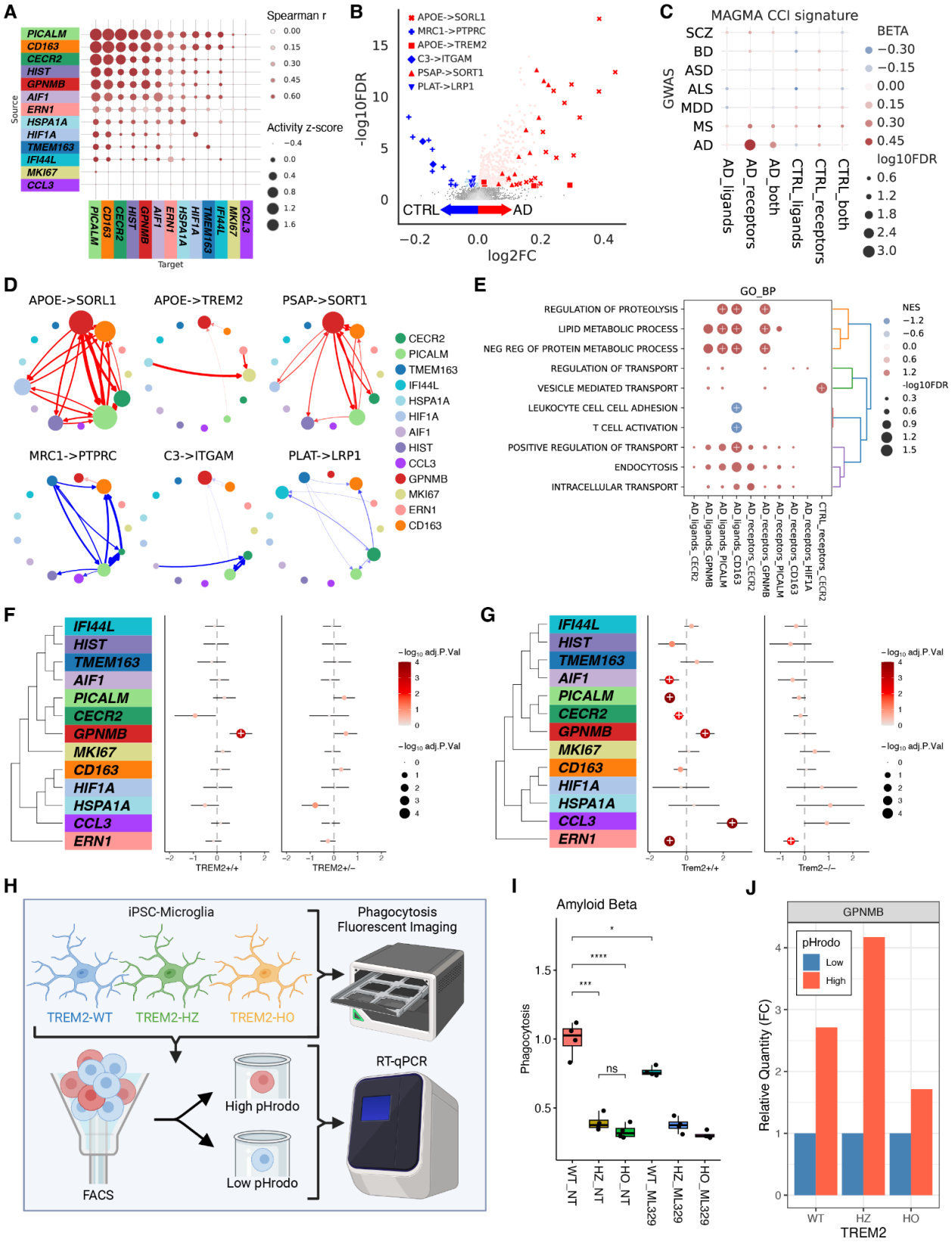

Figure 4. Non-cell-autonomous mechanisms. **(A)** Concordance of CCI scores among human myeloid cells between the FreshMG and the PsychAD cohorts. Pairwise Spearman correlation

using aggregated CCI scores by subtype. Row labels correspond to the sender or ligand-producing cell. Column labels correspond to the receiver or receptor-producing cell. **(B)** Differential CCI analysis based on Braak stages. Meta-analysis of linear mixed model regression using both FreshMG and PsychAD cohorts. Estimated log fold change corresponds to increased representation in the high Braak stage (red) vs. the low Braak stage (blue). **(C)** MAGMA enrichment analysis on differential CCI, stratified by direction of regulation (AD vs CTRL) and role of interaction (ligands, receptors, or both). **(D)** Directed network visualization of the top CCI pairs. Top: AD-associated, Bottom: controls-associated CCIs. Nodes represent each subtype and directional edge weights represent the importance of interaction. The edge color represents the estimated log fold change from differential CCI analysis. **(E)** Gene set enrichment analysis of CCI pairs using Gene Ontology Biological Processes. CCIs aggregated by subtype, direction of regulation (AD vs CTRL), and role of interaction (ligands or receptors). The color scale represents the normalized enrichment score (NES). The dot size represents the FDR significance. + marks FDR < 0.05. **(F)** Compositional variation of myeloid subtypes by AD using *TREM2* missense mutation (R47H or R62H) carriers. Shared disease-free controls without TREM2 mutations were compared against AD cases with *TREM2* WT (+/+) and *TREM2* missense carriers (+/-). AD cases were sampled to match the size of *TREM2* mutation carriers. **(G)** Compositional variation of myeloid subtypes by AD using Trem2-deficient 5XFAD mice. Trem2+/+ 5XFAD and Trem2–/– 5XFAD mice were compared to disease-free control mice (Trem2+/+). **(H)** Schematic of isolating highly phagocytosing microglial cells using flow cytometry. **(I)** Relative level of phagocytosis among WT, *TREM2* heterozygous, and homozygous knockouts in iPSC-derived microglia using Aβ as substrates. **(J)** Relative mRNA expression of *GPNMB* measured by RT-qPCR for high and low phagocytosing microglia using Aβ as substrates.

535 # Discussion

536 The cell atlas presented here underscores the importance of the functional plasticity of
537 human myeloid cells throughout life, reflecting their ability to dynamically adapt to their
538 microenvironment. Our comprehensive analyses uncover striking similarities between normal
539 aging and AD pathology. We speculate that the natural aging process is accelerated in AD, and
540 follows a similar trend for all subtypes, with the exception of the AD-associated microglia,
541 ADAM. ADAM is characterized by elevated expression of *GPNMB* transcripts and *CD44*
542 protein. *GPNMB* is a multifaceted transmembrane protein involved in the regulation of
543 inflammation and is implicated in several neurodegenerative diseases (*41–45*). When cleaved
544 by proteases into its soluble form, *GPNMB* signals by binding to the *CD44* receptor to drive
545 anti-inflammatory responses (*42*, *46*, *47*). Based on the following three main outcomes, our
546 results collectively suggest that ADAM is involved in anti-inflammatory responses and confer
547 neuroprotective benefits in AD.

548 First, ADAM shows a marked increase in prevalence with AD progression and correlates
549 significantly with polygenic AD risk scores. It suggests that individuals with higher AD genetic
550 predisposition may naturally exhibit increased activation of this subtype, positioning it as a
551 potential biomarker for disease progression and reflecting an adaptive, though limited,
552 neuroprotective response to neurodegenerative changes. This is consistent with small-scale
553 studies supporting *GPNMB* as a cerebrospinal fluid biomarker for the early diagnosis and
554 prognosis of AD (*48*, *49*). The significant increase in ADAM, driven by polygenic AD risk and
555 mediated by Aβ accumulation, reveals the intricate interplay between genetic predisposition
556 and cellular responses during AD progression. This association underscores the potential for
557 targeted therapeutic strategies that modulate the ADAM subtype, potentially altering disease
558 progression by mitigating the downstream effects of Aβ accumulation.

559 Second, we investigated cell-intrinsic factors that distinguish transcriptomic profiles
560 between AD cases and controls. Through GRN analysis, we prioritized *MITF* as the master
561 regulator of AD risk signatures, governing the expression of numerous AD-associated genes,
562 including *APOE*, *DPYD*, *TREM2*, and *PTPRG* (*12*, *50*, *51*). The *MITF* network is notably enriched
563 with markers of phagocytic activity and has been recognized as a crucial regulator of
564 homeostatic microglial functions, particularly in promoting autophagic states and enabling
565 microglia to migrate, detect, and clear Aβ/Tau proteinopathies (*22*, *23*, *52–54*). We confirmed
566 that *MITF* is the upstream regulator of *GPNMB* and demonstrated that the activation of
567 *GPNMB* is linked to increased phagocytosis. Prior work demonstrating the expression of
568 *GPNMB* is dependent on phagocytosis of CNS-substrates (*23*), indicative of a positive
569 feedback loop between *GPNMB* expression and phagocytosis.

570 Third, we examined non-cell-autonomous mechanisms that distinguish interactions and
571 communication pathways influencing AD progression. The significant enrichment of AD genetic
572 risk loci (*APP*, *TREM2*, *SORL1*, *SORT1*, *ABCA1*, *TSPAN14*) within the prioritized receptors of
573 AD-associated CCIs suggests potential mechanisms behind their contribution to AD. We
574 prioritize ADAM as a central hub in AD progression, participating in the highest number of AD-
575 associated ligand-receptor interactions among microglia subtypes. Motivated by the AD-
576 associated upregulation of *APOE-TREM2* ligand-receptor interactions in ADAM, we

subsequently found that *TREM2* mutations diminish ADAM microglia, highlighting the dependency of this subtype on *TREM2* function. Corroborating previous observations (*23*, *35*), we demonstrate that phagocytosis is *TREM2*-dependent and regulated through *MITF*-mediated activation of *GPNMB*, reinforcing the importance of this pathway in maintaining microglial function and neuroprotection.

In conclusion, our study advances the field by providing a high-resolution view of human myeloid cell diversity and their adaptive roles in aging and AD. The identification of subtype-specific GRNs, including the *MITF-GPNMB* axis, that are *TREM2*-dependent, highlights promising therapeutic avenues for modulating microglial functions to potentially slow disease progression. Future studies should aim to validate these pathways in humanized models and explore pharmacological strategies that enhance neuroprotective myeloid subtypes, potentially altering the trajectory of AD and related diseases.

Methods

Sources and description of human biosamples

All brain specimens were obtained through informed consent via brain donation programs at the respective organizations. All procedures and research protocols were approved by the respective ethical committees of our collaborator's institutions. The FreshMG samples (n = 137) were taken from 96 fresh postmortem autopsy samples obtained at the Mount Sinai/JJ Peters VA Medical Center NIH Brain and Tissue Repository (NBTR) in the Bronx, NY. An additional set of 41 fresh postmortem autopsy samples was obtained from participants in the Religious Orders Study or Rush Memory and Aging Project (ROSMAP) at Rush Alzheimer's Disease Center (RADC) in Chicago, IL. Both studies were approved by an Institutional Review Board of Rush University Medical Center and all participants signed informed and repository consents and an Anatomic Gift Act (*55*). The PsychAD cohort comprises 1,470 donors from three brain banks, Mount Sinai NIH Brain Bank and Tissue Repository (MSSM; 1,023 samples), NIMH Human Brain Collection Core (HBCC; 295 samples), and ROSMAP (RUSH; 152 samples). Finally, LivingMG biopsies were collected from patients undergoing procedures for intracerebral hemorrhage evacuation (STUDY-18-01012A), as described previously (*9*).

Collection and harmonization of clinical, pathological, and demographic metadata

Since the brain tissue specimens were collected from three different sites, the available clinical data varies as a function of source. As such, we used the following scheme to harmonize available clinical, pathological, and demographic metadata: the CERAD scoring scheme for neuritic plaque density (*19*) was harmonized for consistency across multiple brain banks, where the scores range from 1 to 4, with increasing CERAD number corresponding to an increase in AD burden; 1 = no neuritic plaque (normal brain), 2 = sparse (possible AD), 3 = moderate (probable AD), 4 = frequent (definite AD). Samples from ROSMAP used consensus summary diagnosis of no cognitive impairment (NCI), mild cognitive impairment (MCI), and dementia and its principal cause, Alzheimer's dementia (*56–58*). MSSM/VA samples used clinical dementia rating (CDR), which was based on a scale of 0-5; 0 = no dementia, 0.5 = questionable dementia (very mild), 1 = mild dementia, 2 = moderate dementia, 3=severe dementia, 4 = profound dementia, 5 = terminal dementia. After consulting with clinicians, we created a harmonized ordinal variable where dementia is categorized into three levels of cognitive decline, independent of AD diagnosis; 0 = no cognitive impairment, 0.5 = MCI (mild cognitive impairment), and 1 = dementia. In addition to AD phenotype, we collected comprehensive demographic (age, sex, and genetic ancestry) and technical variables (brain bank, sequencing facility, sequence pooling information, postmortem interval (PMI; measured in minutes), APOE genotype) to describe each cohort (**Supplementary Fig. S1**, **Supplementary Table S3-4**).

629 **Clinical diagnosis of AD**

630 For analysis comparing donors with AD cases and neurotypical controls, a binary clinical
631 diagnosis variable for AD, **dx_AD**, was defined as follows. Individuals with CERAD 2, 3, or 4,
632 Braak ≥ 3, and CDR ≥ 1 for MSSM/VA or Alzheimer's dementia for ROSMAP were classified as
633 AD cases. Controls were defined as individuals with CERAD 1 or 2 and Braak 0, 1, or 2.
634

635 **Measuring AD neuropathology**

636 For analysis comparing donors with pathologic AD, the following variables were used to
637 measure the severity of AD neuropathology. **CERAD score** (*19*). A quantitative measure of Aβ
638 plaque density where 1 is normal, 2 is possible AD, 3 is probable AD, and 4 is definite AD (*56*).
639 **Braak AD-staging score** measuring progression of neurofibrillary tangle neuropathology
640 (Braak & Braak-score, or BBScore). A quantitative measure of the regional patterns of
641 neurofibrillary tangle (NFT) density across the brain, where 0 is normal and asymptotic, 1-2
642 indicate initial stages where NFT begins to appear in the locus coeruleus and the
643 transentorhinal region, 3-4 indicate progression to limbic regions, such as the hippocampus
644 and amygdala, and 5-6 indicate NFT are widespread, affecting multiple cortical regions (*59–*
645 *61*).
646

647 **Measuring cognitive impairment**

648 For analysis comparing donors with AD-related dementia, the following variable was used
649 to measure the severity of cognitive impairment. **Clinical assessment of dementia.** A
650 harmonized variable of cognitive status based on CDR scale for MSSM/VA or NCI, MCI,
651 Alzheimer's dementia for ROSMAP. We used the three-level ordinal categories of clinical
652 dementia to measure the severity of dementia, in which 0 indicates no dementia, 0.5 indicates
653 minor cognitive impairment, and 1.0 indicates definite clinical dementia.
654

655 **Isolation and fluorescence-activated cell sorting (FACS) of microglia from fresh**
656 **brain specimens (FreshMG and LivingMG)**

657 Fresh brain tissue specimens were placed in tissue storage solution (Miltenyi Biotech,
658 #130-100-008) and stored at 4 ˚C for ≤ 48hrs before processing using the Adult Brain
659 Dissociation Kit (Miltenyi Biotech, #130-107-677), according to the manufacturer's instructions.
660 RNase inhibitors (Takara Bio, #2313B) were used throughout cell preparation. Following de-
661 myelination (Miltenyi Myelination removal beads - Miltenyi Biotech, #130-096-433) cells were
662 incubated in antibody (CD45: BD Pharmingen, Clone HI30, #555483 and CD11b: BD
663 Pharmingen, Clone ICRF44, #560914) at 1:500 for 1 hour in the dark at 4 ˚C with end-over-end
664 rotation. Prior to fluorescence-activated cell sorting (FACS), DAPI (Thermoscientific, #62248)
665 was added to facilitate the selection of viable cells. Viable (DAPI negative) CD45/CD11b
666 positive cells were isolated by FACS using a FACSAria flow cytometer (BD Biosciences).
667 Following FACS, cellular concentration and viability were confirmed using a Countess
668 automated cell counter (Life technologies).
669

670 **Isolation and fluorescence-activated nuclear sorting (FANS) of nuclei from frozen**
671 **brain specimens (PsychAD), with hashing**
672 All buffers were supplemented with RNAse inhibitors (Takara, #2313B). 25 mg of frozen
673 postmortem human brain tissue was homogenized in cold lysis buffer (0.32 M Sucrose, 5 mM
674 $CaCl_2$, 3 mM Magnesium acetate, 0.1 mM, EDTA, 10 mM Tris-HCl, pH8, 1 mM DTT, 0.1%
675 Triton X-100) and filtered through a 40 µm cell strainer. The flow-through was underlaid with
676 sucrose solution (1.8 M Sucrose, 3 mM Magnesium acetate, 1 mM DTT, 10 mM Tris-HCl, pH8)
677 and centrifuged at 107,000 g for 1 hour at 4 ˚C. Pellets were resuspended in PBS
678 supplemented with 0.5% bovine serum albumin (BSA). 6 samples were processed in parallel.
679 Up to 2 M nuclei from each sample were pelleted at 500 g for 5 minutes at 4 ˚C. Nuclei were re-
680 suspended in 100 µl staining buffer (2% BSA, 0.02% Tween-20 in PBS) and incubated with 1
681 µg of a unique TotalSeq-A nuclear hashing antibody (Biolegend) for 30 min at 4 ˚C. Prior to
682 FANS, volumes were brought up to 250 µl with PBS and 7aad (Invitrogen, #00-6993-50) added
683 according to the manufacturer's instructions. 7aad positive nuclei were sorted into tubes pre-
684 coated with 5% BSA using a FACSAria flow cytometer (BD Biosciences).
685
686 **scRNA-seq and CITE-seq library preparation (FreshMG and LivingMG)**
687 Following FACS, 10,000 cells were processed using 10x Genomics single cell 3' capture
688 reagents (10x Genomics, #1000268), according to the manufacturer's instructions. In parallel,
689 CITE-seq was performed on a subset of samples (n = 3 donors, n = 8 replicates per donor)
690 using the TotalSeq™-A Human Universal Cocktail (BioLegend, #399907) with 154 unique cell
691 surface antigens, including principal lineage antigens, and includes 9 isotype control antibodies
692 to survey surface antigens. CITE-seq was performed according to the manufacturer's
693 instructions. For the CITE-seq experiment, a total of 80,000 cells were loaded on 10x
694 Genomics B chips (10,000 of each uniquely barcoded sample aliquot per B chip lane), with a
695 total targeted recovery of around 40,000 cells.
696
697 **snRNA-seq and hashing library preparation (PsychAD)**
698 Following FANS, nuclei were subjected to 2 washes in 200 µl staining buffer, after which
699 they were re-suspended in 15 µl PBS and quantified (Countess II, Life Technologies).
700 Concentrations were normalized and equal amounts of differentially hash-tagged nuclei were
701 pooled. A total of 60,000 (10,000 each) pooled nuclei were processed using 10x Genomics
702 single cell 3' v3.1 reagents (10x Genomics, #1000268). Each pool was run across x2 10x
703 Genomics lanes to create a technical replicate. At the cDNA amplification step (step 2.2) during
704 library preparation, 1 µl 2 µm HTO cDNA PCR "additive" primer v3.1 was added (*62*). After
705 cDNA amplification, supernatant from 0.6x SPRI selection was retained for HTO library
706 generation. cDNA library was prepared according to the 10x Genomics protocol. HTO libraries
707 were prepared as previously described(*62*). cDNA and HTO libraries were sequenced at NYGC
708 using the Novaseq platform (Illumina).
709

710 **Processing of scRNA-seq data (FreshMG and LivingMG)**

711 We developed a tracking platform to record all technical covariates (such as 10x Genomics
712 kit lotnumber, dates of different preparations, viable cell counts, etc.) and quality metrics
713 derived from data preprocessing. **Alignment**. Paired-end scRNA-seq reads were aligned to the
714 hg38 reference genome and the count matrix was generated using 10x cellranger count
715 (v7.0.0). Subsequently, we used the CellBender (*63*) to carefully separate out true cells from
716 empty droplets with ambient RNA from raw unfiltered cellranger output. **QC**. We performed the
717 downstream analysis by aggregating gene-count matrices of multiple samples. A battery of QC
718 tests was performed to filter low-quality libraries and non-viable cells within each library using
719 Pegasus (v1.7.0)(*64*). Viable cells were retained based on UMI (1,000 ≤ n_UMI ≤ 40,000), gene
720 counts (500 ≤ n_genes ≤ 8,000), and percentage of mitochondrial reads (percent_mito ≤ 20).
721 We also checked for possible contamination from ambient RNA, a fraction of reads mapped to
722 non-mRNA like rRNA, sRNA, pseudogenes, and known confounding features such as lncRNA
723 MALAT1. Further filtering was carried out by removing doublets using the Scrublet method
724 (*65*). After filtering, the retained count matrix was normalized and log-transformed. Batch
725 correction. We assessed the correlation between all pairs of technical and biological variables
726 using Canonical Correlation Analysis and used the Harmony method (*66*) to regress out
727 unwanted confounding variables such as the source of brain tissue. Clustering. From the kNN
728 graph calculated from the PCA, we clustered cells in the same cell state using Leiden (*67*)
729 clustering. We use UMAP (*68*) for the visualization of resulting clusters. Cells identified as T
730 cells, NK cells, monocytes, neutrophils, oligodendrocytes, and astrocytes were removed, and
731 those identified as microglia and PVMs were carried forward for subsequent taxonomic
732 analysis. **Annotation of LivingMG**. After subsetting the data for microglia and PVMs, we used
733 myeloid taxonomy from the FreshMG dataset as reference to annotate the LivingMG dataset.
734 We used the same set of highly variable genes from the FreshMG dataset and employed
735 scANVI (*69*) to transfer both subclass and subtype level annotations (**Supplementary Fig.
736 S3J**).
737

738 **Processing of snRNA-seq data (PsychAD)**

739 **Alignment**. Samples were multiplexed by combining 6 donors in each nuclei pool using
740 hashing, and each biosample was processed in duplicate to produce technical replicates.
741 Paired-end snRNA-seq libraries were aligned to the hg38 reference genome using STAR solo
742 (*70*, *71*) and multiplexed pools were demultiplexed using genotype matching via vireoSNP (*72*).
743 After per-library count matrices were generated, the downstream processing was performed
744 using pegasus v1.7.0 (*64*) and scanpy v1.9.1 (*73*). **QC**. We applied rigorous three-step QC to
745 remove ambient RNA and retain nuclei for subsequent downstream analysis. First, the QC is
746 applied at the individual nucleus level. A battery of QC tests was performed to filter low-quality
747 nuclei within each library. Poor-quality nuclei were detected by thresholding based on UMI
748 (1,179 ≤ n_UMI ≤ 200,000; determined based on median absolute deviation of n_UMI
749 distribution), gene counts (986 ≤ n_genes ≤ 15,000; determined based on median absolute
750 deviation of n_genes distribution), and percentage of mitochondrial reads (percent_mito ≤ 1).
751 We also checked for possible contamination from ambient RNA, the fraction of reads mapped

752 to non-mRNA like rRNA, sRNA, and pseudogenes, as well as known confounding features,
753 such as the lncRNA MALAT1. Second, the QC was applied at the feature level. We removed
754 features that were not robustly expressed in at least 0.05% of nuclei. Lastly, the QC was
755 applied at the donor level. We removed donors with very low nuclei counts, which can
756 introduce more noise to the downstream analysis. We also removed donors with low genotype
757 concordances. Further filtering was carried out by removing doublets using the Scrublet
758 method (*65*). **Batch correction**. We assessed the correlation between all pairs of technical
759 variables using Canonical Correlation Analysis and used the Harmony method (*66*) to regress
760 out unwanted variables such as the effect of brain tissue sources. **Clustering**. Highly variable
761 features were selected from mean and variance trends, and we used the k-nearest-neighbor
762 (kNN) graph calculated on the basis of harmony-corrected PCA embedding space to cluster
763 nuclei in the same cell type using Leiden (*67*) clustering algorithms. We used UMAP (*68*) for the
764 visualization of the resulting clusters. **Isolation of myeloid cells**. Identified cell-type clusters
765 were annotated based on manual curation of known gene marker signatures obtained from
766 Human Cell Atlas and human DLPFC study (*74*). Classes of immune cells, including Microglia
767 and PVM, were isolated and subjected to myeloid subtype annotation and downstream
768 analysis.
769

770 **Processing of bulk RNA-seq data (BulkMG)**

771 RNA was extracted from aliquots of up to 100,000 FACS-sorted CD45+ microglia using the
772 Arcturus PicoPure RNA isolation kit (Applied Biosystems). RNA-sequencing libraries were
773 generated using the SMARTer Stranded Total RNA-Seq Kit v2 (Takara Bio USA, #634411).
774 Libraries were quantified by Qubit HS DNA kit (Life Technologies, #Q32851) and by quantitative
775 PCR (KAPA Biosystems, #KK4873) before sequencing on the Hi-Seq2500 (Illumina) platform
776 obtaining 2x100 paired-end reads.
777 Count matrices were generated using Kallisto pseudo-mapping (*75*) using the standard
778 Genecode v38 reference (starting with 235,227 transcripts for 60,535 unique genes). For gene-
779 level analyses, 21,856 features were retained for downstream analyses after filtering for
780 features with CPM > 1 in at least 15% of samples. Correct identity of the samples was
781 confirmed by concordance between the genetic variants obtained from RNA-seq with those
782 obtained from ATAC-seq, or directly available genotypes, as available.
783

784 **Spatial validation using Akoya PhenoCycler**

785 FFPE sections from both AD and control cases were used for the Akoya PhenoCycler
786 experiment. The experiments were performed according to the manufacturer's protocol, with
787 the Neuroinflammation Module, Neuroscience Core Panel and Immune Module provided by
788 Akoya. Briefly, samples were deparaffinized and hydrated. For antigen retrieval, samples were
789 boiled in Tris-EDTA pH 9 for 20 minutes in a programmable pressure cooker. Samples were
790 stained in Antibody Cocktail Solution containing antibodies (**Supplementary Table S5**) and
791 PhenoCycler Blocking Buffer. Following staining, samples were washed, fixed, and loaded on
792 the PhenoCycler, with data generated using the automatic workflow. Akoya PhenoCycler
793 results were saved as .qpproj files. and protein expression quantified using QuPath (*76*). After

794 the sections were annotated, cells were segmented with the QuPath extension StarDist
795 fluorescent cell detection script, with dsb2018_paper.pb as a training model. Protein
796 expression was quantified using raw channel intensity with spatial boundaries of cells inferred
797 by export measurement and export detection commands using QuPath.
798

799 **Spatial transcriptomic characterization using Xenium *in situ***

800 **Custom panel design**. Xenium Human Brain Gene Expression Panel (10x Genomics,
801 #1000599) and a custom panel of 100 genes (**Supplementary Table 16**) were selected for the
802 Xenium experiment. The 100-gene custom panel consisted mainly of subclass markers
803 selected based on specificity and gene expression level. The custom gene list was sent to 10X
804 genomics and the probe design was performed using their in-house pipeline. **Tissue**
805 **preparation**. Fresh frozen tissue specimens of DLPFC were dissected into small blocks on ice.
806 Tissue blocks were snap frozen by submerging in an isopentane (Sigma-Aldrich, #320404-1L)
807 bath chilled with dry ice and stored at -80 ˚C. Before cryosectioning, tissue blocks were
808 allowed to equilibrate to the cryostat (Microm, #HM505) chamber temperature, and were
809 mounted with OCT (Tissue-Tek® O.C.T. Compound, Sakura Finetek USA, #4583). After
810 trimming, good quality 10 µm sections were flattened on the cryostat stage and placed on pre-
811 equilibrated Xenium slides (Xenium Slides & Sample Prep Reagents, 10x Genomics,
812 #1000460). 2-3 sections were placed on each slide. Sections were further adhered to by
813 placing a finger on the backside of the slide for a few seconds and were then refrozen in the
814 cryostat chamber. Slides were sealed in 50 ml tubes and stored at -80˚C until Xenium sample
815 preparation. **Sample preparation**. Xenium sample preparation was performed according to the
816 manufacturer's protocol; "*Xenium In Situ for Fresh Frozen Tissues – Fixation &*
817 *Permeabilization, CG000581, Rev C*" and *"Xenium In Situ Gene Expression - Probe*
818 *Hybridization, Ligation & Amplification, User Guide, CG000582, Rev C*''. Briefly, fresh frozen
819 sections mounted on Xenium slides from the previous step were removed from -80 ˚C storage
820 on dry ice prior to incubation at 37 ˚C for 1 min. Samples were then fixed in 4%
821 paraformaldehyde (Formaldehyde 16% in aqueous solution, VWR, #100503-917) in PBS for 30
822 min. After rinsing in PBS, the samples were permeabilized in 1% SDS (sodium dodecyl sulfate
823 solution) for 2 min and then rinsed in PBS before being immersed in the pre-chilled 70%
824 methanol and incubated for 60 min on ice. After rinsing the samples in PBS, the Xenium
825 Cassettes were assembled on the slides. Samples were incubated with a probe hybridization
826 mix containing both the Xenium Human Brain Gene Expression Panel (10x Genomics,
827 #1000599) and the 100 custom gene panel at 50 ˚C overnight to allow the probes to hybridize
828 to targeted mRNAs. After probe hybridization, samples were rinsed with PBST, and incubated
829 with Xenium Post Hybridization Wash Buffer at 37 ˚C for 30 min. Samples were then rinsed with
830 PBST and a ligation mix was added. Ligation was performed at 37 ˚C for 2 hrs to circularize the
831 hybridized probes. After rinsing the samples with PBST, Amplification Master Mix was added
832 to enzymatically amplify the circularized probes at 30 ˚C for 2 hrs. After washing with TE buffer,
833 auto-fluorescence was quenched according to the manufacturer's protocol and nuclei stained
834 with DAPI prior to Xenium *in situ* analysis. Nuclear segmentation. The prepared samples were
835 loaded into the Xenium analyzer and run according to manufacturer's instructions "*Xenium*

Analyzer User Guide CG000584 Rev B". After the Xenium analyzer was initiated, the correct gene panel was chosen, and decoding consumables (Xenium Decoding Consumables, 10x Genomics, #1000487) and reagents (Xenium Decoding Reagents, 10x Genomics, #1000461) were loaded. The bottom of the slides was carefully cleaned with ethanol prior to loading. Once the samples were loaded and the run was initiated, the instrument scanned the whole sample area of the slides using the DAPI channel, and regions of interest were selected to maximize the capture area. Results were generated by the instrument using default settings. By default, the Xenium analyzer uses 15 μm nuclei expansion distance for segmentation of cells. To test the idea of nuclei only segmentation, we resegment the results with 0 μm nuclei expansion, by using the Xenium ranger and the following scripts:

```
xeniumranger resegment --id=demo --xenium-bundle=/path/to/xenium/files
--expansion-distance=0 --resegment-nuclei=True
```

Identification of myeloid cells. After generating the cell-by-gene count matrices based on nuclear segmentation, nuclei were filtered by the number of detected transcripts (n_counts ≥ 30). The count matrices from all samples were merged, log-normalized, and subjected to PCA, kNN graph calculation, and Leiden clustering. To assign major cell type labels to each cell, we combined this unsupervised clustering approach with supervised label transfer with scANVI (*69*). In short, nuclei from the RADC dataset (a subset of the full PsychAD study) with known labels for eight major CNS cell types and 27 subclass labels were used as a reference to assign labels to all cells in the unfiltered Xenium dataset. Then, we assigned labels to each Leiden cluster according to the following criteria - any cluster containing >90% of cells with a single label was assigned that label; all other clusters were removed from further analysis. In addition, cells within retained clusters were removed if their individual scANVI label did not match the label assigned to their cluster. To retain a pure microglia and PVM nuclei population, we first filtered the Xenium data for the Immune class. This population was further filtered based on the label transfer of PsychAD subclasses, to retain only nuclei with the "Microglia" and "PVM" subclass labels. This filtered data (~24,000 nuclei) was then re-processed and normalized up to PCA computation, followed by integration with batch correction using harmony (*66*), with the batch label set as the ID of the Xenium slide (each slide contained 2-3 tissue samples), and corrected for variation in the number of detected transcripts per nucleus. The top 30 harmony-corrected PCs were then used for neighbor graph calculation, UMAP visualization, and Leiden clustering. **Taxonomy of myeloid cells**. To identify subtypes of myeloid cells in the Xenium data, we relied on the scANVI label transfer method. We used the PsychAD cohort as a reference since we expected it to be more similar to our Xenium data than the FreshMG cohort (since the PsychAD cohort was also frozen *in situ*, and contains only nuclear transcripts). Label transfer was performed for subclass (subtype) annotation as described below. However, due to the high degree of transcriptional similarity between microglia sub-populations, as well as the relative sparsity of measured informative genes, we adopted a more stringent approach and assigned microglia subclass (subtype) labels based on the stability of obtained predictions. We ran scANVI for subclass (subtype) label transfer 23 (21) independent times, differing only by a randomly generated initial condition. Then, we defined

877 stably-predicted nuclei as those that had 17 (16) predictions in internal agreement, and
878 assigned "unstable" labels to nuclei whose combined predictions did not fulfill this condition.
879 Subclass predictions were subsequently refined to obtain stable subtype prediction by
880 subsetting the dataset to Homeo (or Adapt) stably predicted nuclei and running 10
881 independent subtype-level predictions per subset, with predictions being accepted as stable
882 with 8 or more consistent "votes". **Consensus subclass and subtype labels from stability**
883 **analysis.** To further strengthen the reliability of our predictions, we attempted to combine our
884 microglia subclass and subtype prediction into a single consensus. Of note, consensus labels
885 could be either at the subclass or subtype level, depending on the set of predicted labels
886 obtained for a given nucleus. Our consensus voting process began by assigning pseudo-
887 subclasses to nuclei from the subtype predictions, by asking whether at least 16 (out of 21)
888 subtype predictions agree for a given nucleus at the subclass level (even if the subtype
889 prediction was "unstable"). Next, cells were assigned a subclass label if the 2 subclass
890 predictions did not contradict each other (i.e., they either agreed, or one method had a stable
891 prediction and the other was unstable). Cells with stable subclass predictions by this
892 methodology were then further assigned a subtype if their subtype predictions were similarly
893 stable and consistent. Based on these criteria, ~76% of microglia were stably assigned a
894 subclass. Subtype annotation, however, proved more challenging, and many cells were not
895 stably assigned to a single subtype in this analysis. **Label transfer from snRNA-seq data**
896 **using scANVI.** Throughout this work, we utilize scANVI to perform reference-based label
897 transfer as a way to assist in identifying pre-defined populations on cells. In each such
898 instance, we performed the following steps. First, snRNA-seq gene expression data was
899 subset to the genes also measured in our Xenium data. Next, we used the scvi-tools package
900 (*77*, *78*) to train machine learning models for dimensionality reduction based on the reference
901 dataset and its assigned labels (e.g., class and subclass labels from the PsychAD cohort).
902 Unless stated otherwise, model training was run with the following parameters. scVI models
903 were run with 5 layers and 20 latent variables (30 for microglia sub-populations) and were
904 trained for 50 (75) epochs; scANVI models were trained for 50 epochs with a minimal sample of
905 100 cells per cluster per epoch; transfer models were trained for 100 epochs. Following
906 training, the model was applied to query Xenium data to assign labels. To assess the
907 performance of each transfer model, we performed a "self label transfer", predicting labels in
908 the reference data (using the subset gene pool) and evaluated the rate of correct prediction
909 and biases in label misassignment for each predicted category. Where appropriate, we also
910 computed the Pearson correlation coefficients for gene expression between the reference and
911 query data, limited to the shared subset of genes across predicted labels.
912

913 **Preparation of phagocytosis substrates**

914 **Myelin**. Human myelin was isolated from human brain tissue using a modified protocol (*23*,
915 *79*). Dissecting media [RPMI (Sigma, #R8758), 10% FBS (Avantor, #97068-091), 0.4 mg/mL
916 collagenase (Sigma, #10269638001), 2 mg/mL DNAse I (Sigma, #10104159001)] was
917 preheated in a 12-well tissue culture plate (Corning, #3513) in a 37 ˚C incubator. Using a
918 scalpel, 75-125 mg of human brain white matter was minced and transferred to the preheated

919 dissecting media and incubated at 37 ˚C for 30 minutes, pipetting the solution after 15 minutes.
920 After 30 minutes, brain homogenate was transferred to a 2 mL Dounce homogenizer (Kimble,
921 #885302) on ice, homogenized, sieved using a 40 µm cell strainer (Greiner, #542040) and
922 transferred to a 15 mL conical tube. The homogenate was centrifuged at 400 x g for 10
923 minutes at 4 ˚C and the resulting pellet resuspended in 1.5 mL Ca^{2+}/Mg^{2+}-free DPBS (Gibco,
924 #14200075). This was combined with 500 µL of fresh isotonic percoll solution [1 part
925 Ca^{2+}/Mg^{2+}-free DPBS, 9 parts Percoll (Cytiva, #17-0891-02)] and mixed by pipetting. 2 mL of
926 DPBS was gently layered on top of the Percoll-homogenate solution creating two separate
927 layers. The solution was then centrifuged at 3000 x g for 10 minutes at 4 ˚C resulting in a disc
928 of myelin between the lower and upper layers of Percoll and DPBS. The myelin was transferred
929 to a new 1.5 mL tube and centrifuged at max speed for 10 minutes at 4 ˚C. The myelin pellet
930 was washed twice with DPBS and protein concentration measured using the Pierce Rapid
931 Gold BCA Protein Assay Kit (Pierce, #A53225). **Synaptic protein**. Human synaptic protein was
932 isolated from fresh human brain tissue using the Syn-PER Synaptic Protein Extraction Reagent
933 protocol (ThermoFisher, #87793). Human brain tissue was homogenized in Syn-PER Reagent
934 and synaptic protein isolated by centrifugation. **Amyloid beta**. Amyloid-β (Aβ) was aggregated
935 using the Beta Amyloid (1-42) Aggregation Kit (rPeptide, #A-1170-025) according to the
936 manufacturer's protocol. In brief, lyophilized Aβ was reconstituted and incubated at 37 ˚C
937 overnight to allow for protein aggregation. After 24 hours, aggregates were collected by
938 centrifugation and the pellet was rinsed once in 1 mL Ca^{2+}/Mg^{2+}-free DPBS (Gibco, #14200075)
939 before being resuspend in 200 µL of filtered 0.1 M sodium bicarbonate (Sigma, #S5761) for
940 pHrodo labeling. **pHrodo Labeling.** Isolated myelin, synaptic protein, and aggregated amyloid-
941 beta was labeled using 1 µL (10.2 mM) pHrodo Red SE (Fisher, #P36600) per 1 mg of protein
942 and incubated for 1 hour at room temperature protected from light. Labeled protein was then
943 washed three times with DPBS before resuspending in PBS to a 100x stock concentration
944 (1.25 mg/mL) and stored at -20 ˚C until further use. **Apoptotic neurons**. Apoptotic neurons
945 were prepared using a modified protocol (*23*, *80*). SH-SY5Y neurons (ATCC, #CRL-2266) were
946 seeded in 6-well tissue culture-treated corning plates and grown to confluence. To induce
947 apoptosis, SH-SY5Y cells were placed inside a tissue culture biosafety cabinet without the
948 plate cover and exposed to 60 lux of UV light for 1 min. UV lux was determined by Digital Lux
949 Meter (Dr. Meter, # LX1010B). Neurons were harvested by pipetting with 1 mL Ca^{2+}/Mg^{2+}-free
950 DPBS (Gibco, #14200075) and washed twice in PBS. Cell pellets were resuspended in 1 mL
951 PBS supplemented with 2 µL (10.2 mM) pHrodo Red SE (Fisher, #P36600) and incubated for
952 15 minutes at room temperature in the dark. Labeled neurons were washed twice in PBS
953 +20% FBS to remove any unbound pHrodo, resuspended in PBS, and counted using a
954 Countess II FL automated cell counter (ThermoFisher). Aliquots of labeled apoptotic neurons
955 were stored at -80 ˚C until used.
956

957 **Validation of GPNMB and MITF**

958 **HMC3 Cell Line Maintenance**. The HMC3 human immortalized microglia line (ATCC,
959 #CRL-3304) was maintained in Minimum Essential Medium (MEM) (Gibco, #11095098)
960 supplemented with 10% heat inactivated Fetal Bovine Serum (FBS) (Avantor, #97068-091) and

961 100 U/mL Penicillin-Streptomycin (Gibco, #15140122). Cells were maintained in 10 cm dishes
962 (ThermoFisher, #150466) and passaged by trypsinization (Gibco, #25200072). **Lentiviral**
963 **Transduction of dCas9-VPR**. The dCas9-VPR effector system was expressed in HMC3 cells
964 via lentiviral transduction. The lenti-EF1a-dCas9-VPR-Puro (Addgene, #99373) plasmid was
965 packaged into lentivirus using the VectorBuilder lentiviral packaging service, and stable cell
966 lines were generated according to the manufacturer's instructions
967 (https://www.addgene.org/protocols/generating-stable-cell-lines/). Parent lines expressing the
968 dCas9-VPR system were clonalized, and dCas9 expression confirmed by qPCR. **Guide RNA**
969 **Design and Preparation**. Guide RNA design and preparation protocols were adapted from the
970 previously established protocols by Li and colleagues (*81*). Guide RNA (gRNA) sequences for
971 MITF and GPNMB were identified by searching the CRISPR-ERA database for "gene
972 activation" using the most up-to-date human reference genome (Human GRCh37/h19). Genes
973 were searched indicating "U6 promoter" given our specific gRNA cloning vector. gRNA
974 sequences with the highest efficiency and specificity ("E+S") scores were selected and
975 confirmed to have no off-target binding using the Cas-OFFinder database
976 (http://www.rgenome.net/cas-offinder/). gRNA sequences were then cloned into the
977 lentiGuide-Hygro-mTagBFP2 (Addgene, #99374) backbone using Golden Gate Assembly for
978 digestion and ligation. Competent e. coli (NEB, #C3019I) were transformed using the gRNAs
979 cloned into the lentiGuide-Hygro-mTagBFP2 (Addgene, #99374) plasmid vector according to
980 the manufacturer's protocol for heat shock transformation. Transformed bacterial colonies
981 were grown on Ampicillin Agar (InvivoGen, #FAS-AM-S) at 37 ˚C overnight prior to inoculation
982 of liquid cultures (InvivoGen, #FAS-AM-B). Plasmid DNA was isolated using the Plasmid Mini
983 Kit (Qiagen, #12125) and subjected to sanger sequencing (Genewiz Azenta Life Sciences) to
984 confirm the presence of gRNA sequences. **Lentivirus Preparations**. Human embryonic kidney
985 cells (HEK293T) were used to package gRNA plasmids into lentivirus. Lentiviral production was
986 completed using a polyethyleneimine (PEI) (Polysciences, #23966-2) transfection strategy as
987 described by Li and colleagues (*81*). Transfections in HEK293T cells were performed in 15 cm
988 plates (Nunc, #150468) when cells reached approximately 80% confluency. A "PEI
989 transfection-mixture" of 110 µL PEI to 250 µL Opti-MEM (Gibco, #31985-062) was combined in
990 a 1:1 ratio with a "DNA-mixture" containing 250 µL Opti-MEM, 8.1 µg pMDLg/pRRE (Addgene,
991 #12251), 3.1 µg pRSV-Rev (Addgene, #12253), 4.1 µg pCMV-VSV-G (Addgene, #8454) and
992 12.2 µg gRNA plasmid DNA. PEI-mixture and DNA-mixtures were mixed and incubated at
993 room-temperature for 15 minutes. After incubation, 700 µL of the mixture was added to the
994 HEK293T cells and incubated at 37 ˚C for 6 hours before being replaced with 15 mL complete
995 media. After 48 hours of incubation, viral media was collected, stored at 4 ˚C and fresh HEK
996 media was replaced for an additional 24 hours incubation. Viral media was collected a second
997 time before concentrating with Lenti-X Concentrator (Takara, #631232) according to the
998 manufacturer protocol. Viral quantification was completed by isolating viral RNA using the
999 NucleoSpin RNA Virus Kit (Takara, #740956), and viral copies determined using the Lenti-X
1000 qRT-PCR Titration Kit (Takara, #631235). **CRISPR activation of MITF and GPNMB**. HMC3
1001 cells were plated in 96-well plates at a seeding density of 10,000 cells per well. After adhering
1002 overnight, cells were treated with gRNA-containing lentivirus at a final concentration of 3225

1003 viral copies/μL (based on qPCR). Cells were transduced with virus for 24 hours before
1004 removing vial media and replacing with hygromycin (1 mg/mL) antibiotic selection media for 48
1005 hours. **Phagocytosis**. Seventy-two hours after transduction, pHrodo-labeled substrate; myelin
1006 (5 μg/mL), amyloid-beta (5 μg/mL) or SHSY5Y Apoptotic Neurons (5000 cells/well) was added,
1007 and plates were imaged by Incucyte. Fluorescent intensity was recorded, capturing four
1008 images per well across two replicate wells. All conditions were plated in triplicate across two
1009 replicate plates and imaged after 24 hours. For RNA isolation and quantification of target genes
1010 by RT-qPCR, cells in replicate wells were harvested and pooled to increase RNA yield. **RT-**
1011 **qPCR**. HMC3 cells were harvested by trypsinization and RNA isolated using the Arcturus
1012 PicoPure RNA Isolation Kit (Applied Biosystems, #12204-01). RNA was quantified by
1013 NanoDrop (ThermoScientific, #840274100). RT-qPCR was performed using the Power SYBR
1014 Green RNA-to-CT 1-Step Kit (Applied Biosystems, #4389986) on the QuantStudio 5 Real-Time
1015 PCR System (Applied Biosystems, #A28135). qPCR primers were obtained from Integrated
1016 DNA Technologies (IDT), sequences for the PrimeTime qPCR Primers can be found in
1017 **Supplementary Table S16**.
1018

1019 **TREM2 validation using iPSC-derived microglia**

1020 **Preparation of iPSC-derived microglia**. Isogenic TREM2 wild-type (WT) (FujiFilm,
1021 #C1110), heterozygous knockout (HZ) (FujiFilm, #C1134), and homozygous knockout (HO)
1022 (FujiFilm, #C1136) lines were obtained from FujiFilm and maintained in iCell Culture media
1023 according to the manufacturer's protocols. TREM2 WT, HZ, and HO iCell microglia were plated
1024 at 125,000 cells/mL in Poly-D-Lysine (Gibco, #A3890401) coated plates according to the
1025 manufacturer's protocol. **Phagocytosis**. Cells were maintained in culture media for 72 hours
1026 before addition of phagocytosis substrates: amyloid-beta (5 μg/mL), myelin (5 μg/mL), synaptic
1027 protein (5 ug/mL), or apoptotic neurons (35,000/mL), with or without the MITF pathway
1028 inhibitor, ML329 (2 μM, MedChemExpress, #HY-101464)(*23*, *82*). Phagocytosis was assessed
1029 using the Sartorius Incucyte S3 Live-Cell Analysis System by imaging four fields per well. RFP
1030 was used to visualize and measure phagocytosed pHrodo-labeled substrate, while bright-field
1031 was used to estimate cell confluency. Phagocytosis was analyzed 24 hours after introduction
1032 of the substrate using the Incucyte analysis software. Statistical analyses were conducted in
1033 GraphPad Prism using two-tailed t-tests to compare phagocytosis across cell lines. **RT-qPCR**.
1034 For RT-qPCR analyses, cells were harvested by pipetting and prepared for RNA isolation using
1035 the Arcturus PicoPure RNA Isolation Kit (Applied Biosystems, #12204-01). RNA was quantified
1036 by NanoDrop (ThermoScientific, #840274100). RT-qPCR was performed on isolated RNA using
1037 the Power SYBR Green RNA-to-CT 1-Step Kit (Applied Biosystems, #4389986) on the
1038 QuantStudio 5 Real-Time PCR System (Applied Biosystems, #A28135). qPCR primers were
1039 obtained from Integrated DNA Technologies (IDT), sequences for the PrimeTime qPCR Primers
1040 can be found in **Supplementary Table S16**. **FACS**. For analysis of phagocytosis by flow
1041 cytometry, cells were harvested by pipetting before incubating with GPNMB Monoclonal
1042 antibody (Proteintech, #66926-1) at 1:1000 for 1 hour, followed by Goat anti-Mouse IgG (H+L)
1043 Cross-Adsorbed Secondary Antibody, Alexa Fluor™ 750 (ThermoFisher, #A-21037) at 1:1000
1044 for 30 minutes. Just prior to FACS, DAPI (ThermoFisher, #62248) was added at 1:10,000. Cells

were then analyzed by flow cytometry for fluorescence of pHrodo-positive phagocytosed substrate and for the presence of GPNMB protein. Cells were sorted into low and high substrate populations for RNA isolation and qPCR, as previously described.

Compositional variation analysis

We applied `crumblr` method (https://diseaseneurogenomics.github.io/crumblr) for testing the variation of cell type composition. Analysis of count ratio data (i.e., fractions) requires special consideration since data is non-normal, heteroskedastic, and spans a low-rank space. While counts can be considered directly using Poisson, negative binomial, or Dirichlet-multinomial models for simple regression applications, these can be problematic since they 1) can be very computationally expensive, 2) can produce poorly calibrated hypothesis tests, and 3) are challenging to extend to other applications. The widely used centered log-ratio (CLR) transform from compositional data analysis makes count ratio data more normal and enables use the of linear models and other standard methods. Yet CLR-transformed data is still highly heteroskedastic: the precision of measurements varies widely. This important factor is not considered by existing methods. `crumblr` uses a fast asymptotic normal approximation of CLR-transformed counts from a Dirichlet-multinomial distribution to model the sampling variance of the transformed counts. `crumblr` enables incorporating the sampling variance as precision weights to linear (mixed) models in order to increase power and control the false positive rate. `crumblr` also uses a variance stabilizing transform (vst) based on the precision weights to improve the performance of PCA and clustering.

Differential gene expression analysis

We applied `dreamlet` for differential expression analysis. Building from the previously developed statistical tool Dream (*83*), it applies linear mixed models to the differential expression problem in single-cell omics data. It starts by aggregating cells by the donor using a pseudobulk approach (*84*, *85*) and fits a regression model and cell. For each feature and cell cluster, the following mixed model was applied: `Gene expression ~ Intercept + age + (1|sex) + (1|ancestry) + PMI + (1|batch) + (1|source) + phenotype`, where categorical and numerical variables were modeled as random and fixed effects, respectively. We ran gene set analysis using the full spectrum of gene-level t-statistics (*86*).

Mediation analysis

Causal Mediation Analysis was performed using the mediation R package (*87*). From PsychAD cohort, we subsetted to 645 individuals with European ancestry who have AD phenotype variables and PRS calculations from the latest AD GWAS(*8*). For each regression, we used the following covariates:

```
Age + Sex + PMI + PC1 + PC2 + PC3 + PC4 + PC5 + PC6 + PC7 + PC8 + PC9
+ PC10
```

where PC1-10 indicate genotype PCs. For the subtype composition, we used CLR-transformed cell count fractions obtained from `crumblr` analysis. For bootstrapping, we used 10,000

simulations with 50th percentiles of the treatment variable used as the control condition and 90th percentile of the treatment variable used as the treatment condition.

Constructing gene regulatory networks

We inferred gene regulatory networks with the pySCENIC (v 0.12.1)(*31*, *32*) pipeline using a concatenated dataset of FreshMG and PsychAD microglia cohorts. We followed the standard SCENIC expression preprocessing; log normalizing expression counts and selecting highly variable genes (3,192 total) while accounting for batch correction between datasets with scanpy (v1.9.3). The pySCENIC's GRNboost2 (arboreto v0.1.6) method was utilized for gene regulatory network inference. The pySCENIC's cisTarget function with Human motif database v10 (https://resources.aertslab.org/cistarget/motif2tf/motifs-v10nr_clust-nr.hgnc-m0.001-o0.0.tbl) was used to enrich for gene signatures and pruned based on *cis*-regulatory cues using default settings. The "aucell" positional argument was utilized to find the enrichment of regulons across single cells.

To compare regulon enrichment between subtypes, the resulting AUCell matrix was z-score normalized. To assess the concordance between regulon enrichment across subtypes between FreshMG and PsychAD cohorts, we computed the Pearson correlations between normalized z-scores using the pandas `corrwith` function. For each dataset, we computed the normalized regulon enrichment Z-score, and performed a meta-analysis between two datasets using Stouffer's method.

To test whether there is a significant association between the target genes of a TF and disease signatures, we performed Fisher's exact tests between SCENIC GRN target genes and AD risk gene signatures, based on `Dreamlet` DEG analysis. Disease-associated genes with FDR < 0.05 were selected based on four different measures of AD severity, namely, case-control diagnosis, Braak, CERAD, and dementia status. The top 3 regulons were prioritized based on the overall enrichment of the AD DEG signature. The similarity between target genes of regulons was evaluated using the Jaccard similarity index. We found the target genes of the top 3 TFs shared high similarity and clustered distinctly from other regulons (**Supplementary Fig. S6B**). Node centrality was calculated using PageRank analysis, which measures a ranking of the nodes in the graph based on the structure of the incoming links (**Supplementary Fig. S6C**). The mean estimate and -log10FDR of target risk genes in SCENIC regulons are visualized using the importance score edge weights from GRNboost2 with networkX (v3.1). For each regulon, a list of SCENIC GRN TF target genes after cisTarget pruning were obtained and, using gseapy (v1.0.5)(*88*), tested for gene-set enrichment based on the Gene Ontology Biological Processes 2023 reference (*88*). GO terms were clustered based on their Ward distance between -log10FDR values.

Constructing a pseudotemporal trajectory of AD

We followed the same steps when constructing Braak-stage-informed pseudotimes for the FreshMG and PsychAD datasets, respectively. First, cells that were not assigned a Braak stage were excluded and the data subsetted to contain either only cells annotated as adaptive, homeostatic, ADAM, or PVM. We then computed a k-nearest-neighbor graph using Scanpy

(*73*) (`scanpy.pp.neighbors`, k = 30, n_pcs = 15) on the PCA embedding, regressed with Harmony. Finally, transport maps were computed between pairs of consecutive disease stages using moscot's TemporalProblem (*29*).

Identification of driver genes with CellRank 2

To identify drivers of disease progression within each cell type, we first estimated a cell-cell transition matrix T using the *`RealTimeKernel`* implemented in the CellRank framework (*30*). Disease stage heterogeneity within each Braak stage was accounted for by including cell-cell similarity (`conn_weight=0.1`). Since moscot relies on entropical regularization to solve the underlying optimal transport problem, it returns dense transport maps, leading to negligible transition probabilities and large memory requirements when computing the transition matrix. To render our downstream analysis computationally feasible, we thresholded the constructed transition matrix using the *`RealTimeKernel`*'s automatic thresholding scheme (`threshold="auto"`).

Based on the *`RealTimeKernel`*-derived transition matrix, we estimated terminal states with the GPCCA estimator (*30*, *89*). In the case of adaptive and homeostatic cells, we computed terminal states at the resolution of subclasses (MG_Adapt, MG_Homeo), for the PVM subset based on the subtype (PVM_CD163, ADAM_GPNMB) annotation. We confirmed the estimated terminal states as biologically plausible by quantifying the cell type and disease stage purity, respectively. Given n cells (n = 30 in this study) identifying a terminal state, the disease stage purity is defined as

$$\frac{|C \cap B_j|}{n},$$

with C denoting the set of cells identifying the terminal state, B_j the set of cells with Braak stage j, and $|\cdot|$ the cardinality of the set. Cell type purity is defined similarly.

We computed fate probabilities towards each terminal state next and identified driver genes by correlating gene expression with fate probabilities as outlined in the corresponding CellRank tutorial. To compare the gene ranking between the FreshMG and PsychAD cohorts, we subsetted to genes present in both datasets and computed the Pearson correlation coefficient between the gene-specific correlations $r^{(g)}_{\mathrm{FMG}}$ and $r^{(g)}_{\mathrm{PAD}}$ by CellRank:

$$r = \frac{\sum_g \left(r^{(g)}_{\mathrm{FMG}} - \bar{r}^{(g)}_{\mathrm{FMG}}\right)\left(r^{(g)}_{\mathrm{PAD}} - \bar{r}^{(g)}_{\mathrm{PAD}}\right)}{\sqrt{\sum_g \left(r^{(g)}_{\mathrm{FMG}} - \bar{r}^{(g)}_{\mathrm{FMG}}\right)^2}\sqrt{\sum_g \left(r^{(g)}_{\mathrm{FMG}} - \bar{r}^{(g)}_{\mathrm{FMG}}\right)^2}},$$

with sample mean $\bar{r}$.

Pseudotime construction

DPT (*90*) is traditionally calculated on a symmetric connectivity matrix, the constructed transition matrix T is, however, non-symmetric. To compute DPT based on our Braak-stage-informed transition matrix, we, thus, symmetrized T via $\frac{1}{2}(T + T^{\mathrm{T}})$ and row-normalized entries. Following, we computed diffusion pseudotime using SCANPY's `scanpy.tl.dpt` function with default values. The corresponding initial cells were identified via extreme points in diffusion components (*91*). To verify that the constructed pseudotime recapitulates our findings that homeostatic CECR2 cells decline with disease progression, while the number of homeostatic PICALM cells increases, we stratified pseudotime by subtype (**Fig. 5C**). Next, we performed a Welch's t-test to validate that homeostatic CECR2 cells are assigned significantly smaller pseudotime values compared to the set of homeostatic PICALM. We performed similar Welch's t-tests to assess the change between consecutive Braak stages. For each dataset, we first computed the T-statistics from Welch's t-test and then combined them across datasets using Stouffer's method: Considering T-statistics T^{freshMG} and T^{psychAD}, the reported T-statistic T given by

$$T = \frac{T^{\mathrm{freshMG}} + T^{\mathrm{psychAD}}}{2}.$$

As a final analysis, we correlated fate probabilities with gene expression for each lineage to identify putative driver genes for each lineage. Here, we included genes present in both datasets. To confirm concordance between the two independent cohorts, we computed the Spearman correlation between the two rankings.

Inferring cell-to-cell interactions

CCI analysis relies on inference of ligand-receptor interactions given a gene expression matrix with annotated cell types. By comparing to a known set of ligand-receptor (LR) pairs (reference "resource"), CCI can be inferred and scored through a variety of methods. LR pairs across cell types that are expressed above a set threshold and are differentially co-expressed, are inferred to represent interactions between the cell types. The `LIANA` (*33*) framework combines several established CCI inference methods and reference resources. We used the Python implementation of `LIANA` (v0.1.8). For each donor in FreshMG and PsychAD, we separately ran the standard rank_aggregate pipeline (resource_name = 'consensus', expr_prop = 0.1, min_cells = 5, n_perms = 1000). This utilizes the RobustRankAggregate (*92*) algorithm for aggregating scores from several methods (CellPhoneDB, Connectome, log2FC, NATMI, SingleCellSignalR, and CellChat)(*33*, *93–97*) into a single magnitude score for each CCI. We used the standard "consensus" CCI reference resource provided by `LIANA`. For a given pair of cell types and pair of genes to be considered for CCI scoring, each gene must be found in the reference resource, and be expressed in at least 10% of each involved cell type and in at least 5 cells. We evaluated CCI using the rank aggregate magnitude score for cell types annotated at the subtype level. We negative log-transformed these scores so that low magnitude CCI are

scored close to 0 and normalized the score distribution. Additional post-processing was then performed to filter out CCI that were not expressed in both FreshMG and PsychAD.

To assess the concordance between FreshMG and PsychAD CCI scores, we first computed the average CCI score for each CCI across donors within each cohort. We then grouped the average scores by each possible pair of subtypes and measured the Spearman rank correlation. We additionally computed an activity z-score for the frequency of CCI involving each subtype pair (**Fig. 4A**).

To determine whether CCI are differentially expressed in AD, we applied Dream[13] to construct a linear mixed model and account for technical and biological covariates (batch, age, sex). Linear mixed model regression was performed separately for FreshMG and PsychAD across four measures of AD progression: diagnosis (dx_AD), CERAD score, Braak stage, and dementia status. We then also used Dream to meta-analyze CCI that are significantly differentially expressed across both cohorts and to estimate the log fold change effect of each CCI for each AD progression measure (**Fig. 4B, Supplementary Fig. S7C**).

To evaluate whether significantly differentially expressed CCI are enriched in AD genome-wide association studies (GWAS), we utilize the Multi-marker Analysis of GenoMic Annotation (`MAGMA`)(*34*). The `MAGMA` gene set was constructed from significantly differentially expressed CCI LR pairs. These include CCI with at least a false discovery rate (FDR) of 0.05 significance, as determined by the Dream regression meta-analyses across each AD progression measure. We normalized the log2 fold change (log2FC) values for these CCI for each progression measure and split the CCI into AD (log2FC > 0) and CTRL (log2FC < 0) groups. Top LR pairs for AD and CTRL were then ranked by selecting the LR pairs involved in the CCI with the largest absolute normalized log2FC values. The ranked AD and CTRL LR pair gene sets were analyzed by the `MAGMA` for enrichment across several GWAS (**Fig. 4C**). We generated a network diagram to highlight the top-ranked three AD and CTRL CCI in our gene set (**Fig. 4D**).

To investigate the biological processes AD-relevant CCI are involved in, we performed a gene set enrichment analysis using the cell2cell (*98*) package and the human Gene Ontology Biological Processes 2023 reference (*99*, *100*) The AD-relevant CCI gene set was constructed in the same way as the `MAGMA` analysis gene set. We aggregated these CCI by the sender and receiver subtype to improve statistical power, and then computed normalized enrichment scores for each process based on our AD-relevant LR pair gene set. We prioritized processes that pass the 0.05 FDR significance threshold (**Fig. 4E**).

Analysis of genetic heritability of AD polygenic risk

We established a standardized pipeline for Multi-marker Analysis of GenoMic Annotation (`MAGMA`) followed by single-cell Disease-Relevance Scoring (`scDRS`). `MAGMA` incorporates the association p-values of genetic variants from the latest AD genome-wide association study (GWAS)(*8*). We applied `MAGMA` using a standard window of 35 kbp upstream and 10 kbp downstream around the gene body. We executed `scDRS` using the top 1000 gene weights, sorted by Z score. The `MAGMA` and `scDRS` pipeline was run separately on FreshMG and PsychAD single-cell cohorts using the following parameters. `MAGMA` was run using `-snp-loc g1000_eur.bim` (SNP location file corresponding to the Phase 3 1000 Genome Project) and –

-gene-loc NCBI38.gene.loc (gene location file from NCBI build 38). Both files were obtained from https://ctg.cncr.nl/software/magma.

To justify the use of the top 1000 genes for scDRS, genes were sorted by MAGMA z-score and top 200, 500, and 1000 genes were used for testing the concordance between cohorts in subsequent scDRS analysis. scDRS command scdrs.preprocess was run with the default parameters of n_mean_bin=20, n_var_bin=20w, while scdrs.score_cell was run using n_ctrl=100. Best concordance between FreshMG and PsychAD cohorts of average scDRS scores (per myeloids subtype) was achieved using top 1000 genes (Pearson's R of top n MAGMA genes; n = 200 was 0.85, n = 500 was 0.94, n = 1000 was 0.97, hence we proceeded with the analysis using top 1000 MAGMA genes).

We tested the following GWAS summary stats in scDRS/MAGMA pipeline: AD (*8*), MS (*101*), PD (*102*), MDD (*103*), ASD (*104*), BD (*105*), SCZ (*106*) and ALS (*107*). The scDRS scores were highly reproducible between the FreshMG and PsychAD cohorts, with AD having the greatest correlation (r = 0.97), followed by MS (r = 0.92), PD (r = 0.83), MDD (r = 0.79), ASD (r = 0.71) and ALS (r = 0.66). The lowest correlation was noted for BD (r = 0.60) and SCZ (r = 0.42), both of which are neuropsychiatric diseases. This emphasized a high reproducibility of myeloid cell heritability estimates in AD, MS, and PD, all of which are neurodegenerative diseases with progressive damage to neuronal cell types, and whose primary pathogenic mechanisms involve non-neuronal cells, including microglia and PVM. Neuropsychiatric diseases such as SCZ and BD, whose primary risks are enriched in synaptic dysfunctions of neurons, had lower correlations (**Supplementary Fig. S3C**). Per cluster association z-scores (scDRS assoc_mcz) were obtained using scdrs.method.downstream_group_analysis function. Stouffer's method for meta-analysis was used to combine FreshMG and PsychAD scDRS association z-scores using the number of cells per cell cluster as cluster weights. For each cohort, scDRS permutation p-values per cluster were combined using Stouffer's method on p-values with weights (cell counts of clusters). Meta p-values were further corrected for multiple testing using FDR correction (both per cell type and using all cell types combined). A more stringent correction was achieved using the per-cell type method hence we applied this correction.

Case-control residual analysis of heritability estimates

To test for concordance in heritability estimates, we separated cases and controls and repeated MAGMA/scDRS pipe for both FreshMG and PsychAD single-cell cohorts. We calculated meta z-scores for cases and controls separately using Stouffer's method with weights (cluster's cell counts). We correlated meta-z-scores of cases and controls using linear regression and derived residuals as a deviation from the regression line, indicative of per-cell cluster heritability. For both cohorts, per-cell pseudotime scores were correlated with per-cell scDRS scores for every microglia subtype and the correlation coefficient was calculated using Spearman's test. FreshMG and PsychAD coefficients were combined in a meta value by applying Stouffer's method and the number of cells per cell cluster as cluster weights.

1288 **Processing of genotypes**

1289 The FreshMG cohort genotype data consisted of samples from the Mount Sinai and Rush
1290 brain banks, as has been previously described(*9*). The PsychAD cohort genotype data
1291 consisted of samples from the Mount Sinai brain bank. For both cohorts, DNA extraction and
1292 genotyping were performed as described previously(*9*). In brief, genomic DNA was extracted
1293 from buffy coat or frozen brain tissue using the QIAamp DNA Mini Kit (Qiagen), according to
1294 the manufacturer's instructions. Samples were genotyped using the Infinium Psych Chip Array
1295 (Illumina) at the Mount Sinai Sequencing Core. Pre-imputation processing consisted of running
1296 the quality control script HRC-1000G-check-bim.pl from the McCarthy Lab Group
1297 (https://www.well.ox.ac.uk/~wrayner/tools/), using the Trans-Omics for Precision Medicine
1298 (TOPMed) reference(*108*). Genotypes were then phased and imputed on the TOPMed
1299 Imputation Server (https://imputation.biodatacatalyst.nhlbi.nih.gov). Samples with a mismatch
1300 between one's self-reported and genetically inferred sex, suspected sex chromosome
1301 aneuploidies, high relatedness as defined by the KING kinship coefficient (*109*) (KING > 0.177),
1302 and outlier heterozygosity (+/- 3SD from mean) were removed. Additionally, samples with a
1303 sample-level missingness > 0.05 were removed and calculated within a subset of high-quality
1304 variants (variant-level missingness ≤ 0.02).

1305 Samples of European (EUR) ancestry, as defined by assignment to the EUR
1306 superpopulation described by the 1000 Genomes Project (*110*, *111*), were isolated using a 3SD
1307 ellipsoid method. Genotypes were first merged with GRCh38 v2a 1000 Genomes Project data
1308 (https://wellcomeopenresearch.org/articles/4-50)(*111*) using BCFtools version 1.9 (*112*). PLINK
1309 2.0 (*113*) was then used to calculate the merged genotypes' principal components (PCs),
1310 following filtering (minor allele frequency (MAF) ≥ 0.01, Hardy-Weinberg equilibrium (HWE) p-
1311 value≥1×10^{-10}, variant-level missingness ≤ 0.01, regions with high linkage disequilibrium (LD)
1312 removed) and LD pruning (window size = 1000 kb, step size = 10, r2 = 0.2) steps. An ellipsoid
1313 with a radius of 3SD, corresponding to the 1000 Genomes Project EUR superpopulation, was
1314 constructed using the first three genotype PCs. Only samples that fell within this ellipsoid
1315 (FreshMG: n = 178, PsychAD: n = 759) were retained for subsequent variant-level filtering.
1316 Autosomal bi-allelic variants with an imputation R^2 > 0.8, HWE p-value≥1×10^{-6}, and variant-
1317 level missingness ≤ 0.02 were retained. Genotypes were then annotated with ancestry-specific
1318 MAF values from the National Center for Biotechnology Information's Allele Frequency
1319 Aggregator (ALFA) (https://ftp.ncbi.nih.gov/snp/population_frequency/latest_release/). Only
1320 variants with an ancestry-specific ALFA MAF ≥ 0.01 (FreshMG: n = 10,828,658, PsychAD: n =
1321 18,490,352) were retained.

1322

1323 **PRS calculation**

1324 Polygenic risk scores (PRS) were calculated on the FreshMG and PsychAD cohort samples
1325 using AD GWAS summary statistics (*8*). The PRS-CS-auto method (*114*) was used to apply
1326 continuous shrinkage priors to the effect sizes from these summary statistics. A EUR LD
1327 reference panel provided by the developers of PRS-CS was utilized
1328 (https://github.com/getian107/PRScs), which draws from 1000 Genomes Project data (*111*).
1329 The following PRS-CS default settings were used: parameter a in the γ-γ prior = 1, parameter b

in the γ-γ prior = 0.5, MCMC iterations = 1000, number of burn-in iterations = 500, and thinning of the Markov chain factor = 5. The global shrinkage parameter phi was set using a fully Bayesian determination method. Individual-level PRS were calculated using PLINK 2.0 (*113*).

Transcriptional variation with PRS

PRS analysis was performed using the `dreamlet` package (v0.99) that applies a linear mixed model with precision weights to fit a regression model. Instead of applying a fixed contrast between two coefficients, we used AD polygenic risk scores (PRS) as a continuous variable to test for the presence of non-linear effects on variance. We subtracted admixed donors from this analysis using the PCA analysis of the first 5 genotype PCs (2 individuals were removed from PsychAD and 1 from the FreshMG cohort as clear outliers in the PCA plots). In addition, we removed a cluster of 200 individuals that were clustering separately on the PC1/PC2 plot in psychAD as admixed individuals with a percentage of a non-EUR ancestry ranging from 2.5%-10% (mainly AFR ancestry). Similarly, we removed 6 more donors from FreshMG that were outliers and showed decreased EUR and increased AFR ancestry. The removal of admixed individuals allowed us to achieve a high level of concordance in `Dreamlet` PRS analysis between FreshMG and PsychAD cohorts. For the PsychAD cohort, we considered the following covariates to model the variance: source, log(n_counts), PMI, age, AD_Bellenguez PRS, sex, dx, genotype PCs 1-5. For the FreshMG cohort, we used the same set of covariates, in addition to the sequencing batch as a covariate. We further performed a fixed-effect meta-analysis with the R metafor package using effect sizes and standard error from the `dreamlet` output (metafor `rma` function with parameters: `yi = logFC, sei = logFC / t, method = "FE"`). Meta p-values were further corrected for multiple testing using FDR correction (using the per-cell type correction).

To test whether the observed cell proportions change with PRS as a continuous variable, we applied the `crumblr` R package to each cohort and performed analysis of count ratio data with precision-weighted linear mixed models. Similar to the `Dreamlet` analysis, we modeled PRS as a continuous variable and tested for non-linear effects. FreshMG and PsychAD effect sizes were combined in a meta value using Stouffer's method and the number of cells per cell cluster as cluster weights.

Supplementary Information

Assessment of *ex-vivo* activation in Microglia

Microglia are highly reactive cells and prolonged exposure to non-physiological conditions could induce unintended responses (*115*, *116*). It has previously been shown that enzymatic dissociation of brain tissue performed at elevated temperatures can stimulate microglial cells, termed *ex-vivo* activated microglia (exAM)(*17*, *79*, *117*). Failing to account for dissociation-induced changes can compromise the interpretation of microglial biology (*118*). Although artificially induced, we wondered if the proportion of exAM might reflect microglial reactivity to pathological lesions and, as such, could provide valuable insights into disease mechanisms. In this study, we are uniquely positioned to interrogate the impact of exAM as myeloids from the FreshMG cohort were isolated via enzymatic dissociation at 37°C while samples from the PsychAD cohort, consisting of flash frozen tissue, were processed using an ice-cold, enzyme free, dissociation buffer. Assessing the extent and prevalence of the exAM signature in our datasets, we observed a distinct subtype in the FreshMG dataset, called MG_exAM_ERN1, which accounts for about 14.8% of all myeloid cells, and shows up-regulation of genes implicated in cell-cell adhesion, including ERN1, PLK2 (serine/threonine-protein kinase), CSKMT, and SNHG5. Notably, PLK2 is an enzyme regulating synaptic activity and has been implicated in stimulating Aβ production (*119*, *120*). We note that the PsychAD dataset had very few cells identified as the ERN1 subtype, which belongs to the exAM subclass. This result suggests a number of possibilities. Given that the transcripts in the PsychAD dataset originate from the nuclear fraction of frozen nuclei and are free from enzymatic treatment or dissociation bias, it's possible that the exAM cluster is predominantly derived from fresh tissue and is artificially induced during processing (*17*). In addition, the transcripts that define the ERN1 subtype may be predominantly cytoplasmic and are, thus, missing from the PsychAD samples. Moreover, we acknowledge that we observe a substantial compositional variation among three different cohorts. However, to properly assess the extent of compositional variation, we need to model this by accounting for various technical effects, including the dissection bias. In conclusion, this comparative analysis confirmed the robustness of the human microglial taxonomy, independent of tissue source, agonal state, and postmortem interval (PMI).

Disease trajectory of human myeloid cells

Understanding the dynamic changes that take place during the onset and progression of AD at a molecular-level requires modeling of gene expression change along the measures of disease progression and identifying corresponding putative drivers. Analyses solely based on donor-level clinical covariate, such as CERAD scores or Braak staging, are limited due to the discrete nature of these variables. However, we reasoned that each labeled disease stage contains observations spanning the range of disease development and sought to identify drivers and order cells along a disease pseudotime trajectory.

Trajectory inference allows us to expand our ability to describe molecular changes at single-cell resolution. Trajectory inference methods have been remarkably successful in describing normal developmental processes faithfully and identifying regulatory mechanisms

based on single-cell sequencing data (*90*, *121*, *122*). Classical pseudotime algorithms order cells along a developmental axis, with early and late cells being assigned low and high pseudotime values, respectively. To take advantage of advances in experimental design and different sources of information, alternative methods have been developed. To link observations across experimental time points, optimal transport-based solutions have been proposed to assign each measurement from one experimental time point its likely future state in the following via a probabilistic assignment in the form of transport maps (*29*, *123*). These couplings can then be used to quantify cellular change and determine the fate and putative drivers using CellRank 2's *RealTimeKernel (30)*. Using it together with and GPCCA estimator (*30*, *89*), we automatically inferred the terminal states of the disease dynamics. As AD onset and progression do not result in the emergence or disappearance of novel cell types, we expected to recover the major subclasses of the data, *i.e.*, adaptive, homeostatic, ADAM, or PVM. In concordance with this ground truth, we recovered the terminal states accordingly and observed a high terminal state purity defined by the fraction of cells with the correct cell type and Braak stage six (terminal state purity was 1.0 for all subclasses used). Following, we computed driver genes of these respective fates by correlating gene expression with fate probabilities (**Methods**). We replicated the same analysis using the PsychAD and observed high concordance between the correlations between gene expression and fate probabilities associated with each gene (**Supplementary Fig. S5I**). While CellRank 2 identifies putative lineage drivers, it does not align cells along the disease trajectory. To construct this orthogonal information, we used the transition matrix computed by the *RealTimeKernel* to compute a Braak-stage-informed pseudotime for the two subsets of the data in a similar fashion as previously proposed for experimental time points by the CellRank 2 study (*30*) (**Methods**). We tested if the gene expression changes over pseudotime inferred on the FreshMG cohort agrees with the corresponding change in the PsychAD dataset. As expected, the inferred change in gene expression showed high concordance between the two independent cohorts for both homeostatic and adaptive lineages (**Supplementary Figs. S5J-K**).

Data availability

The single-cell dataset, clinical metadata, and analysis outputs are available via the AD Knowledge Portal (https://adknowledgeportal.org). The AD Knowledge Portal is a platform for accessing data, analyses, and tools generated by the Accelerating Medicines Partnership (AMP-AD) Target Discovery Program and other National Institute on Aging (NIA)-supported programs to enable open-science practices and accelerate translational learning. The data, analyses, and tools are shared early in the research cycle without a publication embargo on secondary use. Data is available for general research use according to the following requirements for data access and data attribution (https://adknowledgeportal.org/DataAccess/Instructions). For access to data described in this manuscript see: https://www.synapse.org/#!Synapse:syn52795287.

Code availability

All the source codes used in this study are available via GitHub: https://github.com/DiseaseNeuroGenomics/scMyeloidAD

Acknowledgments

We would like to express our deep gratitude to the patients and their families who generously donated the invaluable biological material essential for the success of this study. We are profoundly indebted to their participation and commitment to advancing scientific knowledge and improving human health. We acknowledge the National Institute on Aging for their generous support in funding this research with the following NIH grants: R01AG065582 (PR, VH), R01AG067025 (PR, VH), and R01AG082185 (PR, VH, DL). ROSMAP is supported by P30AG10161, P30AG72975, R01AG15819, R01AG17917. U01AG46152, U01AG61356. ROSMAP resources can be requested at https://www.radc.rush.edu. We also thank Stefano Marenco and Pavan Auluck from the Human Brain Collection Core (HBCC) at the National Institute of Mental Health-Intramural Research Program for their contribution to the resource. The HBCC is supported by the NIMH-IRP under project ZIC MH002903.

Author contributions

Conceptualization: DL, VH, JFF, PR.
Methodology: DL, GEH, JFF, PR.
Investigation: JV, XW, KP, PM, EH, JMF, SPK, ZS, SA, MA, CC, AH, JFF.
Formal analysis: DL, CP, CS, MP, SK, PW, RK, JB, PNM, SZ, KT, DM.
Validation: JV, XW, JMF, JFF.
Resources: KGB, RS, CPK, DAB, VH.
Writing: DL, JFF, PR, with contributions from all authors.
Visualization: DL, JV.

Supervision: DL, GCY, GV, FJT, GEH, VH, JFF, PR.
Project administration: DL, PR.
Funding acquisition: DL, VH, PR.
All authors read and approved the final draft of the paper.

Competing interests

FJT consults for Immunai Inc., Singularity Bio B.V., CytoReason Ltd, Omniscope Ltd, Cellarity, and has ownership interests in Dermagnostix GmbH and Cellarity. The remaining authors declare no competing interests.

Materials & Correspondence

Correspondence to Donghoon Lee and Panos Roussos.

Supplementary Figures

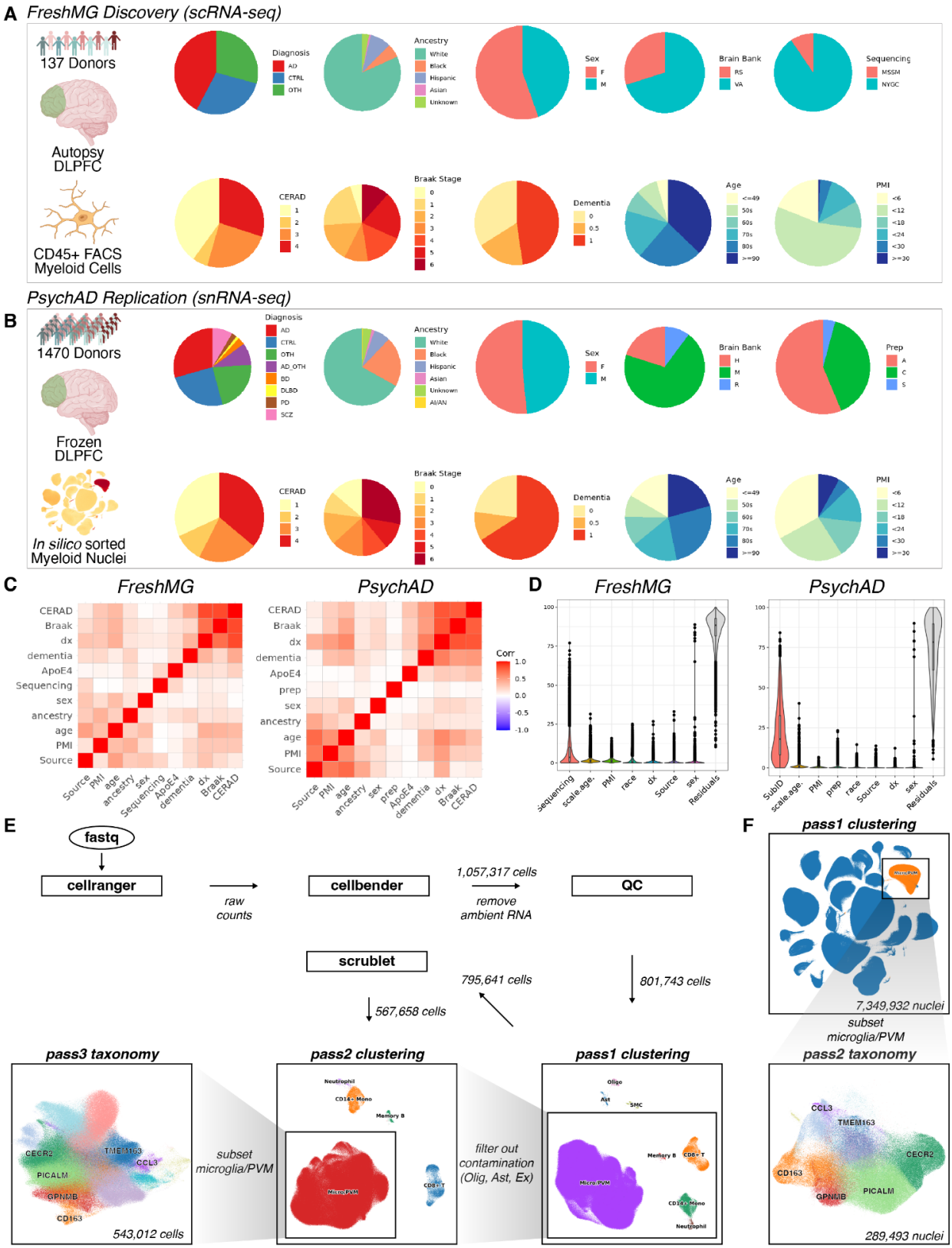
A
FreshMG Discovery (scRNA-seq)
137 Donors
Autopsy DLPFC
CD45+ FACS Myeloid Cells
Diagnosis
AD
CTRL
OTH
Ancestry
White
Black
Hispanic
Asian
Unknown
Sex
F
M
Brain Bank
RS
VA
Sequencing
MSSM
NYGC
CERAD
Braak Stage
Dementia
Age
PMI
B
PsychAD Replication (snRNA-seq)
1470 Donors
Frozen DLPFC
In silico sorted Myeloid Nuclei
AD_OTH
BD
DLBD
PD
SCZ
AI/AN
Prep
C
FreshMG
PsychAD
CERAD
Braak
dx
dementia
ApoE4
Sequencing
sex
ancestry
age
PMI
Source
prep
Corr
D
FreshMG
PsychAD
SubID
scale.age
race
Residuals
E
fastq
cellranger
raw counts
cellbender
1,057,317 cells
remove ambient RNA
QC
scrublet
795,641 cells
801,743 cells
567,658 cells
F
pass1 clustering
7,349,932 nuclei
subset microglia/PVM
pass2 taxonomy
289,493 nuclei
pass3 taxonomy
543,012 cells
subset microglia/PVM
pass2 clustering
filter out contamination (Olig, Ast, Ex)
pass1 clustering
Neutrophil
CD14+ Mono
Memory B
CD8+ T
Micro/PVM
Oligo
Ast
SMC
CCL3
TMEM163
CECR2
CD163
PICALM
GPNMB

Supplementary Figure S1. **(A)** Demographic and clinical metadata of the FreshMG cohort. **(B)** Demographic and clinical metadata of the PsychAD cohort. **(C)** Pairwise correlation of donor-level clinical variables. **(D)** Partition of gene expression variance using technical and donor-level covariates used in the study. **(E)** Schematic overview of the FreshMG single-cell data processing. **(F)** Schematic overview of the PsychAD single-cell data processing.

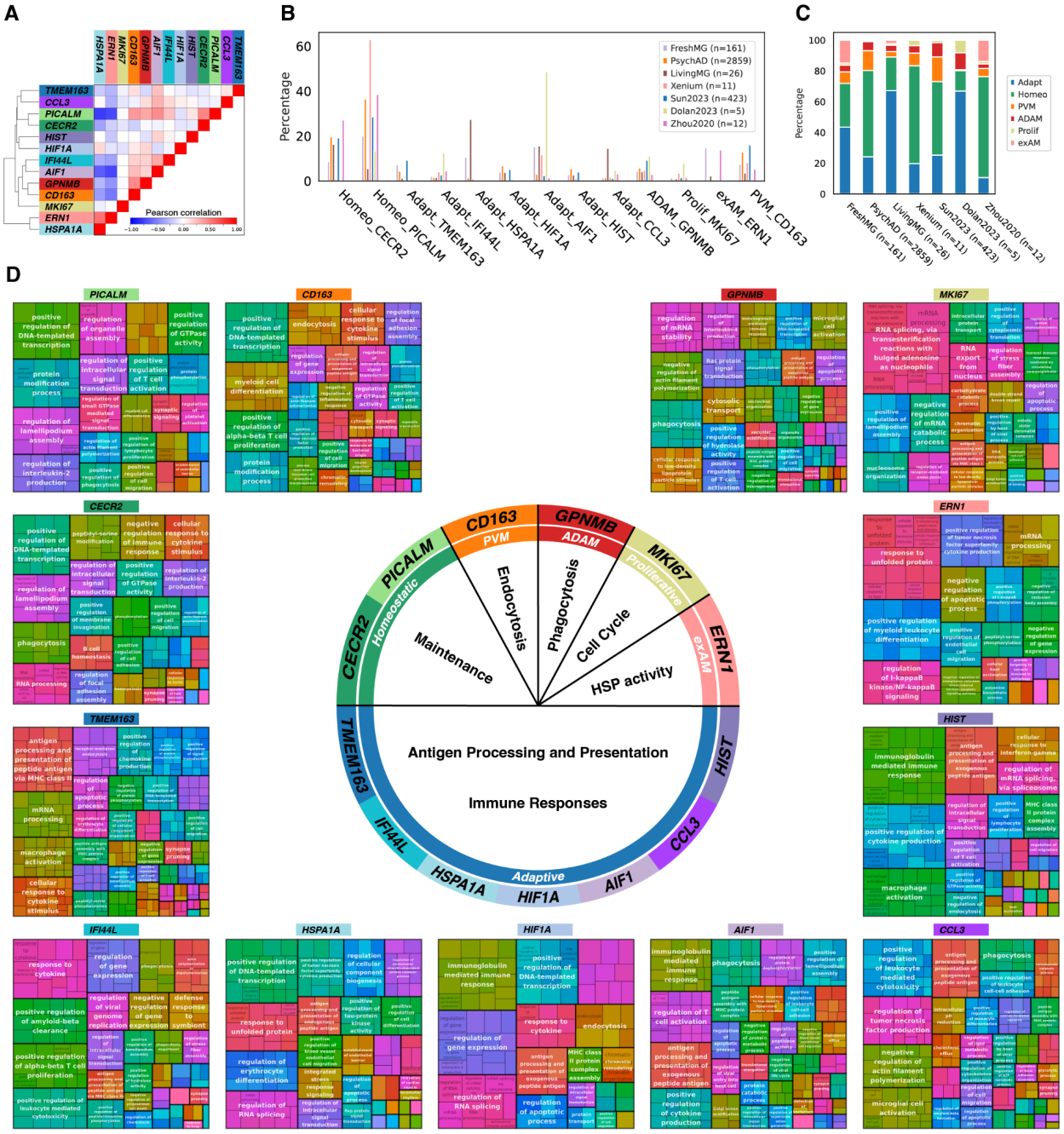

Supplementary Figure S2. **(A)** Pairwise Pearson correlation between FreshMG and PsychAD myeloid subtypes. **(B)** Compositional differences of myeloid subtypes across independent (*LivingMG* sourced from biopsy specimens and represents living brains) and published datasets; Sun2023 (*14*), Dolan2023 (*23*), and Zhou2020 (*27*). **(C)** Compositional differences of myeloid subclasses. **(D)** Pathway enrichment analysis of human myeloid subtypes using GO biological process database. Subtype-specific genes were prioritized using Mann–Whitney U tests of one-vs-the-rest subsets.

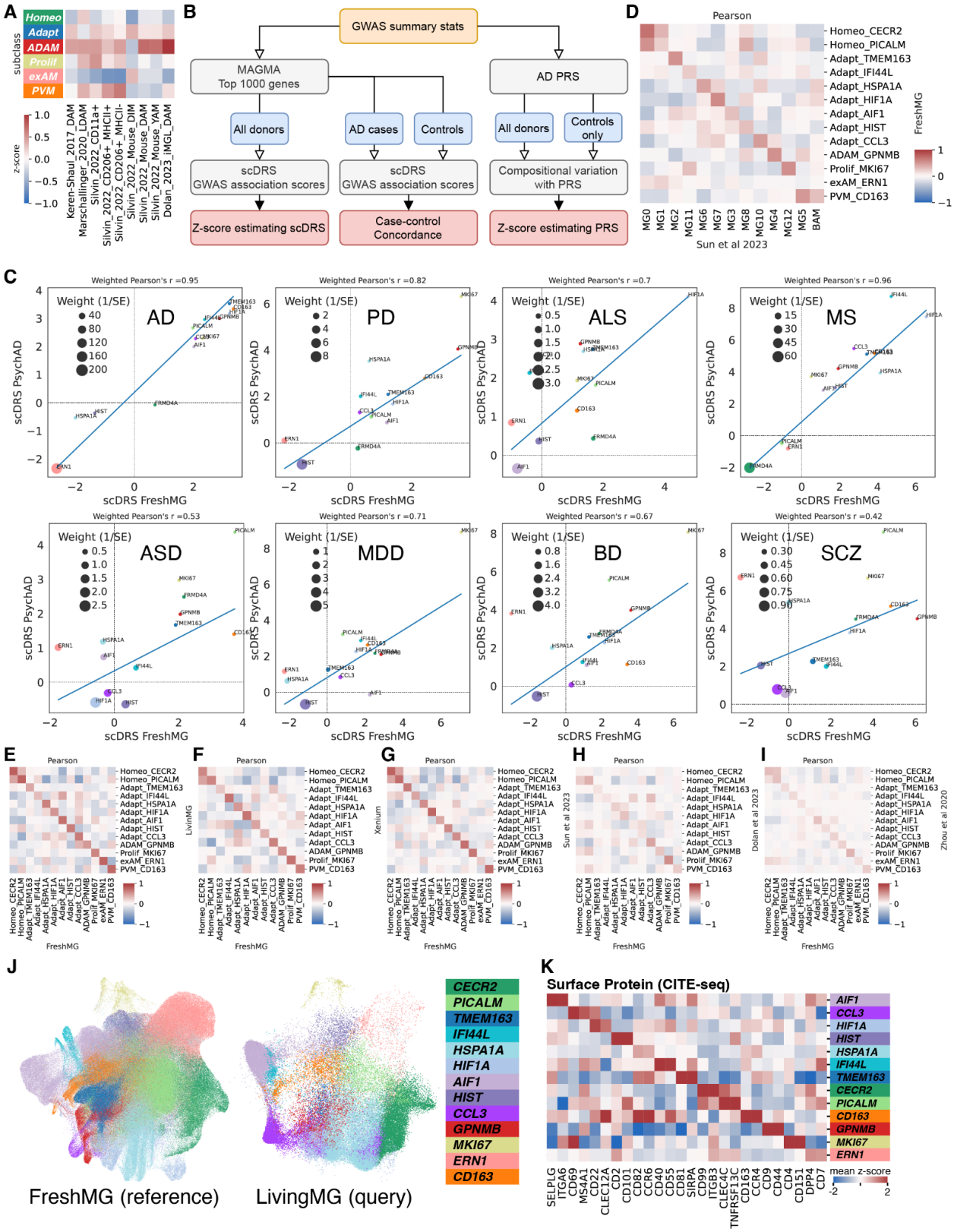

Supplementary Figure S3. (A) Enrichment of gene signatures from published studies. DAM: disease-associated microglia, LDAM: lipid-droplet accumulating microglia, DIM: disease

inflammatory macrophages, YAM: youth-associated microglia, iMGL: human stem-cell-differentiated microglia.
(B) Schematic overview of the `scDRS` and PRS methods for evaluating heritability of AD risk. **(C)** Correlation of the scDRS scores between the FreshMG and PsychAD cohorts across human brain disorders. **(D)** Comparison of myeloid subtypes to microglial states defined in Sun *et al*. 2023 dataset. **(E)** Pairwise Pearson correlation between FreshMG and LivingMG myeloid subtypes. **(F)** Pairwise Pearson correlation between FreshMG and Xenium myeloid subtypes. **(G)** Pairwise Pearson correlation between FreshMG and Sun *et al*. 2023 myeloid subtypes. **(H)** Pairwise Pearson correlation between FreshMG and Dolan *et al*. 2023 myeloid subtypes. **(I)** Pairwise Pearson correlation between FreshMG and Zhou *et al*. 2020 myeloid subtypes. **(J)** Annotation of the LivingMG (biopsies) dataset using the FreshMG as the reference annotation. **(K)** Subtype-specific surface protein markers from the CITE-seq antibody derived tags (ADT).

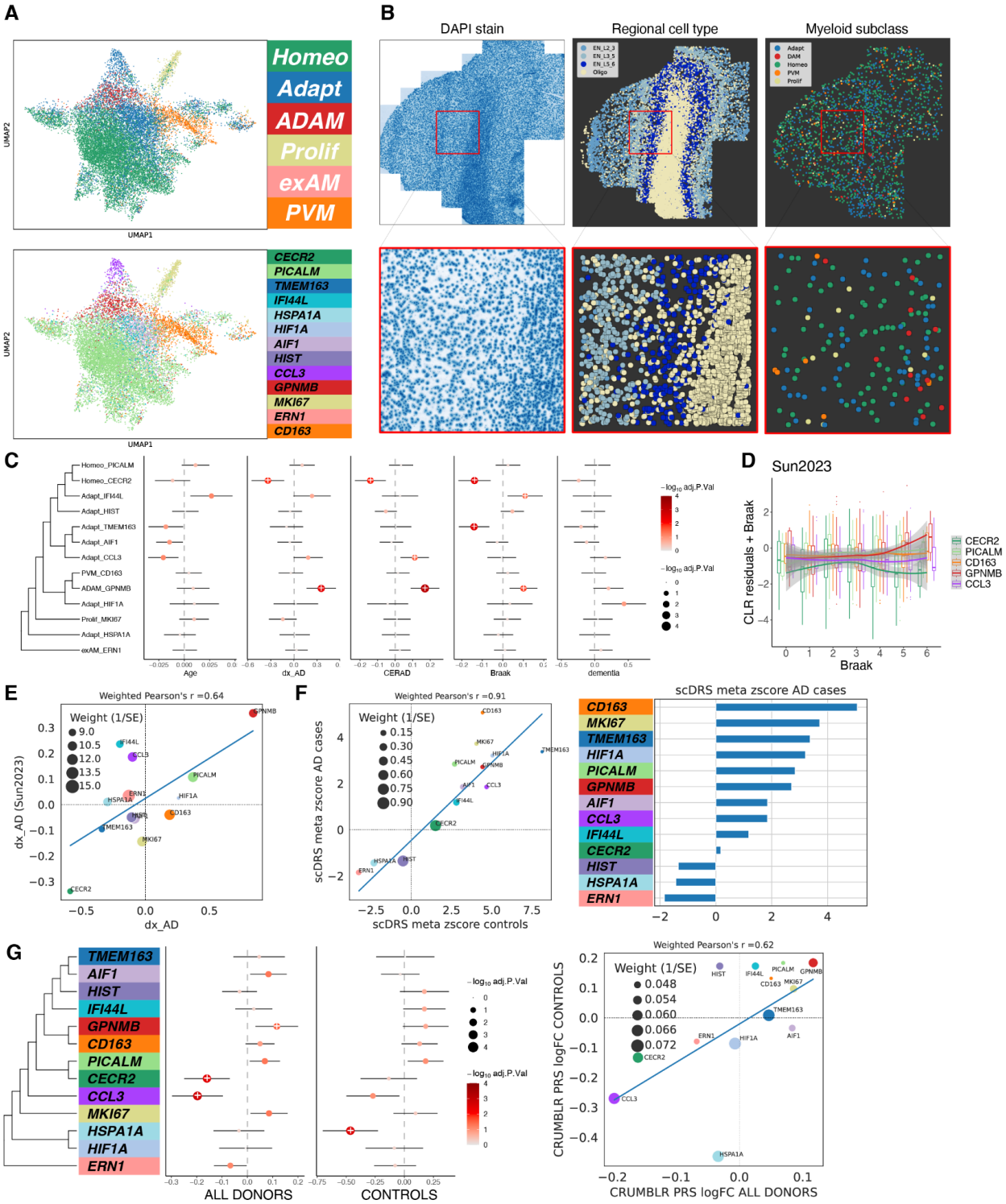

Supplementary Figure S4. **(A)** UMAP of myeloid subclasses and subtypes from the Xenium *in situ* spatial transcriptomics dataset. **(B)** Representative slide of Xenium *in situ* spatial transcriptomics data with zoomed in region of interest. Left: DAPI stain, Middle: laminar distribution of neuronal cell types, Right: distribution of myeloid cells annotated by subclasses. **(C)** Compositional variation of aging and AD phenotypes using Sun *et al*. 2023 dataset. **(D)**

Covariate adjusted compositional variation with Braak staging using Sun *et al*. 2023 dataset. **(E)** Comparison of compositional variation of dx_AD between this study and Sun *et al*. 2023. **(F)** Correlation of `scDRS` z-scores between AD cases and controls. **(G)** Compositional variation of PRS, side-by-side comparison between one using all donors and another using control donors only. Weighted Pearson's correlation using inverse of average of standard error as weights.

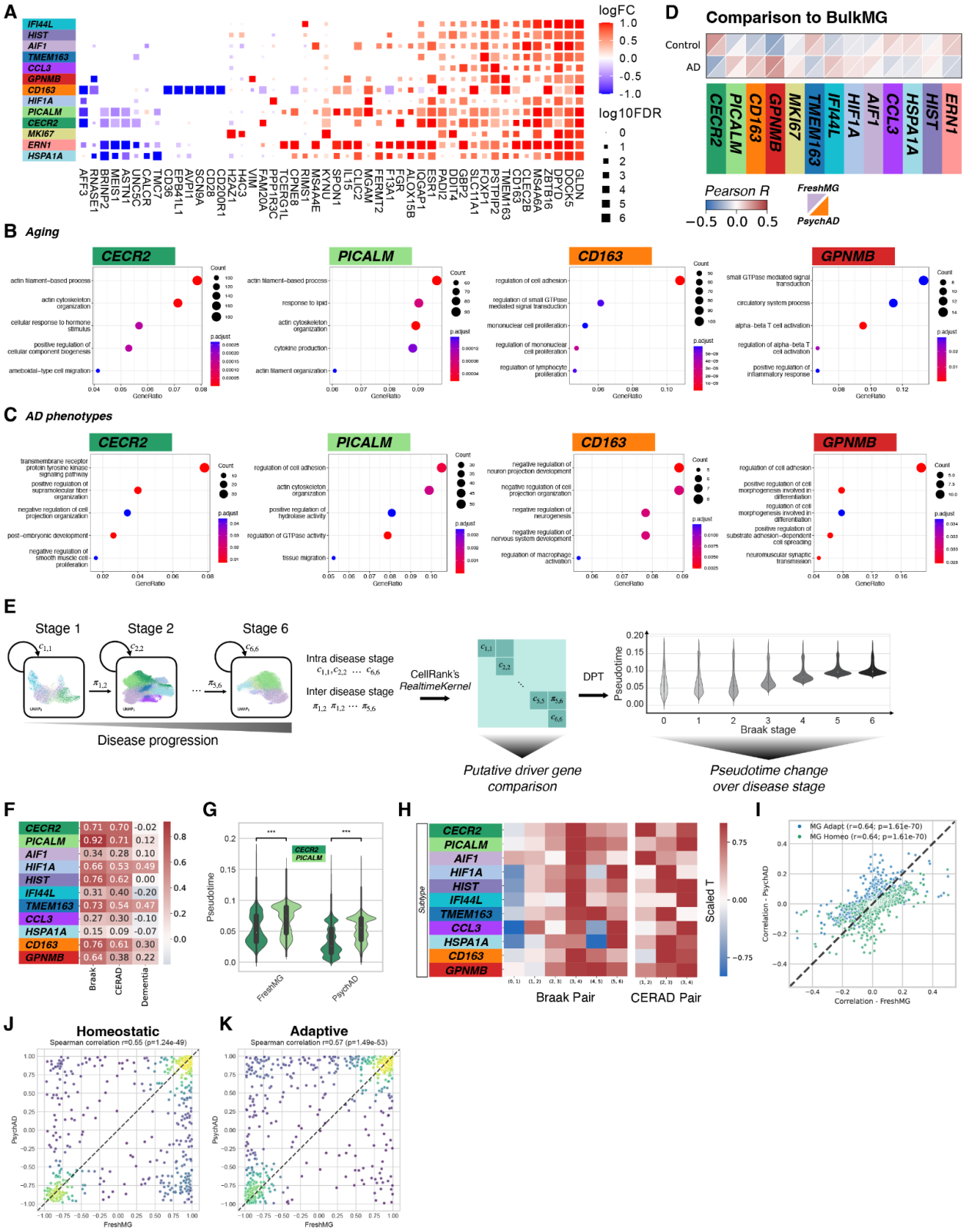

Supplementary Figure S5. (A) Differentially expressed genes by myeloid subtypes associated with disease-free aging. **(B)** Pathway enrichment analysis using the GO biological process database for disease-free aging. **(C)** Pathway enrichment analysis using the GO biological

process database for AD phenotypes. **(D)** Comparison of myeloid subtypes to homogenate bulk RNA-seq expression stratified by AD diagnosis. **(E)** Schematic overview of the pseudotime inference based on Braak staging. State transition matrix inferred using the optimal transport algorithm (Moscot). **(F)** Spearman correlations between inferred disease pseudotime and different measures of AD phenotypes. **(G)** Distribution of disease pseudotime between two homeostatic subtypes. **(H)** Magnitude of changes in disease pseudotime between two adjacent disease stages measured by Braak and CERAD. **(I)** Concordance of the putative drivers of two fates (adaptive and homeostatic) between FreshMG and PsychAD cohorts. Putative drivers are defined by correlating gene expression with fate probabilities. **(J)** Correlation between gene expression change and inferred disease pseudotime showing the concordance of the correlation between FreshMG and PsychAD cohorts for homeostatic and **(K)** adaptive lineages.

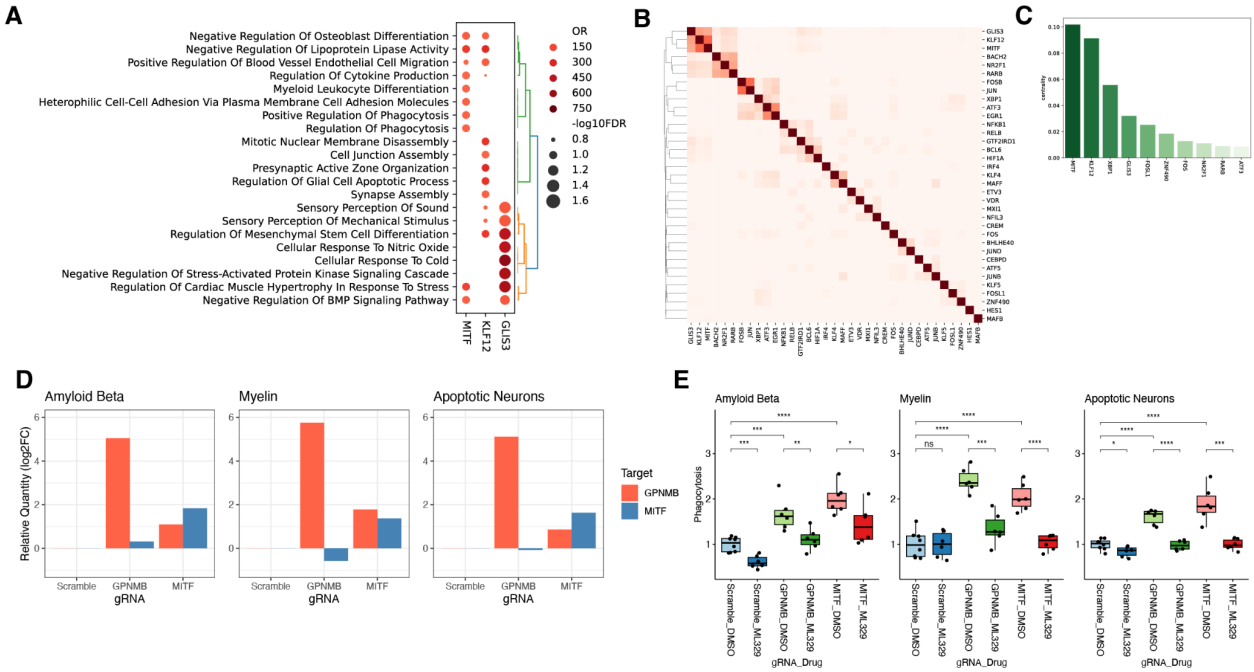

Supplementary Figure S6. **(A)** Pathway enrichment analysis of *KLF12*, *MITF*, and *GLIS3* regulons using GO biological process database. **(B)** Jaccard Index of SCENIC regulon target genes. **(C)** PageRank centrality scores of the GRN nodes. **(D)** RT-qPCR of *GPNMB* and *MITF* after CRISPR activation in HMC3 cell line. **(E)** Relative level of phagocytosis after CRISPR activation in HMC3 cell line with or without the *MITF* pathway inhibitor ML329.

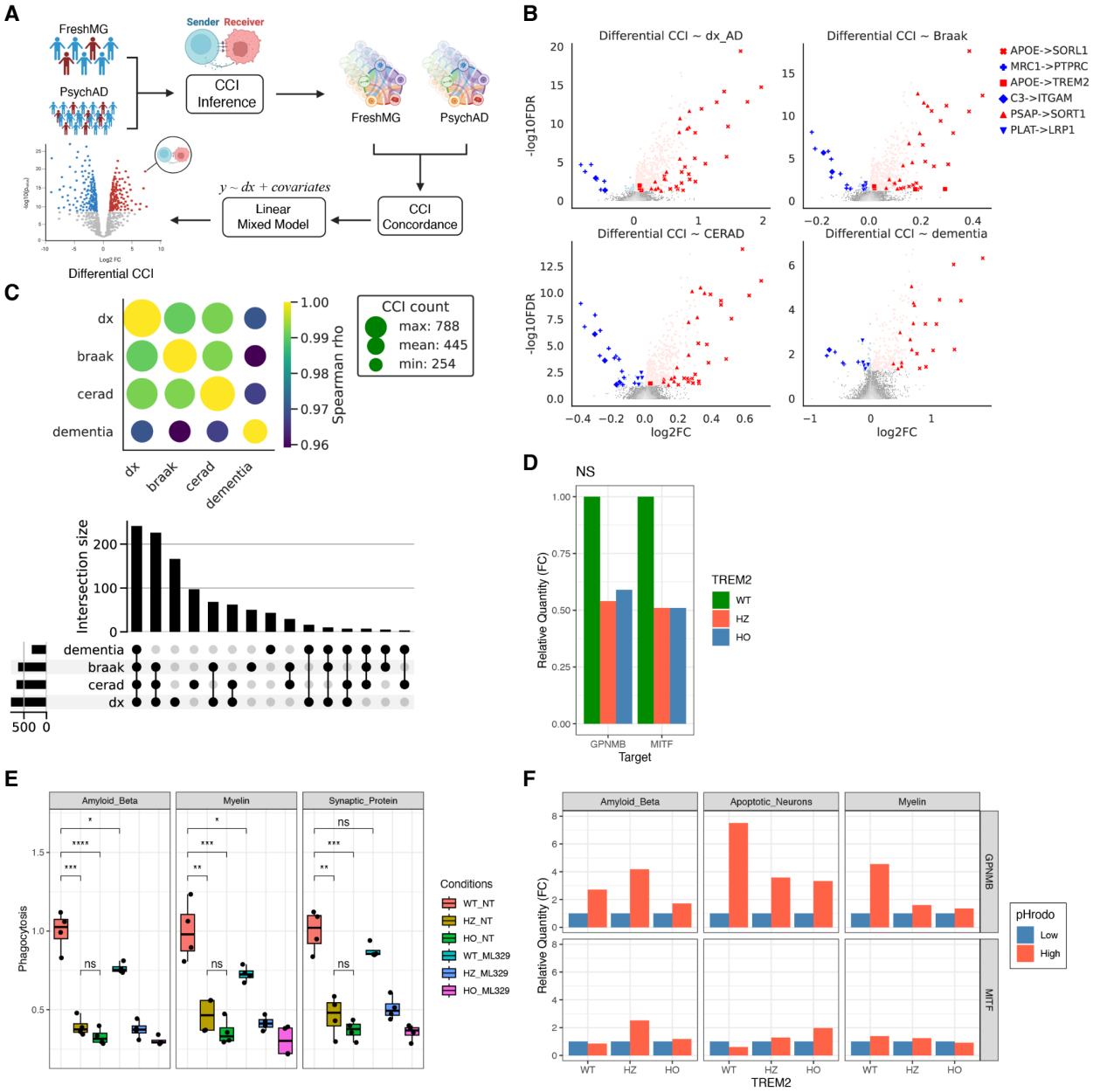

Supplementary Figure S7. **(A)** Schematic overview of the methods for inferring disease-associated CCI. **(B)** Differential CCI using 4 different measures of AD phenotypes; AD cases vs controls (dx_AD), CERAD, Braak, and dementia. **(C)** Concordance of differential CCIs among different measures of AD phenotypes. **(D)** Relative mRNA expression of *GPNMB* and *MITF* measured by RT-qPCR for *TREM2* knockouts. **(E)** Relative level of phagocytosis among WT, TREM2 heterozygous, and homozygous knockouts in iPSC-derived microglia using Aβ, myelin, and synaptic protein as substrates. **(F)** Relative mRNA expression of *GPNMB* and *MITF* measured by RT-qPCR for high and low phagocytosing microglia using Aβ, myelin, and synaptic protein as substrates.

Supplementary Tables

Supplementary Table S1. Myeloid taxonomy of the FreshMG dataset with de-identified individual ID.

Supplementary Table S2. Myeloid taxonomy of the PsychAD dataset with de-identified individual ID.

Supplementary Table S3. Clinical metadata of the FreshMG dataset with de-identified individual ID and age ranges.

Supplementary Table S4. Clinical metadata of the PsychAD dataset with de-identified individual ID and age ranges.

Supplementary Table S5. List of Akoya antibodies.

Supplementary Table S6. Compositional variation meta-analysis for Aging.

Supplementary Table S7. Compositional variation meta-analysis for AD phenotypes.

Supplementary Table S8. Differential gene expression meta-analysis for Aging.

Supplementary Table S9. Differential gene expression meta-analysis for AD phenotypes.

Supplementary Table S10. Pseudotime estimates for the FreshMG dataset.

Supplementary Table S11. Pseudotime estimates for the PsychAD dataset.

Supplementary Table S12. GRN adjacencies.

Supplementary Table S13. Regulon enrichment analysis for AD signatures.

Supplementary Table S14. Differential CCI meta-analysis.

Supplementary Table S15. scDRS scores from meta-analysis.

Supplementary Table S16. List of probes for the Xenium custom panel

Supplementary Table S17. qPCR Primers for targeted proteins

Reference

1. J. M. Long, D. M. Holtzman, Alzheimer Disease: An Update on Pathobiology and Treatment Strategies. *Cell* **179**, 312–339 (2019).

2. S. Hickman, S. Izzy, P. Sen, L. Morsett, J. El Khoury, Microglia in neurodegeneration. *Nat. Neurosci.* **21**, 1359–1369 (2018).

3. F. Leng, P. Edison, Neuroinflammation and microglial activation in Alzheimer disease: where do we go from here? *Nat. Rev. Neurol.* **17**, 157–172 (2021).

4. S. De Schepper, J. Z. Ge, G. Crowley, L. S. S. Ferreira, D. Garceau, C. E. Toomey, D. Sokolova, J. Rueda-Carrasco, S.-H. Shin, J.-S. Kim, T. Childs, T. Lashley, J. J. Burden, M. Sasner, C. Sala Frigerio, S. Jung, S. Hong, Perivascular cells induce microglial phagocytic states and synaptic engulfment via SPP1 in mouse models of Alzheimer's disease. *Nat. Neurosci.* **26**, 406–415 (2023).

5. H. Keren-Shaul, A. Spinrad, A. Weiner, O. Matcovitch-Natan, R. Dvir-Szternfeld, T. K. Ulland, E. David, K. Baruch, D. Lara-Astaiso, B. Toth, S. Itzkovitz, M. Colonna, M. Schwartz, I. Amit, A Unique Microglia Type Associated with Restricting Development of Alzheimer's Disease. *Cell* **169**, 1276–1290.e17 (2017).

6. T. Jonsson, H. Stefansson, S. Steinberg, I. Jonsdottir, P. V. Jonsson, J. Snaedal, S. Bjornsson, J. Huttenlocher, A. I. Levey, J. J. Lah, D. Rujescu, H. Hampel, I. Giegling, O. A. Andreassen, K. Engedal, I. Ulstein, S. Djurovic, C. Ibrahim-Verbaas, A. Hofman, M. A. Ikram, C. M. van Duijn, U. Thorsteinsdottir, A. Kong, K. Stefansson, Variant of TREM2 associated with the risk of Alzheimer's disease. *N. Engl. J. Med.* **368**, 107–116 (2013).

7. R. Guerreiro, A. Wojtas, J. Bras, M. Carrasquillo, E. Rogaeva, E. Majounie, C. Cruchaga, C. Sassi, J. S. K. Kauwe, S. Younkin, L. Hazrati, J. Collinge, J. Pocock, T. Lashley, J. Williams, J.-C. Lambert, P. Amouyel, A. Goate, R. Rademakers, K. Morgan, J. Powell, P. St George-Hyslop, A. Singleton, J. Hardy, Alzheimer Genetic Analysis Group, TREM2 variants in Alzheimer's disease. *N. Engl. J. Med.* **368**, 117–127 (2013).

8. C. Bellenguez, F. Küçükali, I. E. Jansen, L. Kleineidam, S. Moreno-Grau, N. Amin, A. C. Naj, R. Campos-Martin, B. Grenier-Boley, V. Andrade, P. A. Holmans, A. Boland, V. Damotte, S. J. van der Lee, M. R. Costa, T. Kuulasmaa, Q. Yang, I. de Rojas, J. C. Bis, A. Yaqub, I. Prokic, J. Chapuis, S. Ahmad, V. Giedraitis, D. Aarsland, P. Garcia-Gonzalez, C. Abdelnour, E. Alarcón-Martín, D. Alcolea, M. Alegret, I. Alvarez, V. Álvarez, N. J. Armstrong, A. Tsolaki, C. Antúnez, I. Appollonio, M. Arcaro, S. Archetti, A. A. Pastor, B. Arosio, L. Athanasiu, H. Bailly, N. Banaj, M. Baquero, S. Barral, A. Beiser, A. B. Pastor, J. E. Below, P. Benchek, L. Benussi, C. Berr, C. Besse, V. Bessi, G. Binetti, A. Bizarro, R. Blesa, M. Boada, E. Boerwinkle, B. Borroni, S. Boschi, P. Bossù, G. Bråthen, J. Bressler, C. Bresner, H. Brodaty, K. J. Brookes, L. I. Brusco, D. Buiza-Rueda, K. Bûrger, V. Burholt, W. S. Bush, M. Calero, L. B. Cantwell, G. Chene, J. Chung, M. L. Cuccaro, Á. Carracedo, R. Cecchetti, L. Cervera-Carles, C. Charbonnier, H.-H. Chen, C. Chillotti, S. Ciccone, J. A. H. R. Claassen, C. Clark, E. Conti, A. Corma-Gómez, E. Costantini, C. Custodero, D. Daian, M. C. Dalmasso, A. Daniele, E. Dardiotis, J.-F. Dartigues, P. P. de Deyn, K. de Paiva Lopes, L. D. de Witte, S. Debette, J. Deckert, T. Del Ser, N. Denning, A. DeStefano, M.

Dichgans, J. Diehl-Schmid, M. Diez-Fairen, P. D. Rossi, S. Djurovic, E. Duron, E. Düzel, C. Dufouil, G. Eiriksdottir, S. Engelborghs, V. Escott-Price, A. Espinosa, M. Ewers, K. M. Faber, T. Fabrizio, S. F. Nielsen, D. W. Fardo, L. Farotti, C. Fenoglio, M. Fernández-Fuertes, R. Ferrari, C. B. Ferreira, E. Ferri, B. Fin, P. Fischer, T. Fladby, K. Fließbach, B. Fongang, M. Fornage, J. Fortea, T. M. Foroud, S. Fostinelli, N. C. Fox, E. Franco-Macías, M. J. Bullido, A. Frank-García, L. Froelich, B. Fulton-Howard, D. Galimberti, J. M. García-Alberca, P. García-González, S. Garcia-Madrona, G. Garcia-Ribas, R. Ghidoni, I. Giegling, G. Giorgio, A. M. Goate, O. Goldhardt, D. Gomez-Fonseca, A. González-Pérez, C. Graff, G. Grande, E. Green, T. Grimmer, E. Grünblatt, M. Grunin, V. Gudnason, T. Guetta-Baranes, A. Haapasalo, G. Hadjigeorgiou, J. L. Haines, K. L. Hamilton-Nelson, H. Hampel, O. Hanon, J. Hardy, A. M. Hartmann, L. Hausner, J. Harwood, S. Heilmann-Heimbach, S. Helisalmi, M. T. Heneka, I. Hernández, M. J. Herrmann, P. Hoffmann, C. Holmes, H. Holstege, R. H. Vilas, M. Hulsman, J. Humphrey, G. J. Biessels, X. Jian, C. Johansson, G. R. Jun, Y. Kastumata, J. Kauwe, P. G. Kehoe, L. Kilander, A. K. Ståhlbom, M. Kivipelto, A. Koivisto, J. Kornhuber, M. H. Kosmidis, W. A. Kukull, P. P. Kuksa, B. W. Kunkle, A. B. Kuzma, C. Lage, E. J. Laukka, L. Launer, A. Lauria, C.-Y. Lee, J. Lehtisalo, O. Lerch, A. Lleó, W. Longstreth Jr, O. Lopez, A. L. de Munain, S. Love, M. Löwemark, L. Luckcuck, K. L. Lunetta, Y. Ma, J. Macías, C. A. MacLeod, W. Maier, F. Mangialasche, M. Spallazzi, M. Marquié, R. Marshall, E. R. Martin, A. M. Montes, C. M. Rodríguez, C. Masullo, R. Mayeux, S. Mead, P. Mecocci, M. Medina, A. Meggy, S. Mehrabian, S. Mendoza, M. Menéndez-González, P. Mir, S. Moebus, M. Mol, L. Molina-Porcel, L. Montrreal, L. Morelli, F. Moreno, K. Morgan, T. Mosley, M. M. Nöthen, C. Muchnik, S. Mukherjee, B. Nacmias, T. Ngandu, G. Nicolas, B. G. Nordestgaard, R. Olaso, A. Orellana, M. Orsini, G. Ortega, A. Padovani, C. Paolo, G. Papenberg, L. Parnetti, F. Pasquier, P. Pastor, G. Peloso, A. Pérez-Cordón, J. Pérez-Tur, P. Pericard, O. Peters, Y. A. L. Pijnenburg, J. A. Pineda, G. Piñol-Ripoll, C. Pisanu, T. Polak, J. Popp, D. Posthuma, J. Priller, R. Puerta, O. Quenez, I. Quintela, J. Q. Thomassen, A. Rábano, I. Rainero, F. Rajabli, I. Ramakers, L. M. Real, M. J. T. Reinders, C. Reitz, D. Reyes-Dumeyer, P. Ridge, S. Riedel-Heller, P. Riederer, N. Roberto, E. Rodriguez-Rodriguez, A. Rongve, I. R. Allende, M. Rosende-Roca, J. L. Royo, E. Rubino, D. Rujescu, M. E. Sáez, P. Sakka, I. Saltvedt, Á. Sanabria, M. B. Sánchez-Arjona, F. Sanchez-Garcia, P. S. Juan, R. Sánchez-Valle, S. B. Sando, C. Sarnowski, C. L. Satizabal, M. Scamosci, N. Scarmeas, E. Scarpini, P. Scheltens, N. Scherbaum, M. Scherer, M. Schmid, A. Schneider, J. M. Schott, G. Selbæk, D. Seripa, M. Serrano, J. Sha, A. A. Shadrin, O. Skrobot, S. Slifer, G. J. L. Snijders, H. Soininen, V. Solfrizzi, A. Solomon, Y. Song, S. Sorbi, O. Sotolongo-Grau, G. Spalletta, A. Spottke, A. Squassina, E. Stordal, J. P. Tartan, L. Tárraga, N. Tesí, A. Thalamuthu, T. Thomas, G. Tosto, L. Traykov, L. Tremolizzo, A. Tybjærg-Hansen, A. Uitterlinden, A. Ullgren, I. Ulstein, S. Valero, O. Valladares, C. Van Broeckhoven, J. Vance, B. N. Vardarajan, A. van der Lugt, J. Van Dongen, J. van Rooij, J. van Swieten, R. Vandenberghe, F. Verhey, J.-S. Vidal, J. Vogelgsang, M. Vyhnalek, M. Wagner, D. Wallon, L.-S. Wang, R. Wang, L. Weinhold, J. Wiltfang, G. Windle, B. Woods, M. Yannakoulia, H. Zare, Y. Zhao, X. Zhang, C. Zhu, M. Zulaica, EADB, GR@ACE, DEGESCO, EADI, GERAD, Demgene, FinnGen, ADGC, CHARGE, L. A. Farrer, B. M. Psaty, M. Ghanbari, T. Raj, P. Sachdev, K. Mather, F. Jessen, M. A. Ikram, A. de Mendonça, J. Hort, M. Tsolaki, M. A. Pericak-Vance, P. Amouyel, J. Williams, R. Frikke-Schmidt, J. Clarimon, J.-F. Deleuze, G. Rossi, S. Seshadri, O. A. Andreassen, M. Ingelsson, M. Hiltunen, K. Sleegers, G. D. Schellenberg, C. M. van Duijn, R. Sims, W. M. van der Flier, A. Ruiz, A. Ramirez, J.-C. Lambert, New insights into the genetic etiology of Alzheimer's disease and related dementias. *Nat. Genet.* **54**, 412–436 (2022).

9. R. Kosoy, J. F. Fullard, B. Zeng, J. Bendl, P. Dong, S. Rahman, S. P. Kleopoulos, Z. Shao, K. Girdhar, J. Humphrey, K. de Paiva Lopes, A. W. Charney, B. H. Kopell, T. Raj, D. Bennett, C. P. Kellner, V. Haroutunian, G. E. Hoffman, P. Roussos, Genetics of the human microglia regulome refines Alzheimer's disease risk loci. *Nat. Genet.* **54**, 1145–1154 (2022).

10. Y. Chen, M. Colonna, Two-faced behavior of microglia in Alzheimer's disease. *Nat. Neurosci.* **25**, 3–4 (2022).

11. M. Olah, V. Menon, N. Habib, M. F. Taga, Y. Ma, C. J. Yung, M. Cimpean, A. Khairallah, G. Coronas-Samano, R. Sankowski, D. Grün, A. A. Kroshilina, D. Dionne, R. A. Sarkis, G. R. Cosgrove, J. Helgager, J. A. Golden, P. B. Pennell, M. Prinz, J. P. G. Vonsattel, A. F. Teich, J. A. Schneider, D. A. Bennett, A. Regev, W. Elyaman, E. M. Bradshaw, P. L. De Jager, Single cell RNA sequencing of human microglia uncovers a subset associated with Alzheimer's disease. *Nat. Commun.* **11**, 6129 (2020).

12. H. Mathys, J. Davila-Velderrain, Z. Peng, F. Gao, S. Mohammadi, J. Z. Young, M. Menon, L. He, F. Abdurrob, X. Jiang, A. J. Martorell, R. M. Ransohoff, B. P. Hafler, D. A. Bennett, M. Kellis, L.-H. Tsai, Single-cell transcriptomic analysis of Alzheimer's disease. *Nature* **570**, 332–337 (2019).

13. T. Masuda, R. Sankowski, O. Staszewski, C. Böttcher, L. Amann, Sagar, C. Scheiwe, S. Nessler, P. Kunz, G. van Loo, V. A. Coenen, P. C. Reinacher, A. Michel, U. Sure, R. Gold, D. Grün, J. Priller, C. Stadelmann, M. Prinz, Spatial and temporal heterogeneity of mouse and human microglia at single-cell resolution. *Nature* **566**, 388–392 (2019).

14. N. Sun, M. B. Victor, Y. P. Park, X. Xiong, A. N. Scannail, N. Leary, S. Prosper, S. Viswanathan, X. Luna, C. A. Boix, B. T. James, Y. Tanigawa, K. Galani, H. Mathys, X. Jiang, A. P. Ng, D. A. Bennett, L.-H. Tsai, M. Kellis, Human microglial state dynamics in Alzheimer's disease progression. *Cell* **186**, 4386–4403.e29 (2023).

15. R. C. Paolicelli, A. Sierra, B. Stevens, M.-E. Tremblay, A. Aguzzi, B. Ajami, I. Amit, E. Audinat, I. Bechmann, M. Bennett, F. Bennett, A. Bessis, K. Biber, S. Bilbo, M. Blurton-Jones, E. Boddeke, D. Brites, B. Brône, G. C. Brown, O. Butovsky, M. J. Carson, B. Castellano, M. Colonna, S. A. Cowley, C. Cunningham, D. Davalos, P. L. De Jager, B. de Strooper, A. Denes, B. J. L. Eggen, U. Eyo, E. Galea, S. Garel, F. Ginhoux, C. K. Glass, O. Gokce, D. Gomez-Nicola, B. González, S. Gordon, M. B. Graeber, A. D. Greenhalgh, P. Gressens, M. Greter, D. H. Gutmann, C. Haass, M. T. Heneka, F. L. Heppner, S. Hong, D. A. Hume, S. Jung, H. Kettenmann, J. Kipnis, R. Koyama, G. Lemke, M. Lynch, A. Majewska, M. Malcangio, T. Malm, R. Mancuso, T. Masuda, M. Matteoli, B. W. McColl, V. E. Miron, A. V. Molofsky, M. Monje, E. Mracsko, A. Nadjar, J. J. Neher, U. Neniskyte, H. Neumann, M. Noda, B. Peng, F. Peri, V. H. Perry, P. G. Popovich, C. Pridans, J. Priller, M. Prinz, D. Ragozzino, R. M. Ransohoff, M. W. Salter, A. Schaefer, D. P. Schafer, M. Schwartz, M. Simons, C. J. Smith, W. J. Streit, T. L. Tay, L.-H. Tsai, A. Verkhratsky, R. von Bernhardi, H. Wake, V. Wittamer, S. A. Wolf, L.-J. Wu, T. Wyss-Coray, Microglia states and nomenclature: A field at its crossroads. *Neuron* **110**, 3458–3483 (2022).

16. N. Thrupp, C. Sala Frigerio, L. Wolfs, N. G. Skene, N. Fattorelli, S. Poovathingal, Y. Fourne, P. M. Matthews, T. Theys, R. Mancuso, B. de Strooper, M. Fiers, Single-Nucleus RNA-Seq Is Not Suitable for Detection of Microglial Activation Genes in Humans. *Cell Rep.* **32**, 108189 (2020).

17. S. E. Marsh, A. J. Walker, T. Kamath, L. Dissing-Olesen, T. R. Hammond, T. Y. de Soysa, A. M. H. Young, S. Murphy, A. Abdulraouf, N. Nadaf, C. Dufort, A. C. Walker, L. E. Lucca, V. Kozareva, C. Vanderburg, S. Hong, H. Bulstrode, P. J. Hutchinson, D. J. Gaffney, D. A. Hafler, R. J. M. Franklin, E. Z. Macosko, B. Stevens, Dissection of artifactual and confounding glial signatures by single-cell sequencing of mouse and human brain. *Nat. Neurosci.* **25**, 306–316 (2022).

18. M. Stoeckius, C. Hafemeister, W. Stephenson, B. Houck-Loomis, P. K. Chattopadhyay, H. Swerdlow, R. Satija, P. Smibert, Simultaneous epitope and transcriptome measurement in single cells. *Nat. Methods* **14**, 865–868 (2017).

19. S. S. Mirra, A. Heyman, D. McKeel, S. M. Sumi, B. J. Crain, L. M. Brownlee, F. S. Vogel, J. P. Hughes, G. van Belle, L. Berg, The Consortium to Establish a Registry for Alzheimer's Disease (CERAD). Part II. Standardization of the neuropathologic assessment of Alzheimer's disease. *Neurology* **41**, 479–486 (1991).

20. H. Braak, E. Braak, Evolution of the neuropathology of Alzheimer's disease. *Acta Neurol. Scand. Suppl.* **165**, 3–12 (1996).

21. A. Ajoolabady, D. Lindholm, J. Ren, D. Pratico, ER stress and UPR in Alzheimer's disease: mechanisms, pathogenesis, treatments. *Cell Death Dis.* **13**, 706 (2022).

22. A. M. Smith, K. Davey, S. Tsartsalis, C. Khozoie, N. Fancy, S. S. Tang, E. Liaptsi, M. Weinert, A. McGarry, R. C. J. Muirhead, S. Gentleman, D. R. Owen, P. M. Matthews, Diverse human astrocyte and microglial transcriptional responses to Alzheimer's pathology. *Acta Neuropathol.* **143**, 75–91 (2022).

23. M.-J. Dolan, M. Therrien, S. Jereb, T. Kamath, V. Gazestani, T. Atkeson, S. E. Marsh, A. Goeva, N. M. Lojek, S. Murphy, C. M. White, J. Joung, B. Liu, F. Limone, K. Eggan, N. Hacohen, B. E. Bernstein, C. K. Glass, V. Leinonen, M. Blurton-Jones, F. Zhang, C. B. Epstein, E. Z. Macosko, B. Stevens, Exposure of iPSC-derived human microglia to brain substrates enables the generation and manipulation of diverse transcriptional states in vitro. *Nat. Immunol.* **24**, 1382–1390 (2023).

24. J. Marschallinger, T. Iram, M. Zardeneta, S. E. Lee, B. Lehallier, M. S. Haney, J. V. Pluvinage, V. Mathur, O. Hahn, D. W. Morgens, J. Kim, J. Tevini, T. K. Felder, H. Wolinski, C. R. Bertozzi, M. C. Bassik, L. Aigner, T. Wyss-Coray, Lipid-droplet-accumulating microglia represent a dysfunctional and proinflammatory state in the aging brain. *Nat. Neurosci.* **23**, 194–208 (2020).

25. A. Silvin, S. Uderhardt, C. Piot, S. Da Mesquita, K. Yang, L. Geirsdottir, K. Mulder, D. Eyal, Z. Liu, C. Bridlance, M. S. Thion, X. M. Zhang, W. T. Kong, M. Deloger, V. Fontes, A. Weiner, R. Ee, R. Dress, J. W. Hang, A. Balachander, S. Chakarov, B. Malleret, G. Dunsmore, O. Cexus, J. Chen, S. Garel, C. A. Dutertre, I. Amit, J. Kipnis, F. Ginhoux, Dual ontogeny of disease-associated microglia and disease inflammatory macrophages in aging and neurodegeneration. *Immunity* **55**, 1448–1465.e6 (2022).

26. A. C. Lieber, I. T. McNeill, J. Scaggiante, D. A. Nistal, M. Fowkes, M. Umphlett, J. Pan, P. Roussos, C. V. Mobbs, J. Mocco, C. P. Kellner, Biopsy During Minimally Invasive Intracerebral Hemorrhage Clot Evacuation. *World Neurosurg.*, doi:

10.1016/j.wneu.2018.12.058 (2018).

27. Y. Zhou, W. M. Song, P. S. Andhey, A. Swain, T. Levy, K. R. Miller, P. L. Poliani, M. Cominelli, S. Grover, S. Gilfillan, M. Cella, T. K. Ulland, K. Zaitsev, A. Miyashita, T. Ikeuchi, M. Sainouchi, A. Kakita, D. A. Bennett, J. A. Schneider, M. R. Nichols, S. A. Beausoleil, J. D. Ulrich, D. M. Holtzman, M. N. Artyomov, M. Colonna, Human and mouse single-nucleus transcriptomics reveal TREM2-dependent and TREM2-independent cellular responses in Alzheimer's disease. *Nat. Med.* **26**, 131–142 (2020).

28. J. Ma, J.-T. Yu, L. Tan, MS4A Cluster in Alzheimer's Disease. *Mol. Neurobiol.* **51**, 1240–1248 (2015).

29. D. Klein, G. Palla, M. Lange, M. Klein, Z. Piran, M. Gander, L. Meng-Papaxanthos, M. Sterr, A. Bastidas-Ponce, M. Tarquis-Medina, H. Lickert, M. Bakhti, M. Nitzan, M. Cuturi, F. J. Theis, Mapping cells through time and space with moscot, *bioRxiv* (2023)p. 2023.05.11.540374.

30. P. Weiler, M. Lange, M. Klein, D. Pe'er, F. J. Theis, Unified fate mapping in multiview single-cell data, *bioRxiv* (2023)p. 2023.07.19.549685.

31. S. Aibar, C. B. González-Blas, T. Moerman, V. A. Huynh-Thu, H. Imrichova, G. Hulselmans, F. Rambow, J.-C. Marine, P. Geurts, J. Aerts, J. van den Oord, Z. K. Atak, J. Wouters, S. Aerts, SCENIC: single-cell regulatory network inference and clustering. *Nat. Methods* **14**, 1083–1086 (2017).

32. B. Van de Sande, C. Flerin, K. Davie, M. De Waegeneer, G. Hulselmans, S. Aibar, R. Seurinck, W. Saelens, R. Cannoodt, Q. Rouchon, T. Verbeiren, D. De Maeyer, J. Reumers, Y. Saeys, S. Aerts, A scalable SCENIC workflow for single-cell gene regulatory network analysis. *Nat. Protoc.* **15**, 2247–2276 (2020).

33. D. Dimitrov, D. Türei, M. Garrido-Rodriguez, P. L. Burmedi, J. S. Nagai, C. Boys, R. O. Ramirez Flores, H. Kim, B. Szalai, I. G. Costa, A. Valdeolivas, A. Dugourd, J. Saez-Rodriguez, Comparison of methods and resources for cell-cell communication inference from single-cell RNA-Seq data. *Nat. Commun.* **13**, 3224 (2022).

34. C. A. de Leeuw, J. M. Mooij, T. Heskes, D. Posthuma, MAGMA: generalized gene-set analysis of GWAS data. *PLoS Comput. Biol.* **11**, e1004219 (2015).

35. Y. Wang, M. Cella, K. Mallinson, J. D. Ulrich, K. L. Young, M. L. Robinette, S. Gilfillan, G. M. Krishnan, S. Sudhakar, B. H. Zinselmeyer, D. M. Holtzman, J. R. Cirrito, M. Colonna, TREM2 lipid sensing sustains the microglial response in an Alzheimer's disease model. *Cell* **160**, 1061–1071 (2015).

36. T. R. Jay, C. M. Miller, P. J. Cheng, L. C. Graham, S. Bemiller, M. L. Broihier, G. Xu, D. Margevicius, J. C. Karlo, G. L. Sousa, A. C. Cotleur, O. Butovsky, L. Bekris, S. M. Staugaitis, J. B. Leverenz, S. W. Pimplikar, G. E. Landreth, G. R. Howell, R. M. Ransohoff, B. T. Lamb, TREM2 deficiency eliminates TREM2+ inflammatory macrophages and ameliorates pathology in Alzheimer's disease mouse models. *J. Exp. Med.* **212**, 287–295 (2015).

1790 37. P. Yuan, C. Condello, C. D. Keene, Y. Wang, T. D. Bird, S. M. Paul, W. Luo, M. Colonna, D.
1791 Baddeley, J. Grutzendler, TREM2 haplodeficiency in mice and humans impairs the
1792 microglia barrier function leading to decreased amyloid compaction and severe axonal
1793 dystrophy. *Neuron* **90**, 724–739 (2016).

1794 38. Y. Wang, T. K. Ulland, J. D. Ulrich, W. Song, J. A. Tzaferis, J. T. Hole, P. Yuan, T. E.
1795 Mahan, Y. Shi, S. Gilfillan, M. Cella, J. Grutzendler, R. B. DeMattos, J. R. Cirrito, D. M.
1796 Holtzman, M. Colonna, TREM2-mediated early microglial response limits diffusion and
1797 toxicity of amyloid plaques. *J. Exp. Med.* **213**, 667–675 (2016).

1798 39. T. K. Ulland, M. Colonna, TREM2 - a key player in microglial biology and Alzheimer
1799 disease. *Nat. Rev. Neurol.* **14**, 667–675 (2018).

1800 40. W. M. Song, S. Joshita, Y. Zhou, T. K. Ulland, S. Gilfillan, M. Colonna, Humanized TREM2
1801 mice reveal microglia-intrinsic and -extrinsic effects of R47H polymorphism. *J. Exp. Med.*
1802 **215**, 745–760 (2018).

1803 41. H. Tanaka, M. Shimazawa, M. Kimura, M. Takata, K. Tsuruma, M. Yamada, H. Takahashi,
1804 I. Hozumi, J.-I. Niwa, Y. Iguchi, T. Nikawa, G. Sobue, T. Inuzuka, H. Hara, The potential of
1805 GPNMB as novel neuroprotective factor in amyotrophic lateral sclerosis. *Sci. Rep.* **2**, 573
1806 (2012).

1807 42. M. L. Neal, A. M. Boyle, K. M. Budge, F. F. Safadi, J. R. Richardson, The glycoprotein
1808 GPNMB attenuates astrocyte inflammatory responses through the CD44 receptor. *J.*
1809 *Neuroinflammation* **15**, 73 (2018).

1810 43. D. A. Kia, D. Zhang, S. Guelfi, C. Manzoni, L. Hubbard, R. H. Reynolds, J. Botía, M. Ryten,
1811 R. Ferrari, P. A. Lewis, N. Williams, D. Trabzuni, J. Hardy, N. W. Wood, United Kingdom
1812 Brain Expression Consortium (UKBEC) and the International Parkinson's Disease
1813 Genomics Consortium (IPDGC), Identification of Candidate Parkinson Disease Genes by
1814 Integrating Genome-Wide Association Study, Expression, and Epigenetic Data Sets. *JAMA*
1815 *Neurol.* **78**, 464–472 (2021).

1816 44. C. S. Storm, D. A. Kia, M. M. Almramhi, S. Bandres-Ciga, C. Finan, International
1817 Parkinson's Disease Genomics Consortium (IPDGC), A. D. Hingorani, N. W. Wood, Finding
1818 genetically-supported drug targets for Parkinson's disease using Mendelian randomization
1819 of the druggable genome. *Nat. Commun.* **12**, 7342 (2021).

1820 45. M. Hüttenrauch, I. Ogorek, H. Klafki, M. Otto, C. Stadelmann, S. Weggen, J. Wiltfang, O.
1821 Wirths, Glycoprotein NMB: a novel Alzheimer's disease associated marker expressed in a
1822 subset of activated microglia. *Acta Neuropathol. Commun.* **6**, 108 (2018).

1823 46. M. Liguori, E. Digifico, A. Vacchini, R. Avigni, F. S. Colombo, E. M. Borroni, F. M. Farina, S.
1824 Milanesi, A. Castagna, L. Mannarino, I. Craparotta, S. Marchini, E. Erba, N. Panini, M.
1825 Tamborini, V. Rimoldi, P. Allavena, C. Belgiovine, The soluble glycoprotein NMB (GPNMB)
1826 produced by macrophages induces cancer stemness and metastasis via CD44 and IL-33.
1827 *Cell. Mol. Immunol.* **18**, 711–722 (2021).

1828 47. Y. Lin, Y. Qi, M. Jiang, W. Huang, B. Li, Lactic acid-induced M2-like macrophages
1829 facilitate tumor cell migration and invasion via the GPNMB/CD44 axis in oral squamous

cell carcinoma. *Int. Immunopharmacol.* **124**, 110972 (2023).

48. J. Doroszkiewicz, A. Kulczyńska-Przybik, M. Dulewicz, R. Borawska, M. Zajkowska, A. Słowik, B. Mroczko, Potential utility of cerebrospinal fluid glycoprotein nonmetastatic melanoma protein B as a neuroinflammatory diagnostic biomarker in mild cognitive impairment and Alzheimer's disease. *J. Clin. Med.* **12** (2023).

49. J. Doroszkiewicz, A. Kulczynska-Przybik, M. Dulewicz, R. Borawska, A. Slowik, B. Mroczko, The cerebrospinal fluid Glycoprotein Nonmetastatic Melanoma Protein B (GPNMB) concentration in Alzheimer's Disease (AD). *Alzheimers. Dement.* **19** (2023).

50. K. Srinivasan, B. A. Friedman, A. Etxeberria, M. A. Huntley, M. P. van der Brug, O. Foreman, J. S. Paw, Z. Modrusan, T. G. Beach, G. E. Serrano, D. V. Hansen, Alzheimer's Patient Microglia Exhibit Enhanced Aging and Unique Transcriptional Activation. *Cell Rep.* **31**, 107843 (2020).

51. T. Schwabe, K. Srinivasan, H. Rhinn, Shifting paradigms: The central role of microglia in Alzheimer's disease. *Neurobiol. Dis.* **143**, 104962 (2020).

52. F. Agostini, R. Agostinis, D. L. Medina, M. Bisaglia, E. Greggio, N. Plotegher, The Regulation of MiTF/TFE Transcription Factors Across Model Organisms: from Brain Physiology to Implication for Neurodegeneration. *Mol. Neurobiol.* **59**, 5000–5023 (2022).

53. J. Miao, H. Ma, Y. Yang, Y. Liao, C. Lin, J. Zheng, M. Yu, J. Lan, Microglia in Alzheimer's disease: pathogenesis, mechanisms, and therapeutic potentials. *Front. Aging Neurosci.* **15**, 1201982 (2023).

54. B. A. Friedman, K. Srinivasan, G. Ayalon, W. J. Meilandt, H. Lin, M. A. Huntley, Y. Cao, S.-H. Lee, P. C. G. Haddick, H. Ngu, Z. Modrusan, J. L. Larson, J. S. Kaminker, M. P. van der Brug, D. V. Hansen, Diverse Brain Myeloid Expression Profiles Reveal Distinct Microglial Activation States and Aspects of Alzheimer's Disease Not Evident in Mouse Models. *Cell Rep.* **22**, 832–847 (2018).

55. D. A. Bennett, A. S. Buchman, P. A. Boyle, L. L. Barnes, R. S. Wilson, J. A. Schneider, Religious Orders Study and Rush Memory and Aging Project. *J. Alzheimers. Dis.* **64**, S161–S189 (2018).

56. D. A. Bennett, J. A. Schneider, Z. Arvanitakis, J. F. Kelly, N. T. Aggarwal, R. C. Shah, R. S. Wilson, Neuropathology of older persons without cognitive impairment from two community-based studies. *Neurology* **66**, 1837–1844 (2006).

57. D. A. Bennett, R. S. Wilson, J. A. Schneider, D. A. Evans, L. A. Beckett, N. T. Aggarwal, L. L. Barnes, J. H. Fox, J. Bach, Natural history of mild cognitive impairment in older persons. *Neurology* **59**, 198–205 (2002).

58. D. A. Bennett, J. A. Schneider, N. T. Aggarwal, Z. Arvanitakis, R. C. Shah, J. F. Kelly, J. H. Fox, E. J. Cochran, D. Arends, A. D. Treinkman, R. S. Wilson, Decision rules guiding the clinical diagnosis of Alzheimer's disease in two community-based cohort studies compared to standard practice in a clinic-based cohort study. *Neuroepidemiology* **27**, 169–176 (2006).

59. H. Braak, E. Braak, Neuropathological stageing of Alzheimer-related changes. *Acta Neuropathol.* **82**, 239–259 (1991).

60. H. Braak, I. Alafuzoff, T. Arzberger, H. Kretzschmar, K. Del Tredici, Staging of Alzheimer disease-associated neurofibrillary pathology using paraffin sections and immunocytochemistry. *Acta Neuropathol.* **112**, 389–404 (2006).

61. H. Braak, D. R. Thal, E. Ghebremedhin, K. Del Tredici, Stages of the pathologic process in Alzheimer disease: age categories from 1 to 100 years. *J. Neuropathol. Exp. Neurol.* **70**, 960–969 (2011).

62. M. Stoeckius, S. Zheng, B. Houck-Loomis, S. Hao, B. Z. Yeung, W. M. Mauck 3rd, P. Smibert, R. Satija, Cell Hashing with barcoded antibodies enables multiplexing and doublet detection for single cell genomics. *Genome Biol.* **19**, 224 (2018).

63. S. J. Fleming, M. D. Chaffin, A. Arduini, A.-D. Akkad, E. Banks, J. C. Marioni, A. A. Philippakis, P. T. Ellinor, M. Babadi, Unsupervised removal of systematic background noise from droplet-based single-cell experiments using CellBender. *Nat. Methods* **20**, 1323–1335 (2023).

64. B. Li, J. Gould, Y. Yang, S. Sarkizova, M. Tabaka, O. Ashenberg, Y. Rosen, M. Slyper, M. S. Kowalczyk, A.-C. Villani, T. Tickle, N. Hacohen, O. Rozenblatt-Rosen, A. Regev, Cumulus provides cloud-based data analysis for large-scale single-cell and single-nucleus RNA-seq. *Nat. Methods* **17**, 793–798 (2020).

65. S. L. Wolock, R. Lopez, A. M. Klein, Scrublet: Computational Identification of Cell Doublets in Single-Cell Transcriptomic Data. *Cell Syst* **8**, 281–291.e9 (2019).

66. I. Korsunsky, N. Millard, J. Fan, K. Slowikowski, F. Zhang, K. Wei, Y. Baglaenko, M. Brenner, P.-R. Loh, S. Raychaudhuri, Fast, sensitive and accurate integration of single-cell data with Harmony. *Nat. Methods* **16**, 1289–1296 (2019).

67. V. A. Traag, L. Waltman, N. J. van Eck, From Louvain to Leiden: guaranteeing well-connected communities. *Sci. Rep.* **9**, 5233 (2019).

68. L. McInnes, J. Healy, J. Melville, UMAP: Uniform Manifold Approximation and Projection for Dimension Reduction, *arXiv [stat.ML]* (2018). http://arxiv.org/abs/1802.03426.

69. C. Xu, R. Lopez, E. Mehlman, J. Regier, M. I. Jordan, N. Yosef, Probabilistic harmonization and annotation of single-cell transcriptomics data with deep generative models. *Mol. Syst. Biol.* **17**, e9620 (2021).

70. A. Dobin, C. A. Davis, F. Schlesinger, J. Drenkow, C. Zaleski, S. Jha, P. Batut, M. Chaisson, T. R. Gingeras, STAR: ultrafast universal RNA-seq aligner. *Bioinformatics* **29**, 15–21 (2013).

71. B. Kaminow, D. Yunusov, A. Dobin, STARsolo: accurate, fast and versatile mapping/quantification of single-cell and single-nucleus RNA-seq data, *bioRxiv* (2021)p. 2021.05.05.442755.

72. Y. Huang, D. J. McCarthy, O. Stegle, Vireo: Bayesian demultiplexing of pooled single-cell

RNA-seq data without genotype reference. *Genome Biol.* **20**, 273 (2019).

73. F. A. Wolf, P. Angerer, F. J. Theis, SCANPY: large-scale single-cell gene expression data analysis. *Genome Biol.* **19**, 15 (2018).

74. S. Ma, M. Skarica, Q. Li, C. Xu, R. D. Risgaard, A. T. N. Tebbenkamp, X. Mato-Blanco, R. Kovner, Ž. Krsnik, X. de Martin, V. Luria, X. Martí-Pérez, D. Liang, A. Karger, D. K. Schmidt, Z. Gomez-Sanchez, C. Qi, K. T. Gobeske, S. Pochareddy, A. Debnath, C. J. Hottman, J. Spurrier, L. Teo, A. G. Boghdadi, J. Homman-Ludiye, J. J. Ely, E. W. Daadi, D. Mi, M. Daadi, O. Marín, P. R. Hof, M.-R. Rasin, J. Bourne, C. C. Sherwood, G. Santpere, M. J. Girgenti, S. M. Strittmatter, A. M. M. Sousa, N. Sestan, Molecular and cellular evolution of the primate dorsolateral prefrontal cortex. *Science* **377**, eabo7257 (2022).

75. N. Bray, H. Pimentel, P. Melsted, L. Pachter, Near-optimal RNA-Seq quantification with kallisto. *Nat. Biotechnol.*

76. P. Bankhead, M. B. Loughrey, J. A. Fernández, Y. Dombrowski, D. G. McArt, P. D. Dunne, S. McQuaid, R. T. Gray, L. J. Murray, H. G. Coleman, J. A. James, M. Salto-Tellez, P. W. Hamilton, QuPath: Open source software for digital pathology image analysis. *Sci. Rep.* **7**, 16878 (2017).

77. A. Gayoso, R. Lopez, G. Xing, P. Boyeau, V. Valiollah Pour Amiri, J. Hong, K. Wu, M. Jayasuriya, E. Mehlman, M. Langevin, Y. Liu, J. Samaran, G. Misrachi, A. Nazaret, O. Clivio, C. Xu, T. Ashuach, M. Gabitto, M. Lotfollahi, V. Svensson, E. da Veiga Beltrame, V. Kleshchevnikov, C. Talavera-López, L. Pachter, F. J. Theis, A. Streets, M. I. Jordan, J. Regier, N. Yosef, A Python library for probabilistic analysis of single-cell omics data. *Nat. Biotechnol.* **40**, 163–166 (2022).

78. I. Virshup, D. Bredikhin, L. Heumos, G. Palla, G. Sturm, A. Gayoso, I. Kats, M. Koutrouli, Scverse Community, B. Berger, D. Pe'er, A. Regev, S. A. Teichmann, F. Finotello, F. A. Wolf, N. Yosef, O. Stegle, F. J. Theis, The scverse project provides a computational ecosystem for single-cell omics data analysis. *Nat. Biotechnol.* **41**, 604–606 (2023).

79. D. Mattei, A. Ivanov, M. van Oostrum, S. Pantelyushin, J. Richetto, F. Mueller, M. Beffinger, L. Schellhammer, J. Vom Berg, B. Wollscheid, D. Beule, R. C. Paolicelli, U. Meyer, Enzymatic Dissociation Induces Transcriptional and Proteotype Bias in Brain Cell Populations. *Int. J. Mol. Sci.* **21** (2020).

80. S. Krasemann, C. Madore, R. Cialic, C. Baufeld, N. Calcagno, R. El Fatimy, L. Beckers, E. O'Loughlin, Y. Xu, Z. Fanek, D. J. Greco, S. T. Smith, G. Tweet, Z. Humulock, T. Zrzavy, P. Conde-Sanroman, M. Gacias, Z. Weng, H. Chen, E. Tjon, F. Mazaheri, K. Hartmann, A. Madi, J. D. Ulrich, M. Glatzel, A. Worthmann, J. Heeren, B. Budnik, C. Lemere, T. Ikezu, F. L. Heppner, V. Litvak, D. M. Holtzman, H. Lassmann, H. L. Weiner, J. Ochando, C. Haass, O. Butovsky, The TREM2-APOE pathway drives the transcriptional phenotype of dysfunctional microglia in neurodegenerative diseases. *Immunity* **47**, 566–581.e9 (2017).

81. Cell Press: STAR Protocols. https://star-protocols.cell.com/protocols/694.

82. L. Li, X. Cao, L. Huang, X. Huang, J. Gu, X. Yu, Y. Zhu, Y. Zhou, Y. Song, M. Zhu, Lycopene inhibits endothelial-to-mesenchymal transition of choroidal vascular endothelial

cells in laser-induced mouse choroidal neovascularization. *J. Cell. Mol. Med.* **27**, 1327–1340 (2023).

83. G. E. Hoffman, P. Roussos, Dream: powerful differential expression analysis for repeated measures designs. *Bioinformatics* **37**, 192–201 (2021).

84. J. W. Squair, M. Gautier, C. Kathe, M. A. Anderson, N. D. James, T. H. Hutson, R. Hudelle, T. Qaiser, K. J. E. Matson, Q. Barraud, A. J. Levine, G. La Manno, M. A. Skinnider, G. Courtine, Confronting false discoveries in single-cell differential expression. *Nat. Commun.* **12**, 5692 (2021).

85. H. L. Crowell, C. Soneson, P.-L. Germain, D. Calini, L. Collin, C. Raposo, D. Malhotra, M. D. Robinson, muscat detects subpopulation-specific state transitions from multi-sample multi-condition single-cell transcriptomics data. *Nat. Commun.* **11**, 6077 (2020).

86. D. Wu, G. K. Smyth, Camera: a competitive gene set test accounting for inter-gene correlation. *Nucleic Acids Res.* **40**, e133 (2012).

87. D. Tingley, T. Yamamoto, K. Hirose, L. Keele, K. Imai, Mediation:RPackage for causal mediation analysis. *J. Stat. Softw.* **59**, 1–38 (2014).

88. Z. Fang, X. Liu, G. Peltz, GSEApy: a comprehensive package for performing gene set enrichment analysis in Python. *Bioinformatics* **39** (2023).

89. B. Reuter, K. Fackeldey, M. Weber, Generalized Markov modeling of nonreversible molecular kinetics. *J. Chem. Phys.* **150**, 174103 (2019).

90. L. Haghverdi, M. Büttner, F. A. Wolf, F. Buettner, F. J. Theis, Diffusion pseudotime robustly reconstructs lineage branching. *Nat. Methods* **13**, 845–848 (2016).

91. L. Heumos, A. C. Schaar, C. Lance, A. Litinetskaya, F. Drost, L. Zappia, M. D. Lücken, D. C. Strobl, J. Henao, F. Curion, Single-cell Best Practices Consortium, H. B. Schiller, F. J. Theis, Best practices for single-cell analysis across modalities. *Nat. Rev. Genet.*, 1–23 (2023).

92. R. Kolde, S. Laur, P. Adler, J. Vilo, Robust rank aggregation for gene list integration and meta-analysis. *Bioinformatics* **28**, 573–580 (2012).

93. M. Efremova, M. Vento-Tormo, S. A. Teichmann, R. Vento-Tormo, CellPhoneDB: inferring cell-cell communication from combined expression of multi-subunit ligand-receptor complexes. *Nat. Protoc.* **15**, 1484–1506 (2020).

94. M. S. B. Raredon, J. Yang, J. Garritano, M. Wang, D. Kushnir, J. C. Schupp, T. S. Adams, A. M. Greaney, K. L. Leiby, N. Kaminski, Y. Kluger, A. Levchenko, L. E. Niklason, Computation and visualization of cell-cell signaling topologies in single-cell systems data using Connectome. *Sci. Rep.* **12**, 4187 (2022).

95. R. Hou, E. Denisenko, H. T. Ong, J. A. Ramilowski, A. R. R. Forrest, Predicting cell-to-cell communication networks using NATMI. *Nat. Commun.* **11**, 5011 (2020).

96. S. Cabello-Aguilar, M. Alame, F. Kon-Sun-Tack, C. Fau, M. Lacroix, J. Colinge,

SingleCellSignalR: inference of intercellular networks from single-cell transcriptomics. *Nucleic Acids Res.* **48**, e55 (2020).

97. S. Jin, C. F. Guerrero-Juarez, L. Zhang, I. Chang, R. Ramos, C.-H. Kuan, P. Myung, M. V. Plikus, Q. Nie, Inference and analysis of cell-cell communication using CellChat. *Nat. Commun.* **12**, 1088 (2021).

98. E. Armingol, H. M. Baghdassarian, C. Martino, A. Perez-Lopez, C. Aamodt, R. Knight, N. E. Lewis, Context-aware deconvolution of cell–cell communication with Tensor-cell2cell. *Nat. Commun.* **13**, 1–15 (2022).

99. M. Ashburner, C. A. Ball, J. A. Blake, D. Botstein, H. Butler, J. M. Cherry, A. P. Davis, K. Dolinski, S. S. Dwight, J. T. Eppig, M. A. Harris, D. P. Hill, L. Issel-Tarver, A. Kasarskis, S. Lewis, J. C. Matese, J. E. Richardson, M. Ringwald, G. M. Rubin, G. Sherlock, Gene ontology: tool for the unification of biology. The Gene Ontology Consortium. *Nat. Genet.* **25**, 25–29 (2000).

100. Gene Ontology Consortium, S. A. Aleksander, J. Balhoff, S. Carbon, J. M. Cherry, H. J. Drabkin, D. Ebert, M. Feuermann, P. Gaudet, N. L. Harris, D. P. Hill, R. Lee, H. Mi, S. Moxon, C. J. Mungall, A. Muruganugan, T. Mushayahama, P. W. Sternberg, P. D. Thomas, K. Van Auken, J. Ramsey, D. A. Siegele, R. L. Chisholm, P. Fey, M. C. Aspromonte, M. V. Nugnes, F. Quaglia, S. Tosatto, M. Giglio, S. Nadendla, G. Antonazzo, H. Attrill, G. Dos Santos, S. Marygold, V. Strelets, C. J. Tabone, J. Thurmond, P. Zhou, S. H. Ahmed, P. Asanitthong, D. Luna Buitrago, M. N. Erdol, M. C. Gage, M. Ali Kadhum, K. Y. C. Li, M. Long, A. Michalak, A. Pesala, A. Pritazahra, S. C. C. Saverimuttu, R. Su, K. E. Thurlow, R. C. Lovering, C. Logie, S. Oliferenko, J. Blake, K. Christie, L. Corbani, M. E. Dolan, H. J. Drabkin, D. P. Hill, L. Ni, D. Sitnikov, C. Smith, A. Cuzick, J. Seager, L. Cooper, J. Elser, P. Jaiswal, P. Gupta, P. Jaiswal, S. Naithani, M. Lera-Ramirez, K. Rutherford, V. Wood, J. L. De Pons, M. R. Dwinell, G. T. Hayman, M. L. Kaldunski, A. E. Kwitek, S. J. F. Laulederkind, M. A. Tutaj, M. Vedi, S.-J. Wang, P. D'Eustachio, L. Aimo, K. Axelsen, A. Bridge, N. Hyka-Nouspikel, A. Morgat, S. A. Aleksander, J. M. Cherry, S. R. Engel, K. Karra, S. R. Miyasato, R. S. Nash, M. S. Skrzypek, S. Weng, E. D. Wong, E. Bakker, T. Z. Berardini, L. Reiser, A. Auchincloss, K. Axelsen, G. Argoud-Puy, M.-C. Blatter, E. Boutet, L. Breuza, A. Bridge, C. Casals-Casas, E. Coudert, A. Estreicher, M. Livia Famiglietti, M. Feuermann, A. Gos, N. Gruaz-Gumowski, C. Hulo, N. Hyka-Nouspikel, F. Jungo, P. Le Mercier, D. Lieberherr, P. Masson, A. Morgat, I. Pedruzzi, L. Pourcel, S. Poux, C. Rivoire, S. Sundaram, A. Bateman, E. Bowler-Barnett, H. Bye-A-Jee, P. Denny, A. Ignatchenko, R. Ishtiaq, A. Lock, Y. Lussi, M. Magrane, M. J. Martin, S. Orchard, P. Raposo, E. Speretta, N. Tyagi, K. Warner, R. Zaru, A. D. Diehl, R. Lee, J. Chan, S. Diamantakis, D. Raciti, M. Zarowiecki, M. Fisher, C. James-Zorn, V. Ponferrada, A. Zorn, S. Ramachandran, L. Ruzicka, M. Westerfield, The Gene Ontology knowledgebase in 2023. *Genetics* **224** (2023).

101. International Multiple Sclerosis Genetics Consortium, Multiple sclerosis genomic map implicates peripheral immune cells and microglia in susceptibility. *Science* **365** (2019).

102. M. A. Nalls, C. Blauwendraat, C. L. Vallerga, K. Heilbron, S. Bandres-Ciga, D. Chang, M. Tan, D. A. Kia, A. J. Noyce, A. Xue, J. Bras, E. Young, R. von Coelln, J. Simón-Sánchez, C. Schulte, M. Sharma, L. Krohn, L. Pihlstrøm, A. Siitonen, H. Iwaki, H. Leonard, F. Faghri, J. R. Gibbs, D. G. Hernandez, S. W. Scholz, J. A. Botia, M. Martinez, J.-C. Corvol, S. Lesage, J. Jankovic, L. M. Shulman, M. Sutherland, P. Tienari, K. Majamaa, M.

Toft, O. A. Andreassen, T. Bangale, A. Brice, J. Yang, Z. Gan-Or, T. Gasser, P. Heutink, J. M. Shulman, N. W. Wood, D. A. Hinds, J. A. Hardy, H. R. Morris, J. Gratten, P. M. Visscher, R. R. Graham, A. B. Singleton, 23andMe Research Team, System Genomics of Parkinson's Disease Consortium, International Parkinson's Disease Genomics Consortium, Identification of novel risk loci, causal insights, and heritable risk for Parkinson's disease: a meta-analysis of genome-wide association studies. *Lancet Neurol.* **18**, 1091–1102 (2019).

103. T. D. Als, M. I. Kurki, J. Grove, G. Voloudakis, K. Therrien, E. Tasanko, T. T. Nielsen, J. Naamanka, K. Veerapen, D. F. Levey, J. Bendl, J. Bybjerg-Grauholm, B. Zeng, D. Demontis, A. Rosengren, G. Athanasiadis, M. Bækved-Hansen, P. Qvist, G. Bragi Walters, T. Thorgeirsson, H. Stefánsson, K. L. Musliner, V. M. Rajagopal, L. Farajzadeh, J. Thirstrup, B. J. Vilhjálmsson, J. J. McGrath, M. Mattheisen, S. Meier, E. Agerbo, K. Stefánsson, M. Nordentoft, T. Werge, D. M. Hougaard, P. B. Mortensen, M. B. Stein, J. Gelernter, I. Hovatta, P. Roussos, M. J. Daly, O. Mors, A. Palotie, A. D. Børglum, Depression pathophysiology, risk prediction of recurrence and comorbid psychiatric disorders using genome-wide analyses. *Nat. Med.* **29**, 1832–1844 (2023).

104. J. Grove, S. Ripke, T. D. Als, M. Mattheisen, R. K. Walters, H. Won, J. Pallesen, E. Agerbo, O. A. Andreassen, R. Anney, Others, Identification of common genetic risk variants for autism spectrum disorder. *Nat. Genet.* **51**, 431–444 (2019).

105. N. Mullins, A. J. Forstner, K. S. O'Connell, B. Coombes, J. R. I. Coleman, Z. Qiao, T. D. Als, T. B. Bigdeli, S. Børte, J. Bryois, A. W. Charney, O. K. Drange, M. J. Gandal, S. P. Hagenaars, M. Ikeda, N. Kamitaki, M. Kim, K. Krebs, G. Panagiotaropoulou, B. M. Schilder, L. G. Sloofman, S. Steinberg, V. Trubetskoy, B. S. Winsvold, H.-H. Won, L. Abramova, K. Adorjan, E. Agerbo, M. Al Eissa, D. Albani, N. Alliey-Rodriguez, A. Anjorin, V. Antilla, A. Antoniou, S. Awasthi, J. H. Baek, M. Bækvad-Hansen, N. Bass, M. Bauer, E. C. Beins, S. E. Bergen, A. Birner, C. Bøcker Pedersen, E. Bøen, M. P. Boks, R. Bosch, M. Brum, B. M. Brumpton, N. Brunkhorst-Kanaan, M. Budde, J. Bybjerg-Grauholm, W. Byerley, M. Cairns, M. Casas, P. Cervantes, T.-K. Clarke, C. Cruceanu, A. Cuellar-Barboza, J. Cunningham, D. Curtis, P. M. Czerski, A. M. Dale, N. Dalkner, F. S. David, F. Degenhardt, S. Djurovic, A. L. Dobbyn, A. Douzenis, T. Elvsåshagen, V. Escott-Price, I. N. Ferrier, A. Fiorentino, T. M. Foroud, L. Forty, J. Frank, O. Frei, N. B. Freimer, L. Frisén, K. Gade, J. Garnham, J. Gelernter, M. Giørtz Pedersen, I. R. Gizer, S. D. Gordon, K. Gordon-Smith, T. A. Greenwood, J. Grove, J. Guzman-Parra, K. Ha, M. Haraldsson, M. Hautzinger, U. Heilbronner, D. Hellgren, S. Herms, P. Hoffmann, P. A. Holmans, L. Huckins, S. Jamain, J. S. Johnson, J. L. Kalman, Y. Kamatani, J. L. Kennedy, S. Kittel-Schneider, J. A. Knowles, M. Kogevinas, M. Koromina, T. M. Kranz, H. R. Kranzler, M. Kubo, R. Kupka, S. A. Kushner, C. Lavebratt, J. Lawrence, M. Leber, H.-J. Lee, P. H. Lee, S. E. Levy, C. Lewis, C. Liao, S. Lucae, M. Lundberg, D. J. MacIntyre, S. H. Magnusson, W. Maier, A. Maihofer, D. Malaspina, E. Maratou, L. Martinsson, M. Mattheisen, S. A. McCarroll, N. W. McGregor, P. McGuffin, J. D. McKay, H. Medeiros, S. E. Medland, V. Millischer, G. W. Montgomery, J. L. Moran, D. W. Morris, T. W. Mühleisen, N. O'Brien, C. O'Donovan, L. M. Olde Loohuis, L. Oruc, S. Papiol, A. F. Pardiñas, A. Perry, A. Pfennig, E. Porichi, J. B. Potash, D. Quested, T. Raj, M. H. Rapaport, J. R. DePaulo, E. J. Regeer, J. P. Rice, F. Rivas, M. Rivera, J. Roth, P. Roussos, D. M. Ruderfer, C. Sánchez-Mora, E. C. Schulte, F. Senner, S. Sharp, P. D. Shilling, E. Sigurdsson, L. Sirignano, C. Slaney, O. B. Smeland, D. J. Smith, J. L. Sobell, C. Søholm Hansen, M. Soler Artigas, A. T. Spijker, D. J. Stein, J. S. Strauss, B. Świątkowska, C. Terao, T. E. Thorgeirsson, C. Toma, P. Tooney, E.-E. Tsermpini, M. P. Vawter, H.

Vedder, J. T. R. Walters, S. H. Witt, S. Xi, W. Xu, J. M. K. Yang, A. H. Young, H. Young, P. P. Zandi, H. Zhou, L. Zillich, HUNT All-In Psychiatry, R. Adolfsson, I. Agartz, M. Alda, L. Alfredsson, G. Babadjanova, L. Backlund, B. T. Baune, F. Bellivier, S. Bengesser, W. H. Berrettini, D. H. R. Blackwood, M. Boehnke, A. D. Børglum, G. Breen, V. J. Carr, S. Catts, A. Corvin, N. Craddock, U. Dannlowski, D. Dikeos, T. Esko, B. Etain, P. Ferentinos, M. Frye, J. M. Fullerton, M. Gawlik, E. S. Gershon, F. S. Goes, M. J. Green, M. Grigoroiu-Serbanescu, J. Hauser, F. Henskens, J. Hillert, K. S. Hong, D. M. Hougaard, C. M. Hultman, K. Hveem, N. Iwata, A. V. Jablensky, I. Jones, L. A. Jones, R. S. Kahn, J. R. Kelsoe, G. Kirov, M. Landén, M. Leboyer, C. M. Lewis, Q. S. Li, J. Lissowska, C. Lochner, C. Loughland, N. G. Martin, C. A. Mathews, F. Mayoral, S. L. McElroy, A. M. McIntosh, F. J. McMahon, I. Melle, P. Michie, L. Milani, P. B. Mitchell, G. Morken, O. Mors, P. B. Mortensen, B. Mowry, B. Müller-Myhsok, R. M. Myers, B. M. Neale, C. M. Nievergelt, M. Nordentoft, M. M. Nöthen, M. C. O'Donovan, K. J. Oedegaard, T. Olsson, M. J. Owen, S. A. Paciga, C. Pantelis, C. Pato, M. T. Pato, G. P. Patrinos, R. H. Perlis, D. Posthuma, J. A. Ramos-Quiroga, A. Reif, E. Z. Reininghaus, M. Ribasés, M. Rietschel, S. Ripke, G. A. Rouleau, T. Saito, U. Schall, M. Schalling, P. R. Schofield, T. G. Schulze, L. J. Scott, R. J. Scott, A. Serretti, C. Shannon Weickert, J. W. Smoller, H. Stefansson, K. Stefansson, E. Stordal, F. Streit, P. F. Sullivan, G. Turecki, A. E. Vaaler, E. Vieta, J. B. Vincent, I. D. Waldman, T. W. Weickert, T. Werge, N. R. Wray, J.-A. Zwart, J. M. Biernacka, J. I. Nurnberger, S. Cichon, H. J. Edenberg, E. A. Stahl, A. McQuillin, A. Di Florio, R. A. Ophoff, O. A. Andreassen, Genome-wide association study of more than 40,000 bipolar disorder cases provides new insights into the underlying biology. *Nat. Genet.* **53**, 817–829 (2021).

106. V. Trubetskoy, A. F. Pardiñas, T. Qi, G. Panagiotaropoulou, S. Awasthi, T. B. Bigdeli, J. Bryois, C.-Y. Chen, C. A. Dennison, L. S. Hall, M. Lam, K. Watanabe, O. Frei, T. Ge, J. C. Harwood, F. Koopmans, S. Magnusson, A. L. Richards, J. Sidorenko, Y. Wu, J. Zeng, J. Grove, M. Kim, Z. Li, G. Voloudakis, W. Zhang, M. Adams, I. Agartz, E. G. Atkinson, E. Agerbo, M. Al Eissa, M. Albus, M. Alexander, B. Z. Alizadeh, K. Alptekin, T. D. Als, F. Amin, V. Arolt, M. Arrojo, L. Athanasiu, M. H. Azevedo, S. A. Bacanu, N. J. Bass, M. Begemann, R. A. Belliveau, J. Bene, B. Benyamin, S. E. Bergen, G. Blasi, J. Bobes, S. Bonassi, A. Braun, R. A. Bressan, E. J. Bromet, R. Bruggeman, P. F. Buckley, R. L. Buckner, J. Bybjerg-Grauholm, W. Cahn, M. J. Cairns, M. E. Calkins, V. J. Carr, D. Castle, S. V. Catts, K. D. Chambert, R. C. K. Chan, B. Chaumette, W. Cheng, E. F. C. Cheung, S. A. Chong, D. Cohen, A. Consoli, Q. Cordeiro, J. Costas, C. Curtis, M. Davidson, K. L. Davis, L. de Haan, F. Degenhardt, L. E. DeLisi, D. Demontis, F. Dickerson, D. Dikeos, T. Dinan, S. Djurovic, J. Duan, G. Ducci, F. Dudbridge, J. G. Eriksson, L. Fañanás, S. V. Faraone, A. Fiorentino, A. Forstner, J. Frank, N. B. Freimer, M. Fromer, A. Frustaci, A. Gadelha, G. Genovese, E. S. Gershon, M. Giannitelli, I. Giegling, P. Giusti-Rodríguez, S. Godard, J. I. Goldstein, J. González Peñas, A. González-Pinto, S. Gopal, J. Gratten, M. F. Green, T. A. Greenwood, O. Guillin, S. Gülöksüz, R. E. Gur, R. C. Gur, B. Gutiérrez, E. Hahn, H. Hakonarson, V. Haroutunian, A. M. Hartmann, C. Harvey, C. Hayward, F. A. Henskens, S. Herms, P. Hoffmann, D. P. Howrigan, M. Ikeda, C. Iyegbe, I. Joa, A. Julià, A. K. Kähler, T. Kam-Thong, Y. Kamatani, S. Karachanak-Yankova, O. Kebir, M. C. Keller, B. J. Kelly, A. Khrunin, S.-W. Kim, J. Klovins, N. Kondratiev, B. Konte, J. Kraft, M. Kubo, V. Kučinskas, Z. A. Kučinskiene, A. Kusumawardhani, H. Kuzelova-Ptackova, S. Landi, L. C. Lazzeroni, P. H. Lee, S. E. Legge, D. S. Lehrer, R. Lencer, B. Lerer, M. Li, J. Lieberman, G. A. Light, S. Limborska, C.-M. Liu, J. Lönnqvist, C. M. Loughland, J. Lubinski, J. J. Luykx, A. Lynham, M. Macek Jr, A. Mackinnon, P. K. E. Magnusson, B. S. Maher, W. Maier, D. Malaspina, J. Mallet, S. R. Marder, S. Marsal, A. R. Martin, L. Martorell, M. Mattheisen, R. W. McCarley,

C. McDonald, J. J. McGrath, H. Medeiros, S. Meier, B. Melegh, I. Melle, R. I. Mesholam-Gately, A. Metspalu, P. T. Michie, L. Milani, V. Milanova, M. Mitjans, E. Molden, E. Molina, M. D. Molto, V. Mondelli, C. Moreno, C. P. Morley, G. Muntané, K. C. Murphy, I. Myin-Germeys, I. Nenadić, G. Nestadt, L. Nikitina-Zake, C. Noto, K. H. Nuechterlein, N. L. O'Brien, F. A. O'Neill, S.-Y. Oh, A. Olincy, V. K. Ota, C. Pantelis, G. N. Papadimitriou, M. Parellada, T. Paunio, R. Pellegrino, S. Periyasamy, D. O. Perkins, B. Pfuhlmann, O. Pietiläinen, J. Pimm, D. Porteous, J. Powell, D. Quattrone, D. Quested, A. D. Radant, A. Rampino, M. H. Rapaport, A. Rautanen, A. Reichenberg, C. Roe, J. L. Roffman, J. Roth, M. Rothermundt, B. P. F. Rutten, S. Saker-Delye, V. Salomaa, J. Sanjuan, M. L. Santoro, A. Savitz, U. Schall, R. J. Scott, L. J. Seidman, S. I. Sharp, J. Shi, L. J. Siever, E. Sigurdsson, K. Sim, N. Skarabis, P. Slominsky, H.-C. So, J. L. Sobell, E. Söderman, H. J. Stain, N. E. Steen, A. A. Steixner-Kumar, E. Stögmann, W. S. Stone, R. E. Straub, F. Streit, E. Strengman, T. S. Stroup, M. Subramaniam, C. A. Sugar, J. Suvisaari, D. M. Svrakic, N. R. Swerdlow, J. P. Szatkiewicz, T. M. T. Ta, A. Takahashi, C. Terao, F. Thibaut, D. Toncheva, P. A. Tooney, S. Torretta, S. Tosato, G. B. Tura, B. I. Turetsky, A. Üçok, A. Vaaler, T. van Amelsvoort, R. van Winkel, J. Veijola, J. Waddington, H. Walter, A. Waterreus, B. T. Webb, M. Weiser, N. M. Williams, S. H. Witt, B. K. Wormley, J. Q. Wu, Z. Xu, R. Yolken, C. C. Zai, W. Zhou, F. Zhu, F. Zimprich, E. C. Atbaşoğlu, M. Ayub, C. Benner, A. Bertolino, D. W. Black, N. J. Bray, G. Breen, N. G. Buccola, W. F. Byerley, W. J. Chen, C. R. Cloninger, B. Crespo-Facorro, G. Donohoe, R. Freedman, C. Galletly, M. J. Gandal, M. Gennarelli, D. M. Hougaard, H.-G. Hwu, A. V. Jablensky, S. A. McCarroll, J. L. Moran, O. Mors, P. B. Mortensen, B. Müller-Myhsok, A. L. Neil, M. Nordentoft, M. T. Pato, T. L. Petryshen, M. Pirinen, A. E. Pulver, T. G. Schulze, J. M. Silverman, J. W. Smoller, E. A. Stahl, D. W. Tsuang, E. Vilella, S.-H. Wang, S. Xu, Indonesia Schizophrenia Consortium, PsychENCODE, Psychosis Endophenotypes International Consortium, SynGO Consortium, R. Adolfsson, C. Arango, B. T. Baune, S. I. Belangero, A. D. Børglum, D. Braff, E. Bramon, J. D. Buxbaum, D. Campion, J. A. Cervilla, S. Cichon, D. A. Collier, A. Corvin, D. Curtis, M. D. Forti, E. Domenici, H. Ehrenreich, V. Escott-Price, T. Esko, A. H. Fanous, A. Gareeva, M. Gawlik, P. V. Gejman, M. Gill, S. J. Glatt, V. Golimbet, K. S. Hong, C. M. Hultman, S. E. Hyman, N. Iwata, E. G. Jönsson, R. S. Kahn, J. L. Kennedy, E. Khusnutdinova, G. Kirov, J. A. Knowles, M.-O. Krebs, C. Laurent-Levinson, J. Lee, T. Lencz, D. F. Levinson, Q. S. Li, J. Liu, A. K. Malhotra, D. Malhotra, A. McIntosh, A. McQuillin, P. R. Menezes, V. A. Morgan, D. W. Morris, B. J. Mowry, R. M. Murray, V. Nimgaonkar, M. M. Nöthen, R. A. Ophoff, S. A. Paciga, A. Palotie, C. N. Pato, S. Qin, M. Rietschel, B. P. Riley, M. Rivera, D. Rujescu, M. C. Saka, A. R. Sanders, S. G. Schwab, A. Serretti, P. C. Sham, Y. Shi, D. St Clair, H. Stefánsson, K. Stefansson, M. T. Tsuang, J. van Os, M. P. Vawter, D. R. Weinberger, T. Werge, D. B. Wildenauer, X. Yu, W. Yue, P. A. Holmans, A. J. Pocklington, P. Roussos, E. Vassos, M. Verhage, P. M. Visscher, J. Yang, D. Posthuma, O. A. Andreassen, K. S. Kendler, M. J. Owen, N. R. Wray, M. J. Daly, H. Huang, B. M. Neale, P. F. Sullivan, S. Ripke, J. T. R. Walters, M. C. O'Donovan, Schizophrenia Working Group of the Psychiatric Genomics Consortium, Mapping genomic loci implicates genes and synaptic biology in schizophrenia. *Nature* **604**, 502–508 (2022).

107. W. van Rheenen, R. A. A. van der Spek, M. K. Bakker, J. J. F. A. van Vugt, P. J. Hop, R. A. J. Zwamborn, N. de Klein, H.-J. Westra, O. B. Bakker, P. Deelen, G. Shireby, E. Hannon, M. Moisse, D. Baird, R. Restuadi, E. Dolzhenko, A. M. Dekker, K. Gawor, H.-J. Westeneng, G. H. P. Tazelaar, K. R. van Eijk, M. Kooyman, R. P. Byrne, M. Doherty, M. Heverin, A. Al Khleifat, A. Iacoangeli, A. Shatunov, N. Ticozzi, J. Cooper-Knock, B. N. Smith, M. Gromicho, S. Chandran, S. Pal, K. E. Morrison, P. J. Shaw, J. Hardy, R. W.

Orrell, M. Sendtner, T. Meyer, N. Başak, A. J. van der Kooi, A. Ratti, I. Fogh, C. Gellera, G. Lauria, S. Corti, C. Cereda, D. Sproviero, S. D'Alfonso, G. Sorarù, G. Siciliano, M. Filosto, A. Padovani, A. Chiò, A. Calvo, C. Moglia, M. Brunetti, A. Canosa, M. Grassano, E. Beghi, E. Pupillo, G. Logroscino, B. Nefussy, A. Osmanovic, A. Nordin, Y. Lerner, M. Zabari, M. Gotkine, R. H. Baloh, S. Bell, P. Vourc'h, P. Corcia, P. Couratier, S. Millecamps, V. Meininger, F. Salachas, J. S. Mora Pardina, A. Assialioui, R. Rojas-García, P. A. Dion, J. P. Ross, A. C. Ludolph, J. H. Weishaupt, D. Brenner, A. Freischmidt, G. Bensimon, A. Brice, A. Durr, C. A. M. Payan, S. Saker-Delye, N. W. Wood, S. Topp, R. Rademakers, L. Tittmann, W. Lieb, A. Franke, S. Ripke, A. Braun, J. Kraft, D. C. Whiteman, C. M. Olsen, A. G. Uitterlinden, A. Hofman, M. Rietschel, S. Cichon, M. M. Nöthen, P. Amouyel, SLALOM Consortium, PARALS Consortium, SLAGEN Consortium, SLAP Consortium, B. J. Traynor, A. B. Singleton, M. Mitne Neto, R. J. Cauchi, R. A. Ophoff, M. Wiedau-Pazos, C. Lomen-Hoerth, V. M. van Deerlin, J. Grosskreutz, A. Roediger, N. Gaur, A. Jörk, T. Barthel, E. Theele, B. Ilse, B. Stubendorff, O. W. Witte, R. Steinbach, C. A. Hübner, C. Graff, L. Brylev, V. Fominykh, V. Demeshonok, A. Ataulina, B. Rogelj, B. Koritnik, J. Zidar, M. Ravnik-Glavač, D. Glavač, Z. Stević, V. Drory, M. Povedano, I. P. Blair, M. C. Kiernan, B. Benyamin, R. D. Henderson, S. Furlong, S. Mathers, P. A. McCombe, M. Needham, S. T. Ngo, G. A. Nicholson, R. Pamphlett, D. B. Rowe, F. J. Steyn, K. L. Williams, K. A. Mather, P. S. Sachdev, A. K. Henders, L. Wallace, M. de Carvalho, S. Pinto, S. Petri, M. Weber, G. A. Rouleau, V. Silani, C. J. Curtis, G. Breen, J. D. Glass, R. H. Brown Jr, J. E. Landers, C. E. Shaw, P. M. Andersen, E. J. N. Groen, M. A. van Es, R. J. Pasterkamp, D. Fan, F. C. Garton, A. F. McRae, G. Davey Smith, T. R. Gaunt, M. A. Eberle, J. Mill, R. L. McLaughlin, O. Hardiman, K. P. Kenna, N. R. Wray, E. Tsai, H. Runz, L. Franke, A. Al-Chalabi, P. Van Damme, L. H. van den Berg, J. H. Veldink, Common and rare variant association analyses in amyotrophic lateral sclerosis identify 15 risk loci with distinct genetic architectures and neuron-specific biology. *Nat. Genet.* **53**, 1636–1648 (2021).

108. D. Taliun, D. N. Harris, M. D. Kessler, J. Carlson, Z. A. Szpiech, R. Torres, S. A. G. Taliun, A. Corvelo, S. M. Gogarten, H. M. Kang, A. N. Pitsillides, J. LeFaive, S.-B. Lee, X. Tian, B. L. Browning, S. Das, A.-K. Emde, W. E. Clarke, D. P. Loesch, A. C. Shetty, T. W. Blackwell, A. V. Smith, Q. Wong, X. Liu, M. P. Conomos, D. M. Bobo, F. Aguet, C. Albert, A. Alonso, K. G. Ardlie, D. E. Arking, S. Aslibekyan, P. L. Auer, J. Barnard, R. G. Barr, L. Barwick, L. C. Becker, R. L. Beer, E. J. Benjamin, L. F. Bielak, J. Blangero, M. Boehnke, D. W. Bowden, J. A. Brody, E. G. Burchard, B. E. Cade, J. F. Casella, B. Chalazan, D. I. Chasman, Y.-D. I. Chen, M. H. Cho, S. H. Choi, M. K. Chung, C. B. Clish, A. Correa, J. E. Curran, B. Custer, D. Darbar, M. Daya, M. de Andrade, D. L. DeMeo, S. K. Dutcher, P. T. Ellinor, L. S. Emery, C. Eng, D. Fatkin, T. Fingerlin, L. Forer, M. Fornage, N. Franceschini, C. Fuchsberger, S. M. Fullerton, S. Germer, M. T. Gladwin, D. J. Gottlieb, X. Guo, M. E. Hall, J. He, N. L. Heard-Costa, S. R. Heckbert, M. R. Irvin, J. M. Johnsen, A. D. Johnson, R. Kaplan, S. L. R. Kardia, T. Kelly, S. Kelly, E. E. Kenny, D. P. Kiel, R. Klemmer, B. A. Konkle, C. Kooperberg, A. Köttgen, L. A. Lange, J. Lasky-Su, D. Levy, X. Lin, K.-H. Lin, C. Liu, R. J. F. Loos, L. Garman, R. Gerszten, S. A. Lubitz, K. L. Lunetta, A. C. Y. Mak, A. Manichaikul, A. K. Manning, R. A. Mathias, D. D. McManus, S. T. McGarvey, J. B. Meigs, D. A. Meyers, J. L. Mikulla, M. A. Minear, B. D. Mitchell, S. Mohanty, M. E. Montasser, C. Montgomery, A. C. Morrison, J. M. Murabito, A. Natale, P. Natarajan, S. C. Nelson, K. E. North, J. R. O'Connell, N. D. Palmer, N. Pankratz, G. M. Peloso, P. A. Peyser, J. Pleiness, W. S. Post, B. M. Psaty, D. C. Rao, S. Redline, A. P. Reiner, D. Roden, J. I. Rotter, I. Ruczinski, C. Sarnowski, S. Schoenherr, D. A. Schwartz, J.-S. Seo, S. Seshadri, V. A. Sheehan, W. H. Sheu, M. B. Shoemaker, N. L. Smith, J. A. Smith, N. Sotoodehnia, A. M.

Stilp, W. Tang, K. D. Taylor, M. Telen, T. A. Thornton, R. P. Tracy, D. J. Van Den Berg, R. S. Vasan, K. A. Viaud-Martinez, S. Vrieze, D. E. Weeks, B. S. Weir, S. T. Weiss, L.-C. Weng, C. J. Willer, Y. Zhang, X. Zhao, D. K. Arnett, A. E. Ashley-Koch, K. C. Barnes, E. Boerwinkle, S. Gabriel, R. Gibbs, K. M. Rice, S. S. Rich, E. K. Silverman, P. Qasba, W. Gan, NHLBI Trans-Omics for Precision Medicine (TOPMed) Consortium, G. J. Papanicolaou, D. A. Nickerson, S. R. Browning, M. C. Zody, S. Zöllner, J. G. Wilson, L. A. Cupples, C. C. Laurie, C. E. Jaquish, R. D. Hernandez, T. D. O'Connor, G. R. Abecasis, Sequencing of 53,831 diverse genomes from the NHLBI TOPMed Program. *Nature* **590**, 290–299 (2021).

109. A. Manichaikul, J. C. Mychaleckyj, S. S. Rich, K. Daly, M. Sale, W.-M. Chen, Robust relationship inference in genome-wide association studies. *Bioinformatics* **26**, 2867–2873 (2010).

110. 1000 Genomes Project Consortium, G. R. Abecasis, A. Auton, L. D. Brooks, M. A. DePristo, R. M. Durbin, R. E. Handsaker, H. M. Kang, G. T. Marth, G. A. McVean, An integrated map of genetic variation from 1,092 human genomes. *Nature* **491**, 56–65 (2012).

111. 1000 Genomes Project Consortium, A. Auton, L. D. Brooks, R. M. Durbin, E. P. Garrison, H. M. Kang, J. O. Korbel, J. L. Marchini, S. McCarthy, G. A. McVean, G. R. Abecasis, A global reference for human genetic variation. *Nature* **526**, 68–74 (2015).

112. P. Danecek, J. K. Bonfield, J. Liddle, J. Marshall, V. Ohan, M. O. Pollard, A. Whitwham, T. Keane, S. A. McCarthy, R. M. Davies, H. Li, Twelve years of SAMtools and BCFtools. *Gigascience* **10** (2021).

113. C. C. Chang, C. C. Chow, L. C. Tellier, S. Vattikuti, S. M. Purcell, J. J. Lee, Second-generation PLINK: rising to the challenge of larger and richer datasets. *Gigascience* **4**, 7 (2015).

114. T. Ge, C.-Y. Chen, Y. Ni, Y.-C. A. Feng, J. W. Smoller, Polygenic prediction via Bayesian regression and continuous shrinkage priors. *Nat. Commun.* **10**, 1776 (2019).

115. C. J. Bohlen, F. C. Bennett, A. F. Tucker, H. Y. Collins, S. B. Mulinyawe, B. A. Barres, Diverse Requirements for Microglial Survival, Specification, and Function Revealed by Defined-Medium Cultures. *Neuron* **94**, 759–773.e8 (2017).

116. D. Gosselin, D. Skola, N. G. Coufal, I. R. Holtman, J. C. M. Schlachetzki, E. Sajti, B. N. Jaeger, C. O'Connor, C. Fitzpatrick, M. P. Pasillas, M. Pena, A. Adair, D. D. Gonda, M. L. Levy, R. M. Ransohoff, F. H. Gage, C. K. Glass, An environment-dependent transcriptional network specifies human microglia identity. *Science* **356** (2017).

117. S. R. Ocañas, K. D. Pham, H. E. Blankenship, A. H. Machalinski, A. J. Chucair-Elliott, W. M. Freeman, Minimizing the Ex Vivo Confounds of Cell-Isolation Techniques on Transcriptomic and Translatomic Profiles of Purified Microglia. *eNeuro* **9** (2022).

118. S. C. van den Brink, F. Sage, Á. Vértesy, B. Spanjaard, J. Peterson-Maduro, C. S. Baron, C. Robin, A. van Oudenaarden, Single-cell sequencing reveals dissociation-induced gene expression in tissue subpopulations. *Nat. Methods* **14**, 935–936 (2017).

2257 119. Y. Lee, J. S. Lee, K. J. Lee, R. S. Turner, H.-S. Hoe, D. T. S. Pak, Polo-like kinase 2
2258 phosphorylation of amyloid precursor protein regulates activity-dependent amyloidogenic
2259 processing. *Neuropharmacology* **117**, 387–400 (2017).

2260 120. J. S. Lee, Y. Lee, E. A. André, K. J. Lee, T. Nguyen, Y. Feng, N. Jia, B. T. Harris, M. P.
2261 Burns, D. T. S. Pak, Inhibition of Polo-like kinase 2 ameliorates pathogenesis in
2262 Alzheimer's disease model mice. *PLoS One* **14**, e0219691 (2019).

2263 121. M. Setty, V. Kiseliovas, J. Levine, A. Gayoso, L. Mazutis, D. Pe'er, Characterization of
2264 cell fate probabilities in single-cell data with Palantir. *Nat. Biotechnol.* **37**, 451–460 (2019).

2265 122. K. Street, D. Risso, R. B. Fletcher, D. Das, J. Ngai, N. Yosef, E. Purdom, S. Dudoit,
2266 Slingshot: cell lineage and pseudotime inference for single-cell transcriptomics. *BMC*
2267 *Genomics* **19**, 477 (2018).

2268 123. G. Schiebinger, J. Shu, M. Tabaka, B. Cleary, V. Subramanian, A. Solomon, J. Gould, S.
2269 Liu, S. Lin, P. Berube, L. Lee, J. Chen, J. Brumbaugh, P. Rigollet, K. Hochedlinger, R.
2270 Jaenisch, A. Regev, E. S. Lander, Optimal-Transport Analysis of Single-Cell Gene
2271 Expression Identifies Developmental Trajectories in Reprogramming. *Cell* **176**, 928–
2272 943.e22 (2019).

2273